UNIVERSIDAD DE LA RIOJA

TESIS DOCTORAL

Título
A capture model for irregular moons based on a restricted 2+2 body problem and its statistical analysis

Autor/es
Wafaa Kanaan

Director/es
Víctor Lanchares Barrasa

Facultad
Facultad de Ciencia y Tecnología

Titulación

Departamento
Matemáticas y Computación

Curso Académico

FACULTY OF SCIENCE AND TECHNOLOGY

DEPARTMENT OF MATHEMATICS AND COMPUTATION

PHD THESIS:

A CAPTURE MODEL FOR IRREGULAR MOONS BASED ON A RESTRICTED 2+2 BODY PROBLEM AND ITS STATISTICAL ANALYSIS

A Thesis submitted by Wafaa Kanaan for the degree of Doctor of Philosophy in the University of La Rioja

Supervised by:
Víctor Lanchares

To the soul of my brother Aeman. . .

*Who has always been my hero and
now is the brightest star in my sky,
showing me the right path to follow.*

Acknowledgements

I would like to express my gratitude to everybody that, in one way or another, has contributed with valuable help and comments that finally ended in this report.

First of all, I would like to thank my advisor, Victor Lanchares, for guiding and supporting me. From him I learned many things and with him I shared very hard times during these years of thesis. He has set an example of excellence as a researcher, teacher, person and role model.

I would also like to thank Dr. David Farrelly for all his help. His ideas and discussion have been absolutely invaluable.

I would like to thank Dr. Juan Félix San Juan Díaz for his kindly treatment and for the support I received from him.

I would especially like to thank my amazing family for all the love, support and constant encouragement I have got over the years. In particular, I would like to thank my parents, my brothers, my sister Faten and my aunt Kholoud. They are the joy of my life and without them I would have never got what I am.

I cannot forget my friend Marcial Roa Ros, who encouraged me in the dark moments and get me up when I lost the trust in myself, during these years of study in Spain. He has been like a brother to me.

Also, I would like to mention the support of my friends Rasha Ibrahim, Yolla Mahmoud, Heba Kbeli, Mary Mahmoud, Sandra Pérez, Marta García Cueva, Laura Pirouano, Gennaro Principe and David Gondelach. They gave to me wonderful friendship, affection and love.

I would like to thank all the people I have met in Spain for all the love I received from them. They made me feel like if I was in my country with my people.

Finally, I would like to thank my country Syria, which gave me the opportunity to travel to pursue my studies and still offers support to me and to all Syrian Students in spite of the long years of war.

vi

Table of contents

List of symbols

Symbol	Meaning
m_j	mass of the body j
M_1, M_2	masses of the primaries in the restricted $2+2$ body problem
μ	mass ratio
T	period of the circular motion
U	effective potential function
C	Jacobi constant
H	Hamiltonian function
$L_1, L_2, \ldots, L_5$	Lagrange points
x, y, z	Cartesian coordinates
p_x, p_y, p_z	conjugate momenta
r_H	Hill's radius
a	semi major axis
e	eccentricity
i	inclination
w	argument of the periapsis
H	absolute magnitude of a Kuiper belt object
n	number of observed oppositions for Kuiper belt objects

Introduction

The history of astronomy is the history of a growing awareness of our position in the universe. Observing, exploring, and ultimately understanding our solar system is the first step towards understanding the rest of the universe. The key discovery in this process was Newton's formulation of the universal law of gravitation; this made sense of the orbits of planets, satellites, and comets, and their future motion could be predicted [MD99].

If Newton's laws were a fundamental milestone in our understanding of the universe, technological advances in the construction of new optical devices to explore outer space have produced a never ending succession of discoveries that have enlarged our view of the solar system. Every new object discovered is a piece of an astonishing puzzle that scientists try to reconstruct, and Newton's laws help this process. One of the first questions scientists tried to solve was the stability of the solar system; will the trajectories followed by the planets remain stable over time or will the planets escape or fall into the Sun? Many of the best astronomers and mathematicians have tackled this question and have produced a plethora of results in many directions, helping to solve another more interesting question: the formation and evolution of the solar system or what was the history of solar system objects before they came to occupy their present positions. This general problem yields to partial questions concerning the main bodies of the solar system, namely the planets, and the minor bodies, such as satellites, asteroids, comets, and Kuiper belt objects. Our goal is to study a particular piece of this problem: the capture of minor bodies by a planet, giving some clues about how an object can end up in a different place than other similar objects, belonging to the same family.

The solar system contains eight planets that astronomers have divided into two groups: the inner and the outer planets. The inner planets are Mercury, Venus, Earth and Mars and they are the closest to the sun. The outer solar system contains the planets Jupiter, Saturn, Uranus and Neptune. The inner and outer planets are separated by a belt containing hundred of thousands of small irregular bodies, the largest one being Ceres having a diameter of approximately 950 Km. This belt is referred to as the main asteroid belt and the total mass of the asteroid belt has been calculated to be about 4% the mass of the Moon; in fact the four largest asteroids

constitute more than half of the total mass. As did the rest of the components of the solar system, the asteroid belt formed from the small precursors of the planets, known as planetesimals, which were the main components of the primordial solar nebula. Gravitational perturbations of Jupiter prevented the formation of a planet in between Mars and Jupiter by scattering the planetesimals from this area of the solar system.

The inner and outer planets are not only separated by the main belt, they exhibit very different features. Indeed, the inner planets are referred to as the rocky or terrestrial planets. All of them are similar to the Earth in composition and size; they have a solid surface and are composed of heavy metals, such as nickel and iron. In addition, they have few or no moons. Only the Earth and Mars have moons; Earth has one and Mars two. Moreover, the inner planets spin relatively slowly when compared to the outer planets which are much larger in size. The Earth is the quickest of the inner planets taking 23 hours, 56 minutes and 4 seconds to rotate around its axis.

The outer planets are also called the Jovian planets or gas giants, as they are similar to Jupiter. They are mainly made of gas and are thought not to have a solid surface, while the core is thought to be liquid. They are large in size and they make up 99% of the mass of all the bodies orbiting the sun. Despite their size, they spin around their axis much quicker than do the inner planets. Even Uranus, the slowest of the outer planets, takes only 17 hours and 14 minutes to complete a revolution about its axis. Opposed to the inner planets, the outer planets have a large number of moons. Indeed, Jupiter has 67 known moons, Saturn 62, Uranus 27 and Neptune 14. These differences between the terrestrial and Jovian planets can be summarized by collecting some data, as it is done in Table for the Earth and Jupiter, the two representative planets in the inner and outer solar system.

Basic data	Jupiter	Earth
Equatorial radius	71 492 km	6 378 km
Density	1.326 kg/m^3	5.514 kg/m^3
Spin period	9.84 hours	23.93 hours
Surface temperature	-120ºC	15ºC
Known moons	67	1

Table 1: Basic data for a comparison between Jupiter and the Earth.

Focusing on the moons of the planets, none of them – with the obvious exception of the Moon itself – was known up to the appearance of the telescope,

as none of them is visible to the naked eye. In 1610, using a very basic telescope with a 20× magnification power, Galileo observed for the first time moons around a planet other than the Earth. These moons, known as Galilean moons, are the four largest ones of Jupiter: Io, Europa, Ganymede and Callisto. After Galileo's discovery, almost three centuries passed until a new moon around Jupiter was spotted by Edward Emerson Barnard, on 9 September 1892, using the 36 inch refractor telescope at Lick Observatory. This was the last satellite discovered by direct visual observation. All the moons discovered since them were found photographically or, more recently, with the aid of space probes. In fact, before the launch of exploration missions to the outer solar system, only 11 moons were known to be orbiting around Jupiter. As of now this number has increased substantially to a total of 67. It is almost unnecessary to say that the recent discovered moons are very small in size compared to the Galilean moons. Indeed, the Galilean moons are similar in size to Mercury, the smallest of the terrestrial planets, with Ganymede being even larger that Mercury, while Callisto is roughly the same size. The rest of Jupiter's moons are less than 250 km across, with the largest one being Amalthea, precisely the one discovered in 1892 by Barnard.

A similar story can be told about the moons of the other giant planets, although with some differences. For instance, Saturn has only one large moon, Titan, which is larger than Mercury, but smaller than Ganymede. The rest are smaller, but eight of them are quite large with sizes ranging from 200 to 1500 Km across; the rest are about 10 km across in average. In the case of Uranus, the largest satellite is Titania, about 1500 Km across together with other four satellites with diameters above 500 km. The rest of the moons are small, but larger than the smallest ones of Jupiter and Saturn. The last of the giant planets, Neptune, has Triton as its largest moon which is about 80% the size of the Moon, while the rest of the satellites are smaller, but very similar in size to the lesser Uranian moons.

Size is not the only difference among the moons of giant planets, a close look at other relevant physical parameters, in this case the orbital elements, reveals a very different dynamical behavior. In Tables 2-4 some relevant data of the 67 known satellites of Jupiter are presented, where the satellites have been classified according to the direction of their orbital motion, setting aside recently discovered and as yet unnamed satellites.

If we pay attention to the size, the semimajor axis and inclination, we can have a picture of the spatial distribution of the Jovian moons which give us some clues about differences in their nature. This is depicted in Figure 1, where the Galilean moons are clearly distinguished from the rest because of their size. These moons, together with the inner lesser satellites, exhibit low inclinations with respect to the equatorial plane of Jupiter. On the contrary, the rest of the moons have high inclinations, at the same time they are of small size. Among these satellites there

Name	a (Jup. radius)	Period (days)	I (deg)	e	Radius (Km)	Discovery date
Small Inner Regular Satellites						
Metis	1.79	0.29	0.06	0.0002	20	1979
Adrastea	1.80	0.30	0.03	0.0015	8.2	1979
Amalthea	2.54	0.50	0.40	0.0030	83.5	1892
Thebe	3.11	0.68	0.80	0.0180	49.3	1979
Galilean Satellites						
Io	5.91	1.77	0.04	0.0040	1821.6	1610
Europa	9.40	3.55	0.47	0.0101	1560.8	1610
Ganymede	14.97	7.16	0.21	0.0015	2631.2	1610
Callisto	26.33	16.69	0.51	0.0070	2410.3	1610
Themisto Prograde Irregular Group						
Themisto	105.00	130.02	45.67	0.2420	4	1975/2000
Himalia Prograde Irregular Group						
Leda	156.20	240.92	27.47	0.1640	9	1974
Himalia	160.30	250.57	27.63	0.1620	85	1904
Lysithea	163.90	259.22	27.35	0.1120	18	1938
Elara	164.20	259.65	24.77	0.2170	40	1905
Dia	175.70	287.00	28.20	0.2480	2	2000
Carpo Prograde Irregular Group						
Carpo	237.60	456.10	51.40	0.4300	1.5	2003

Table 2: Physical and orbital data for Jupiter's prograde satellites.

Name	a (Jup. radius)	Period (days)	I (deg)	e	Radius (Km)	Discovery date
Retrograde Irregular Group						
Euporie	271.20	553.10	147.00	0.1560	1.0	2001
Orthosie	289.80	622.60	145.90	0.2810	1.0	2001
Euanthe	290.90	620.60	148.90	0.2320	1.5	2001
Thyone	292.90	627.30	148.50	0.2290	2.0	2001
Mneme	294.70	620.00	148.60	0.2270	1.0	2003
Harpalyke	295.30	623.30	148.70	0.2270	2.2	2000
Hermippe	295.60	633.90	150.70	0.2100	2.0	2001
Praxidike	295.80	625.30	148.70	0.2200	3.4	2000
Thelxinoe	296.00	628.10	151.40	0.2210	1.0	2003
Helike	297.40	634.80	154.80	0.1560	2.0	2003
Iocaste	297.50	631.50	159.70	0.2180	2.6	2000
Ananke	297.70	629.80	148.90	0.2440	14	1951
Eurydome	319.60	717.30	150.30	0.2760	1.5	2001
Arche	320.70	723.90	165.00	0.2590	1.5	2002
Autonoe	322.30	762.70	152.90	0.3340	2.0	2001
Herse	323.10	715.40	164.20	0.2000	1.0	2003
Pasithee	232.10	716.30	165.40	0.2880	1.0	2001
Chaldene	324.20	723.80	165.40	0.2380	1.9	2000
Kale	324.80	729.50	165.00	0.2600	1.0	2001
Isonoe	324.80	725.50	165.00	0.2610	1.9	2000
Aitne	324.90	730.20	165.10	0.2640	1.5	2001
Erinome	325.60	728.30	164.90	0.2700	1.6	2000
Taygete	326.70	732.20	165.20	0.2510	2.5	2000
Carme	327.30	734.20	164.90	0.2530	23	1938
Sponde	328.60	748.30	151.00	0.3120	1.0	2001
Kalyke	329.80	743.00	165.20	0.2430	2.6	2000
Pasiphae	330.40	743.60	151.40	0.4090	29	1908
Eukelade	330.90	746.40	165.50	0.2720	2.0	2003
Megaclite	333.00	752.80	152.80	0.4210	2.7	2000
Sinope	334.90	758.90	158.10	0.2500	19	1914
Hegemone	335.00	739.60	155.20	0.3280	1.5	2003
Aoede	335.40	761.50	158.30	0.4320	2.0	2003
Kallichore	336.30	764.70	165.50	0.2640	1.0	2003
Callirrhoe	337.10	758.80	147.10	0.2830	4.0	1999
Cyllene	340.60	737.80	149.30	0.3190	1.0	2003
Kore	343.30	779.20	152.40	0.3250	1.0	2003

Table 3: Physical and orbital data for Jupiter's retrograde satellites.

Name	a (Jup. radius)	Period (days)	I (deg)	e	Radius (Km)	Discovery date
Unnamed Satellites						
S/2003J2	399.60	982.50	151.80	0.3800	1.0	2003
S/2003J3	256.50	504.00	143.70	0.2410	1.0	2003
S/2003J4	325.40	723.20	144.90	0.2040	1.0	2003
S/2003J5	336.80	759.70	165.00	0.2100	2.0	2003
S/2003J9	313.90	683.00	164.50	0.2690	1.0	2003
S/2003J10	339.20	767.00	164.10	0.2140	1.0	2003
S/2003J12	265.80	533.30	145.80	0.3760	1.0	2003
S/2003J15	307.70	668.40	140.80	0.1100	1.0	2003
S/2003J16	293.70	595.40	148.60	0.2700	1.0	2003
S/2003J18	289.50	606.30	146.50	0.1190	1.0	2003
S/2003J19	318.90	701.30	162.90	0.3340	1.0	2003
S/2003J23	336.50	759.70	149.20	0.3090	1.0	2003
S/2010J1	326.10	723.20	163.20	0.3200	1.0	2010
S/2010J2	284.00	588.10	150.40	0.3070	1.0	2010
S/2011J1	281.90	580.70	162.80	0.2960	1.0	2011
S/2011J2	326.30	726.80	151.90	0.3870	1.0	2011

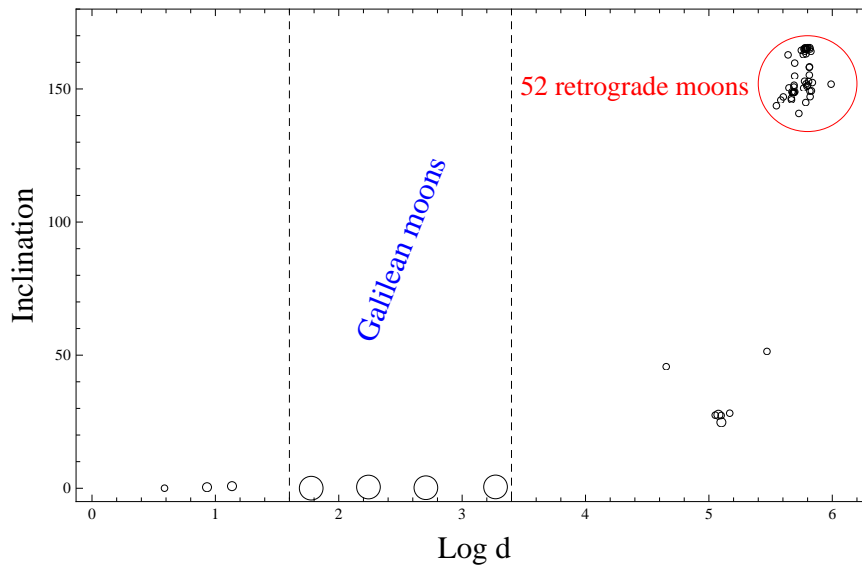Table 4: Physical and orbital data for Jupiter's unnamed satellites.

Figure 1: Spatial distribution of Jupiter moons, according to the semimajor axis and inclination. In the x axis the logarithm of the mean distance to the planet, measured in Jupiter's radii, and in the y axis the inclination of the orbital plane, measured in degrees.

are basically two groups, the group of prograde moons, with Temisto, the Himalia family and Carpo, and the retrograde moons which can also be divided into different subgroups represented by the largest moons Ananke, Carme and Pasiphae.

In this sense, the satellites of Jupiter can be roughly classified into two groups: the regular and the irregular moons. The group of regular moons are the set of closer satellites that ends at Callisto, the farthest Galilean moon. Beyond Callisto, we find the irregular moons, with small sizes, high inclinations and also high eccentricities. But, the most remarkable fact is that, among the irregular moons, most of them have inclinations above $90°$, that is to say they move in a retrograde sense around Jupiter.

All the previous considerations suggest a different origin for regular and irregular moons. The regular ones resemble a solar system in miniature and even the ratio of their masses, especially the Galilean moons, is very similar to the ratio of the planets with respect to the Sun. In this sense, the formation process of regular satellites is not very different from that of the solar system. That is, the regular satellites originated at roughly the same time as the planet from an accretion disk, present around the protoplanet at a late stage of its formation [ME03a]. In contrast, irregular moons are, almost surely, captured objects. This fact was suggested by Kuiper [Kui51a, Kui56], who pointed out that satellite accretion in a

circumplanetary disk is unable to produce the extreme orbits of the irregular satellites, in particular the retrograde motions. So, it is assumed they were formed in a different part of the solar system and were captured by Jupiter as a result of its gravitational influence in combination with other forces. In fact, a simple chain of reasoning yields to this conclusion and, even more, to argue that the irregular moons were mainly captured in the early stages of the formation of the solar system [JS04, JH07]. We can summarized all of these facts in the following key points:

1. The orbits of irregular satellites cannot be explained as a result of accretion in circumplanetary disks because they have very large sized orbits and high inclinations, difficult to match with an origin in a circumplanetary disk [CW02, CW06]. This is more evident in the case of retrograde satellites, which seems to be incompatible with a prograde cricumplanetary disk.

2. As a result of the first item, the more likely scenario is that irregular satellites formed in other place of the solar system and later been captured from heliocentric orbits into their current orbits around their host planets [JH07].

3. It is not difficult to achieve a temporary capture. However, a permanent capture from heliocentric orbit needs energy dissipation.

4. In the present state of the solar system energy dissipation can be a rare phenomenon and, therefore, the captures must have occurred, mainly, during an earlier epoch.

On this basis, different models have been proposed to explain the capture mechanism of irregular moons and all of them have to account for the observational facts:

- They are well separated from the circumplanetary disk that originated regular moons. Indeed they are located far from the centrifugal radius [ME03b]

- Their eccentricities are large in comparison to the regular satellites, which have orbits that are nearly circular.

- Many of them have retrograde orbital motion ($i > 90°$), while the orbits of regular satellites are exclusively prograde.

Among the models proposed in the literature we highlight the following ones:

1. Capture of irregular moons during the migration of the giant planets

   This model is based on the so-called *Nice model* (after the city of Nice in France where the model was developed). The Nice model holds that the

Jovian planets formed closer to the Sun and then migrated within the planetesimal disk to their current positions. The capture process of irregular satellites was due to three-body gravitational reactions during planetary encounters, when nearby planetesimals could be deflected into planet-bound orbits. In [NVM07], it is said that it is likely that the efficiency of this capture mechanism is sufficient to produce populations of observed irregular satellites for the Saturn, Uranus and Neptune systems. However, for the case of Jupiter, different mechanisms are necessary to explain its large population of irregular moons [NVD14].

2. Capture of a binary asteroid that is disrupted in the vicinity of Jupiter

In this model [PHA10, GWN11, GWN13], it is proposed that the planet captures a binary asteroid which is then disrupted through tidal interactions. The energy loss from disruption may be sufficient for capture of one member of the binary. However, this mechanism seems not to be enough to place the bodies in the actual observed orbits and an interaction with a tenuous circumplanetary gas disk is necessary. Nevertheless, in [GWN13], it is demonstrated that the capture mechanism of a binary asteroid can produce permanent captures of objects by itself, which have very similar orbits to irregular Jovian satellites. Some of the captured objects without aid of gas drag or other mechanisms yield semi-major axes, eccentricities and inclinations, which are similar to the known irregular Jovian moons.

This model cannot account for the totality of irregular moons, as it cannot account for all the observed groups of irregular satellites by the simulations [GWN13], and also because the population of binary asteroids is not so great as to give rise to a number of favorable situations [RW06]. Therefore, this model, as a feasible scenario for capture, must be complemented with other models that facilitate permanent captures.

3. Chaos assisted capture

In fact, this is a very general model that is in the basis of almost every other one (although the mechanism was elucidated only relatively recently [ABWF03, AF04]). In this model, the capture of irregular moons by giant planets occurs by a process in which, after they are temporarily trapped inside the planet's Hill sphere in very long living orbits, an unknown mechanism, for instance gas drag [ABWF03, PBT79, Kor05], produces a loss of energy in such a way the moon is permanently trapped in a bounded orbit.

The key point in this model is that incoming potential satellites get trapped in chaotic orbits close to *sticky* KAM tori in the neighborhood of the planet,

possibly for long times, so that the chaotic layer largely dictates the final orbital properties of the captured moons [AF04].

It is clear that different models are able to explain the capture of irregular moons by giant planets and it is also clear that all of them could happen in the past. In this way, it is very likely that more than one mechanism is responsible of the capture process. Thus, taking as a starting point the chaotic assisted capture, the aim of this work is to develop a good model that produces long living orbits inside the Hill sphere, that can be further conducted to permanently trapped orbits by gas drag, tidal forces or other mechanisms. In this sense, we will consider a restricted 2+2 body problem in the planar case, in which two small intruders interact inside the Hill sphere interchanging energy. To this end, we will follow the main ideas stated in [ABWF03], based on Monte Carlo simulations and Poincaré surfaces of section. Besides, we will also analyze the population of Kuiper belt objects, as they are potential parent bodies of our model. In this way, a statistical study is done in order to better understand the distribution of these objects and the main observational biases. These aspects are treated in different chapters of this report.

In chapter 1, we present the basics of the restricted there-body problem and its Hill approximation, we will use as a corner stone of our further study. We also introduce the concept of zero velocity curves and the Hill sphere. Besides, Levi-Civita regularized coordinates are presented as a very useful tool to avoid singularities that take place at collisions and also to prevent instabilities while numerical integration of the equations of the motion. Finally, Poincaré surfaces of section show the behavior of the orbits as a function of the Jacobi constant, giving a clear idea of those orbits well disposed to escape.

Chapter 2 is devoted to the description of the restricted 2+2 body problem, the model proposed as the cause of the existence of very long living orbits. This model can be viewed as the sum of two restricted three-body problems coupled by an interacting term of the two small bodies. Due to its structure, it admits also a Hill approximation and the problem turns to be, as expected, the sum of two Hill problems coupled by the interacting term of the two small bodies. If the two bodies are supposed to have equal masses, the resulting model only depends on the mass ratio of the small bodies and the planet. The chapter concludes with the introduction of Waldvogel regularized coordinates, suitable for numerical integration of the equations of the motion.

In chapter 3, we present the results of the numerical simulations. There, it is explained how the isotropic set of test particles was originated inside the Hill sphere to conduct the Monte Carlo simulation. This set is obtained on the basis of the Hill approximation of the restricted three body problem and then used to select a pair of objects that interact in our restricted 2+2 body model. Then, a statistical

analysis is done of the results obtained. Firstly, we pay attention to the capture rate for different mass ratios and afterwards we focus on a details analysis of one of the cases, for a mass ratio $\mu = 10^{-6}$, where we pay attention to the energy change, the interaction time and the type of captured orbits, among other things.

Chapter 4 is devoted to the statistical analysis of the Kuiper belt objects. We pay attention to the distribution of the main orbital elements, which give rise to the classification of these objects into different dynamical groups with particular characteristics. The information obtained from here gives clues about the formation and evolution of the solar system and could be relevant to identify the possible parent bodies of the proposed capture model. To conclude this chapter, we focus on the biases of the observed population and we give an interesting approach to the role played by the argument of the periapsis on the pointing bias.

This report ends with an appendix where the theoretical background of the Monte Carlo method is treated, as our main results are based on this technique.

Chapter 1

The three-body, restricted three-body and Hill problems

The publication in 1672 of the *Principia Mathematica*, by Isaac Newton, marked a milestone in the understanding and description of many physical phenomena in nature. Thanks to the universal gravitation law, the motion of two spherical bodies, mutually attracting each other, could be completely solved, recovering the known Kepler's laws about the planetary motion. The success in describing the two-body problem allowed consideration of the motion of the planets in the solar system, with special attention to the stability of their orbits. Since large bodies (e.g., planets, dwarf planets) in the solar system are approximately spherical and their dimensions extremely small when compared with the distances between them, they can be regarded as point masses. This simplification gives rise to the so called n-body problem, that aims to describe the motion of n-mass points under their mutual gravitational attraction. Despite the simple formulation it is clear that, to have a complete solution, we need to solve a system of $3n$ coupled differential equations of second order. All the attempts to do this analytically failed and only special solutions could be derived. Due to the difficulty in facing the n-body problem, astronomers, mathematicians and physicists focused on the *simplest case*, after the already solved two-body problem: the three-body problem. This is a classical problem that well serves to describe a wide range of astronomical situations, as it is the motion of an asteroid or a comet under the influence of Sun and Jupiter and also the mutual motion of the Moon and the Earth as perturbed by the Sun.

   Over the years the three-body problem caught the attention of the most outstanding physicists and mathematicians, such as Euler, Lagrange, Jacobi, Hadamard, Hill, Poincaré, Levi-Civita, Birkhoff, Szebehely and Deprit. Their contributions can be divided into two general categories: those which were concerned with finding general theorems about the motion (global dynamics), and those searching

for good approximations for solutions that would hold for a given period of time starting from an instant at which data was available (local dynamics).

Newton was the first to achieve results in both the global and local dynamics. On the one hand, he proved that the centre of mass of the bodies moves at uniform speed following a straight path. On the other hand, using essentially a geometric approach of the variation of parameters method, he applied perturbation theory to describe the motion of moon. However, the calculations caused him great difficulties, especially with the motion of the lunar apsides [BG97]. These difficulties ended in further simplifications in the statement of the problem and, as a consequence, in a simplification of the equations which govern the motion. To arrive to the first simplification, let us consider the trajectory of a comet under the gravitational influence of the Sun and Jupiter. We acknowledge that the mass of the comet is negligible compared with those of the Sun and Jupiter. In this way, no effect of the gravitational attraction of the comet on the motion of Jupiter and the Sun can be supposed. In addition, the orbit of Jupiter around the Sun is not very different from a circular one, so that we also can assume this is the case. These assumptions lead to the *circular restricted three-body problem*, describing the motion of a test particle moving under the gravitational forces of two principal bodies or primaries, which move in a circular mutual orbit. The mass of the test particle is negligible, in such a way that it does not exert any influence on the motion of the two primaries.

The second simplification was proposed by Hill [Hil78] when studying the motion of the Moon, by considering the effect of the Sun's gravity field. The main idea is that we are only interested in the motion of the test particle around the smallest primary but perturbed by the large body [PH86, HP86]. If the mass ratio of the primaries is a small quantity and the distance of the test particle to the smallest primary is also small compared to the distance of the primaries, a simplified version of the restricted three body problem is obtained.

1.1   The restricted three-body problem and equations of motion

Let us consider the restricted three body problem and denote by m_1, m_2 and m_3 the masses of three bodies, where m_1 and m_2 correspond to the masses of the primaries and m_3 to the mass of the last particle. Now we consider an inertial frame (ξ, η, ζ) with the origin at the center of mass of the primaries. The ξ axis lie along the line from m_1 to m_2 at time $t = 0$ with the η axis perpendicular to it and in the orbital plane of the two masses and the ζ axis perpendicular to the $\xi - \eta$ plane, along the angular momentum vector, in such a way that we have a
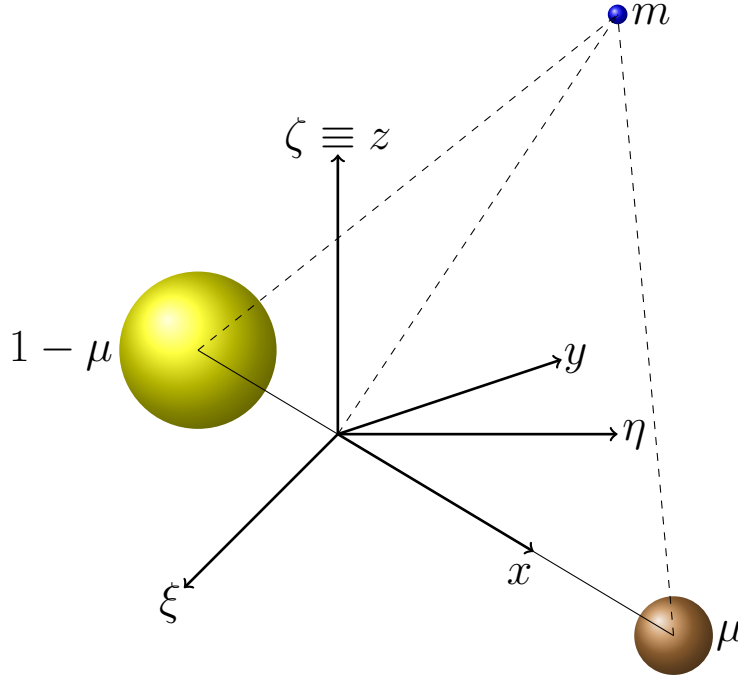
Figure 1.1: The restricted three body problem in the inertial and rotating reference frames.

right-hand system (see Fig. 1.1).

Let the coordinates of the two masses and the test particle, in this reference frame, be (ξ_1, η_1, ζ_1), (ξ_2, η_2, ζ_2) and (ξ, η, ζ) respectively. We chose the unit of mass in such a way that $m_1 + m_2 = 1$, and we assume $m_1 > m_2$. In a similar way, we choose the unit of distance so that the constant distance between the two primaries is unity and, also, the unit of time is chosen in order to make the gravitational constant equal to one. In this set of units, the mean motion of the two primaries $n = 2\pi/T = 1$, where T is the period of the circular motion. Let us consider now the mass parameter

$$\mu = \frac{m_2}{m_1 + m_2}$$

that stands for the ratio between the mass of the smaller primary to their total mass. Note that in our system of units we have

$$m_1 = 1 - \mu, \qquad m_2 = \mu, \qquad 0 < \mu < 1/2.$$

Now it is easy to derive the equations of the motion of the test particle, which are

given by

$$
\begin{cases}
\ddot{\xi} = (1-\mu)\dfrac{\xi_1 - \xi}{r_1^3} + \mu\dfrac{\xi_2 - \xi}{r_2^3}, \\[2mm]
\ddot{\eta} = (1-\mu)\dfrac{\eta_1 - \eta}{r_1^3} + \mu\dfrac{\eta_2 - \eta}{r_2^3}, \\[2mm]
\ddot{\zeta} = (1-\mu)\dfrac{\zeta_1 - \zeta}{r_1^3} + \mu\dfrac{\zeta_2 - \zeta}{r_2^3},
\end{cases}
$$

where

$$
r_1^2 = (\xi_1 - \xi)^2 + (\eta_1 - \eta)^2 + (\zeta_1 - \zeta)^2,
$$

$$
r_2^2 = (\xi_2 - \xi)^2 + (\eta_2 - \eta)^2 + (\zeta_1 - \zeta)^2.
$$

It is worth noting that these equations depend explicitly on the time, as the coordinates of the primaries change with it, but in a known way. This fact motivates the introduction of a new reference frame (x, y, z), rotating with the same angular velocity as the primaries, in order to fix their position. Thus, we define the following coordinate transformation

$$
\xi = x\cos t - y\sin t, \quad \eta = x\sin t + y\cos t, \quad \zeta = z. \tag{1.1}
$$

Differentiating twice these equations we obtain

$$
\begin{cases}
\ddot{\xi} = (\ddot{x} - 2\dot{y} - x)\cos t - (\ddot{y} + 2\dot{x} - y)\sin t, \\[2mm]
\ddot{\eta} = (\ddot{x} - 2\dot{y} - x)\sin t + (\ddot{y} + 2\dot{x} - y)\cos t, \\[2mm]
\ddot{\zeta} = \ddot{z}.
\end{cases}
\tag{1.2}
$$

Note that the switch to a rotating reference frame has introduced terms in $\dot{x}$ and $\dot{y}$, accounting for the Coriolis acceleration, and in x and y, that accounts for the centrifugal acceleration. Now, using (1.1) and (1.2), and, after a straightforward manipulation, the equations of motion become

$$
\begin{cases}
\ddot{x} - 2\dot{y} - x = -(1-\mu)\dfrac{x - x_1}{r_1^3} - \mu\dfrac{x - x_2}{r_2^3}, \\[2mm]
\ddot{y} + 2\dot{x} - y = -(1-\mu)\dfrac{y - y_1}{r_1^3} - \mu\dfrac{y - y_2}{r_2^3}, \\[2mm]
\ddot{z} = -(1-\mu)\dfrac{z}{r_1^3} - \mu\dfrac{z}{r_2^3}.
\end{cases}
\tag{1.3}
$$

It is possible to choose the direction of the x axis in such a way that the two primaries lie on it. In this case, we set $y_1 = y_2 = 0$ and, by virtue of the choice of units and taking into account that the origin of the reference frame is at the centre of mass, we can take

$$
x_1 = -\mu, \qquad x_2 = 1 - \mu.
$$

Thus, the equations (1.3) reduce to

$$\begin{cases} \ddot{x} - 2\dot{y} = x - (1 - \mu)\dfrac{x + \mu}{r_1^3} - \mu\dfrac{x - 1 + \mu}{r_2^3}, \\[2mm] \ddot{y} + 2\dot{x} = y - (1 - \mu)\dfrac{y}{r_1^3} - \mu\dfrac{y}{r_2^3}, \\[2mm] \ddot{z} = -(1 - \mu)\dfrac{z}{r_1^3} - \mu\dfrac{z}{r_2^3}, \end{cases} \tag{1.4}$$

where

$$r_1 = \sqrt{(x + \mu)^2 + y^2 + z^2}, \qquad r_2 = \sqrt{(x - 1 + \mu)^2 + y^2 + z^2}.$$

These equations can be written in terms of the so called effective potential function, $U(x, y, z)$, defined as

$$U = \frac{1}{2}(x^2 + y^2) + \frac{1 - \mu}{r_1} + \frac{\mu}{r_2}, \tag{1.5}$$

so that (1.4) become

$$\ddot{x} - 2\dot{y} = \frac{\partial U}{\partial x}, \quad \ddot{y} + 2\dot{x} = \frac{\partial U}{\partial y}, \quad \ddot{z} = \frac{\partial U}{\partial z}.$$

Multiplying the first equation by $2\dot{x}$, the second one by $2\dot{y}$ and the third one by $2\dot{z}$ and adding together, we find

$$2\dot{x}\ddot{x} + 2\dot{y}\ddot{y} + 2\dot{z}\ddot{z} = 2\frac{\partial U}{\partial x}\dot{x} + 2\frac{\partial U}{\partial y}\dot{y} + 2\frac{\partial U}{\partial z}\dot{z}.$$

Integrating respect to time results

$$\dot{x}^2 + \dot{y}^2 + \dot{z}^2 = 2U - C,$$

where C is a constant that is known as the *Jacobi constant* or integral. Sometimes the Jacobi constant is referred as the energy integral. However, this is not correct, since the Jacobi constant does not express the conservation of the energy. Indeed, what is constant is the energy of the two body system constituted by the two primaries, but not the energy of the test particle, so that the total energy is not conserved. The Jacobi constant serves to introduce the Hamiltonian formalism to the equations of the motion. Let us consider the function

$$H = -\frac{C}{2} = \frac{1}{2}(\dot{x}^2 + \dot{y}^2 + \dot{z}^2) - U,$$

and let us introduce the momenta p_x, p_y, p_z by means of the relations

$$p_x = \dot{x} - y, \qquad p_y = \dot{y} + x, \qquad p_z = \dot{z}, \tag{1.6}$$

so that the Hamiltonian function H becomes

$$H = \frac{1}{2}(p_x^2 + p_y^2 + p_z^2) - (xp_y - yp_x) - \frac{\mu}{r_1} - \frac{1-\mu}{r_2}.$$

Then, the system (1.4) of three differential equations of second order can be written as a system of six differential equations of first order given by

$$\dot{x} = \frac{\partial H}{\partial p_x}, \ \ \dot{y} = \frac{\partial H}{\partial p_y}, \ \ \dot{z} = \frac{\partial H}{\partial p_z}, \ \ \dot{p}_x = -\frac{\partial H}{\partial x}, \ \ \dot{p}_y = -\frac{\partial H}{\partial y}, \ \ \dot{p}_z = -\frac{\partial H}{\partial z}.$$

This form of the equations is more convenient and we will make use of them instead of the equations (1.4).

It is worth noticing that the plane $z = 0$ is invariant. That is to say, if at the initial time $z(t_0) = p_z = t_0$, then $z(t) = p_z(t) = 0$ for all $t \in \mathbb{R}$, as it follows from the third equation in (1.4). This fact leads to the planar restricted three-body problem, which is simpler to manage than the spatial one. In what follows we will consider this case and we will not take into account the z coordinate. Thus our system of differential equations reduces to

$$\begin{cases} \dot{x} &=& \dfrac{\partial H}{\partial p_x} &=& p_x + y, \\[2mm] \dot{y} &=& \dfrac{\partial H}{\partial p_y} &=& p_y - x, \\[2mm] \dot{p}_x &=& -\dfrac{\partial H}{\partial x} &=& p_y - \mu\dfrac{x+\mu}{r_1^3} - (1-\mu)\dfrac{x-1+\mu}{r_2^3}, \\[2mm] \dot{p}_y &=& -\dfrac{\partial H}{\partial y} &=& -p_x - \mu\dfrac{y}{r_1^3} - (1-\mu)\frac{y}{r_2^3}. \end{cases} \tag{1.7}$$

1.1.1   The Jacobi integral and zero velocity curves

For the planar case, the Jacobi integral gets reduced to

$$C = x^2 + y^2 + 2\frac{1-\mu}{r_1} + 2\frac{\mu}{r_2} - \dot{x}^2 - \dot{y}^2, \tag{1.8}$$

where
$$r_1 = \sqrt{(x+\mu)^2 + y^2}, \qquad r_2 = \sqrt{(x-1+\mu)^2 + y^2}.$$

The Jacobi constant serves to determine the so called *zero-velocity curves*, which are those curves where the velocity of the small mass is equal to zero. They can

also be viewed as the level contours of twice the Hamiltonian function, when the velocity is equal to zero. That is to say, the level contours of the function

$$-\left(x^2 + y^2 + 2\frac{1-\mu}{r_1} + 2\frac{\mu}{r_2}\right) = -2U.$$

They determine the regions where the motion of the small particle can take place. The shape of the zero velocity curves depends on the value of the mass parameter μ. In Figure 1.2 we show different situations for three different values of μ. In the top left panel is depicted the extreme case $\mu = 0.5$, known as the Copenhagen case. The other two cases consider smaller values of the mass parameter, being the smallest one that corresponding to Jupiter.

We note that the movement of the small particle takes place in the region where $-2U$ is not greater than the initial value. Otherwise it means that the particle could take negative kinetic energy. In this way, the colored curves play an important role, as they separate bounded from unbounded motion. These curves are homoclinic loops connecting critical points of the effective potential. The equilibrium points are named L_1, L_2 and L_3. The first one is located in between the two primaries. L_2 is located in the positive part of the x axis, to the right of the small primary, and L_3 is located in the negative part of the x axis, to the left of the big primary. Besides these three critical points, there are two other critical points, L_4 and L_5, forming an equilateral triangle with the primaries. These two points correspond to stable positions, where a numerous set of asteroids have been found in the case of Jupiter, like the Trojan asteroids that go ahead and behind Jupiter in its orbit around the Sun.

The homoclinic loops evolve with the mass parameter and, if it is small enough, the loops attached to L_1 and L_2 are almost the same, and also their Jacobi constant. Moreover, the location of L_1 and L_2 is approximately symmetric respect to the small primary and all of these facts suggest a new approximation of the problem, if we are considering the motion in a neighborhood of the small primary. This yields Hill's approximation.

1.2 Hill approximation

The Hill approximation describes the most relevant features of the dynamics of the infinitesimal particle around the small primary, when the mass parameter is small enough. The idea comes from a seminal paper of G. H. Hill [Hil78] published in 1878 about the motion of the Moon. Curiously, this idea was used in Hill's previous work, published in 1877, to explain the motion of the Lunar perigee [Hil86]. The result is a simplified version of the three-body problem.
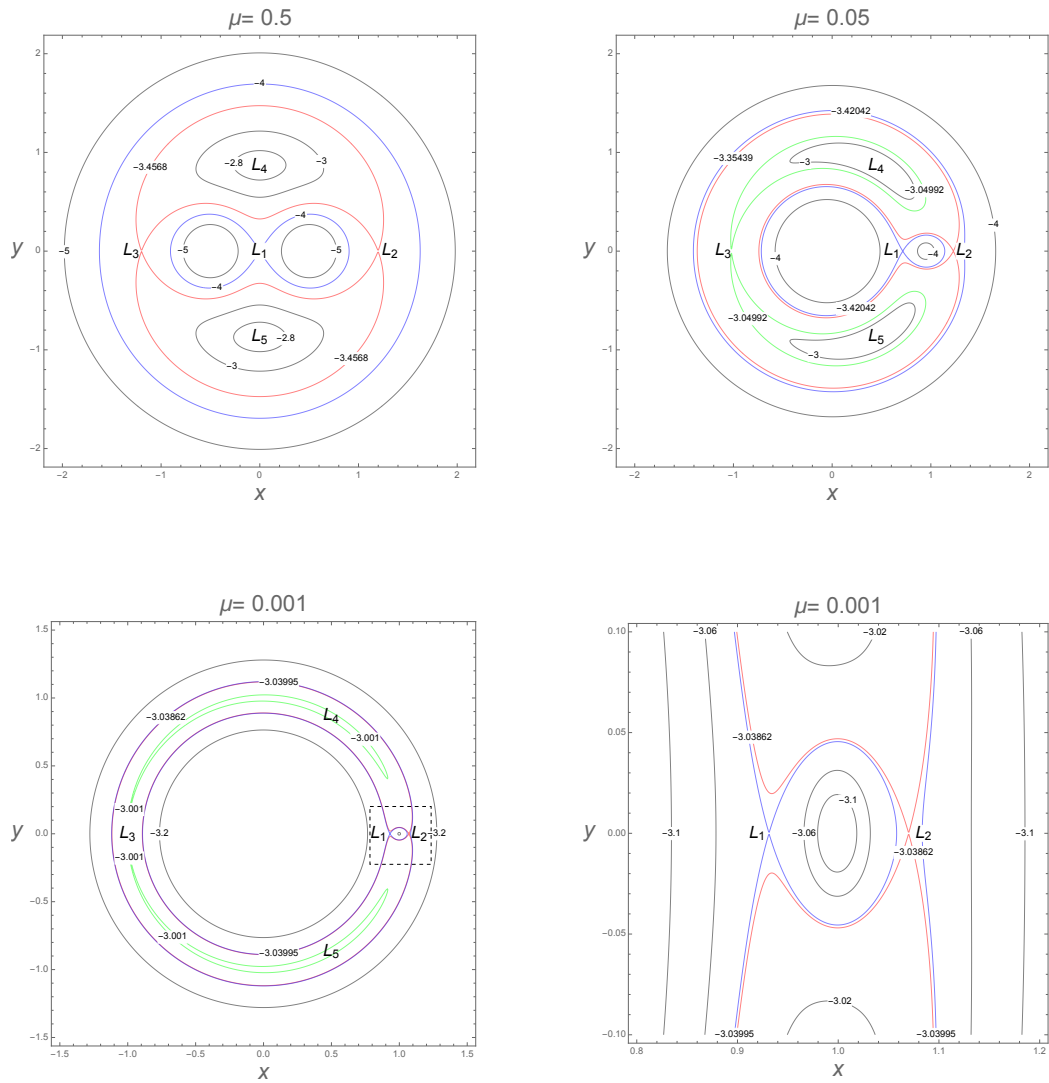
Figure 1.2: Zero velocity curves for different values of the mass parameter μ. For the left bottom panel a magnification of the boxed area is depicted in the right.

In the Hill approximation, the first step is a change of the reference frame, moving the origin to the center of mass of the small primary. This is done by a translation along the x axis, in such a way that we introduce a new x coordinate by means of

$$x \to \bar{x} + 1 - \mu.$$

For the sake of simplicity, we maintain the name of the variables, so that after the change of coordinates $\bar{x}$ is replaced by x. Now, the distance of the particle to the two primaries is given by

$$r_1 = \sqrt{(x+1)^2 + y^2}, \qquad r_2 = \sqrt{x^2 + y^2},$$

while the derivatives remain the same for the old and new variables. In this way, the only affected terms in the equations of the motion (1.4) are those coming from the potential

$$U = \frac{1}{2}((x+1-\mu)^2 + y^2) + \frac{1-\mu}{r_1} + \frac{\mu}{r_2}.$$

Now we take advantage of the fact that x and y are small when moving in the vicinity of the small primary, so that we can expand U in power series of x and y. In this way, neglecting terms of third order and higher we arrive to

$$U = \frac{1}{2}\left[\mu^2 + 3(1+x^2) - \mu(4 + 2x^2 - y^2))\right] + \frac{\mu}{r_2}.$$

We note that μ is also small and that the constant terms in U do not affect the equations of the motion, so that we can suppress both constant terms and terms of the form μx^2 and μy^2, provided we are neglecting powers of third order and higher. Thus, the potential function for the Hill approximation is given by

$$U_H = \frac{3}{2}x^2 + \frac{\mu}{r_2}, \qquad r_2 = \sqrt{x^2 + y^2}, \tag{1.9}$$

and the equations of the motion by

$$\begin{aligned}
\ddot{x} - 2\dot{y} &= \frac{\partial U_H}{\partial x} = 3x - \mu\frac{x}{r_2^3}, \\
\ddot{y} + 2\dot{x} &= \frac{\partial U_H}{\partial y} = -\mu\frac{y}{r_2^3}.
\end{aligned} \tag{1.10}$$

As in the case of the restricted three body problem these equations admit a Hamiltonian formalism. Introducing again the conjugate momenta, by means of (1.6), we obtain a system of four differential equations of first order from the Hamiltonian function

$$H = \frac{1}{2}(p_x^2 + p_y^2) - (xp_y - yp_x) + \frac{1}{2}(x^2 + y^2) - \frac{3x^2}{2} - \frac{\mu}{\sqrt{x^2 + y^2}}. \tag{1.11}$$
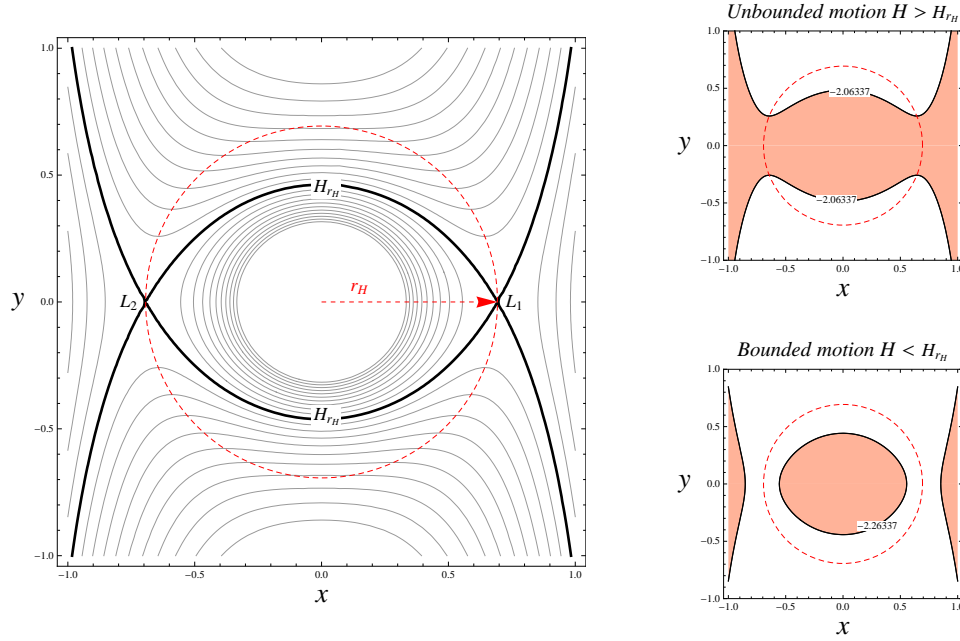
Figure 1.3: Zero velocity curves for the Hill approximation in scaled coordinates. In the right panel the colored regions are those where the small body can move, for a prescribed value of the Hamiltonian function. The Hill's sphere is the dashed red circle.

Indeed, H is a constant of motion, related with a new Jacobi constant which helps to define the zero velocity curves, as in the case of the planar restricted three body problem. These curves are the level contours of U_H, that possesses two saddle points, L_1 and L_2, located on the x axis, symmetric with respect to the origin, at a distance

$$r_H = \sqrt[3]{\frac{\mu}{3}}. \tag{1.12}$$

Here, r_H is known as the Hill's radius and define an imaginary sphere around the small primary which can be viewed as its gravitational sphere of influence. At the saddle points, as the velocity is zero, the Hamiltonian function (1.11) takes the value

$$H_{r_H} = -\frac{3}{2}\sqrt[3]{3\mu^2}.$$

It is worth noting that, if the value of the Hamiltonian function for an infinitesimal mass is less than H_{r_H}, then the particle of infinitesimal mass cannot escape the Hill's sphere. However, if the value of the Hamiltonian is greater than H_{r_H} the mass can escape the influence of the small primary and move far from it. The

escape takes place through a *gate* around the saddle points. This is depicted in Figure 1.3, where in the left panel several zero velocity curves are plotted. Highlighted is the loop connecting the two saddle points that separates the bounded and unbounded motions.

In Figure 1.3 the value of the mass parameter does not appear. In fact, Hill's approximation is independent of it, if convenient scaled variables are used. In this way, let us introduce the new coordinates and momenta by means of

$$x = \mu^{1/3}\,\bar{x}, \quad y = \mu^{1/3}\,\bar{y}, \qquad p_x = \mu^{1/3}\,\bar{p}_x, \quad p_y = \mu^{1/3}\,\bar{p}_y.$$

This is a canonical change of variables with multiplier $\lambda = \mu^{-2/3}$. Therefore, the new Hamiltonian function (1.11) becomes [MHO09]

$$H = \lambda\mu^{2/3}\left(\frac{1}{2}(\bar{p}_x^2 + \bar{p}_y^2) - (\bar{x}\bar{p}_y - \bar{y}\bar{p}_x) + \frac{1}{2}(\bar{x}^2 + \bar{y}^2) - \frac{3\bar{x}^2}{2} - \frac{1}{\sqrt{\bar{x}^2 + \bar{y}^2}}\right)$$

Taking into account that $\lambda = \mu^{-2/3}$, and omitting the bars for the new variables, we get a Hamiltonian system independent of the mass parameter, defined by the function

$$H = \frac{1}{2}(p_x^2 + p_y^2) - (xp_y - yp_x) + \frac{1}{2}(x^2 + y^2) - \frac{3x^2}{2} - \frac{1}{\sqrt{x^2 + y^2}}. \quad (1.13)$$

Thus, we do not need to consider different values of the mass parameter to have a description of the Hill's approximation. All we can say for the Hamiltonian (1.13) can be said for the Hamiltonian (1.11). In particular, to have a qualitative picture of the motion, for different values of the Hamiltonian function, Poincaré surfaces of section can be used. They provide useful information about the trapped and escape dynamics for both prograde and retrograde motions.

1.2.1   Poincaré surfaces of section for the Hill's approximation

Let us consider the orbits in the phase space of the Hamiltonian system defined by (1.13). Due to the fact that the Hamiltonian function H is an integral of the motion, fixing its value to h, all the orbits lie on the three dimensional surface defined by

$$H(x, y, p_x, p_y) = h, \quad (1.14)$$

which is embedded into the four dimensional phase space $\mathbb{R}^4$. In this way, we can consider the orbits in the phase space (x, y, p_x), provided p_y is obtained from the constrain (1.14).

Now, we define a Poincaré surface of section as a hyperplane, S, that is transversal to the orbits of the Hamiltonian system. As S intersect every orbit,

we can consider the *first return or Poincaré map* $P : S \to S$ in such a way that $P(p_0) = p_1$, where p_1 is the point for which the orbit with initial value p_0, when $t = 0$, intersects S for the first time. The sequence of points $P^n(p_0)$ represents the successive intersections of a given orbit with the surface S and some properties of the Hamiltonian system and their orbits can be deduced from the Poincaré map.

The importance of the surface of sections is that the Hamiltonian system gets reduced to a map that it turns to be two dimensional if the system is two degrees of freedom, as it is the case of our problem. In this case, the hyperplane is just a plane and it is easy to visualize the main topological properties of the system. As H is even in p_x, the plane $p_x = 0$, that is the plane (x, y), is a surface of section, provided that, by means of the constrain (1.14), once the Hamiltonian function is fixed to h, we obtain p_y as

$$p_y = x \pm \sqrt{2h + 3x^2 - y^2 + \frac{2}{\sqrt{x^2 + y^2}}}.$$

Indeed, it can be seen that almost every orbit starting inside the zero velocity curve

$$U_H = \frac{3}{2}x^2 + \frac{1}{r} = -h$$

with $\dot{y} > 0$ intersects $p_x = 0$ with $\dot{y} > 0$ an infinite number of times, if the corresponding zero velocity curve is closed. That is to say if

$$h < H_{r_H} = -\frac{3\sqrt[3]{3}}{2}.$$

In this way, the limit of the Poincaré surface of section is given by the zero velocity curve corresponding to $U_H = -h$.

One of the main characteristics of a Poincaré surface of section is that an orbit lying on a toroidal surface, defined by the Hamiltonian function H, and by other formal integral $\Phi(x, y, p_x, p_y) = c$, intersects the section in a sequence of points lying on a curve, called an invariant curve. Many of these curves surround fixed points, that correspond to periodic orbits, while the invariant curves represent quasi periodic motions. Irregular or chaotic motions appear in the Poincaré surface of section as a collection of points filling an area of nonzero measure [Con02].

Let us now turn to our particular case, and consider the surfaces of section for different values of the Hamiltonian function. Concretely, we fix four values of h, the first one below H_{r_H} and the other three above this value. This sections are depicted in Figure 1.4 where the the section is given by $p_x = 0$ and the points are those returning to the surface of section with $p_y > 0$. The red color stand for those orbits in prograde motion when crossing the surface, while green color
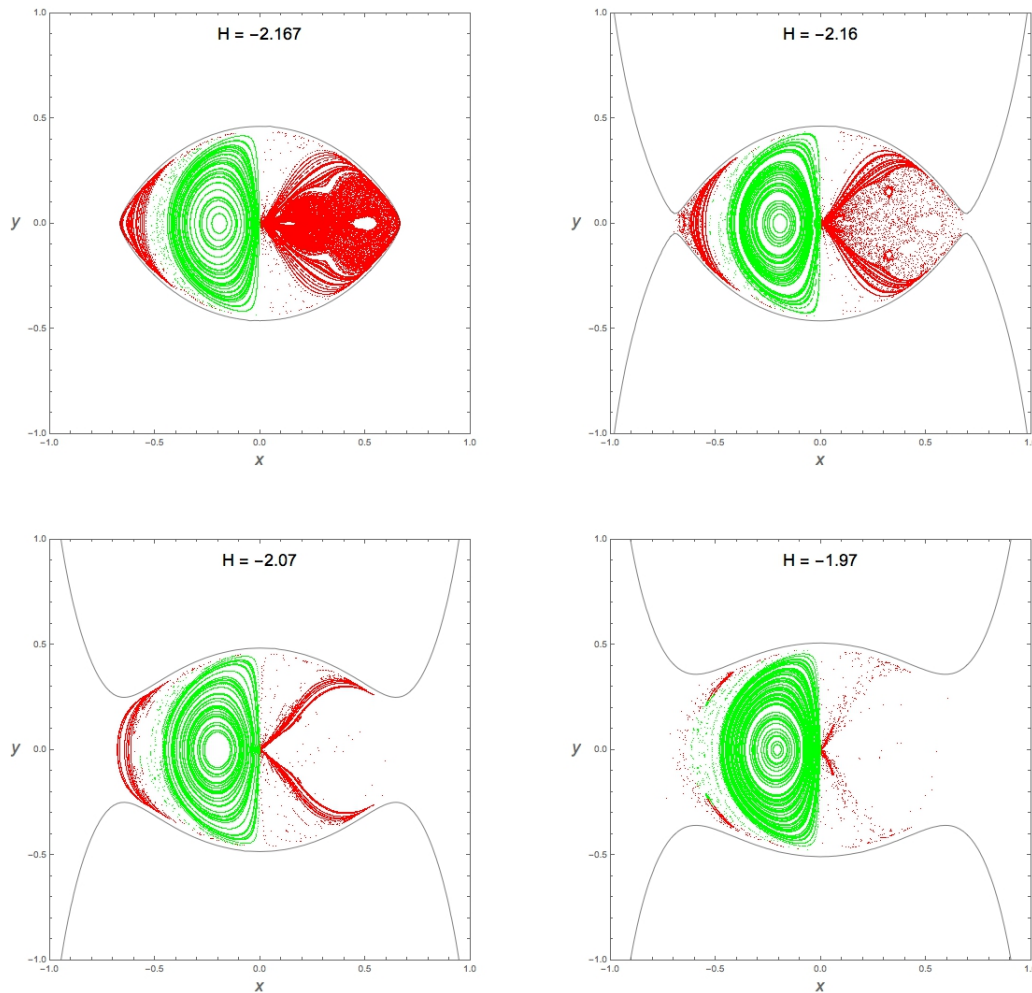
Figure 1.4: Poincaré surfaces of section in the Hill problem for four different values of the Hamiltonian function. The sections defined as $p_x = 0$, with $\dot{y} > 0$. The color for the points is assigned depending on the angular momentum as the orbits intersect the section. The red color stands for prograde motion, while green color stands for retrograde one.

stands for retrograde motion. We can see that, for $h = -2.167$ the motion is bounded, but retrograde orbits are mostly confined to invariant curves. However, prograde orbits, especially those located in the right side of the section are irregular and oriented in the x direction towards the position of the saddle point. When h is slightly above H_{r_H} prograde orbits oriented to the right saddle point start to escape. As the value of h increases, most of the prograde orbits in the right side of the section escape, but the retrograde ones still remain in stable quasi periodic motions. It is worth noticing that orbits in the leftmost part of the section are not always retrograde nor prograde, but of mixed type (see the last right panel of Figure 1.4). For high values of h most of the prograde orbits have disappeared, which indicates that objects temporally trapped into the Hill sphere are most likely to be in retrograde morion around the primary. This can be an indicator of why there is a preference of irregular satellites for retrograde orbits.

1.2.2   Regularization of the Hill problem

The differential equations derived from Hamiltonian (1.13) provide an adequate description of the motion of the small body when it does not collide with the primary. If a collision takes place, the corresponding Hamiltonian and the equations of the motion are singular. To overcome this situation, a transformation of both the space and time variables, called a *regularization*, is performed. This idea goes back to Euler, but it was Levi-Civita who introduced the basic ideas of this technique [LC20] for the planar case, generalized later on by Kustaanheimo and Stiefel [KS65] for the spatial one. Historically, regularization was conceived for the treatment of singularities in the Keplerian motion as well as for the description of collisions of two masses, as well as for the improvement of the numerical integration of collision and near-collision orbits. It is this last aspect that we are interested in, as a huge number of orbits are going to be considered and close encounters are very likely to take place.

The Levi-Civita regularization is based in three steps, following the Waldvogel terminology

- **First step: Slow motion movie**. Instead of the physical time t a new independent variable τ, the ficticious time, is introduced in such a way that the movie is run in slow motion when the bodies are close.

- **Second step: Conformal squaring**. In this step, the complex physical coordinates $\mathbf{x} = x + iy$ are represented as the square $\mathbf{z}^2$ of a complex variable $\mathbf{z} = u + iv$.

- **Third step: Fixing the energy**. In the final step, only orbits of fixed Jacobi constant are considered.

In practice, the first and second steps are performed in the reverse order, that is, we first do the coordinate transformation, followed by the time scaling. In this way, we consider the position of the particle of infinitesimal in the plane case, by the complex vector

$$\mathbf{x} = x + iy,$$

where x, y are the cartesian coordinates with respect to a coordinate system centered at the small primary. In a similar way, we introduce the complex momentum

$$\mathbf{P} = p_x + ip_y,$$

being p_x, p_y the conjugate momenta.

Now, we define the new coordinates u, v, by the conformal transformation

$$\mathbf{x} = \mathbf{z}^2, \tag{1.15}$$

where $\mathbf{z} = u + iv$. In order to preserve the canonical form of the equations of motion, new momenta U, V and a complex variable $\mathbf{\Pi} = U + iV$ are introduced such that the transformation to the new variables is canonical. To this end, we define the new momenta by considering the conformal transformation $\mathbf{x} = \mathbf{x}(u, v)$ or $\mathbf{z} = \mathbf{z}(x, y)$, where $\mathbf{x}(u, v)$ is an analytic function. Now, by means of the generating function $G(x, y, U, V)$, we obtain

$$u = \frac{\partial G}{\partial U}, \quad v = \frac{\partial G}{\partial V}, \quad p_x = \frac{\partial G}{\partial x}, \quad p_y = \frac{\partial G}{\partial y}. \tag{1.16}$$

Integration of the first two of these equations yields

$$G = Uu(x, y) + Vv(x, y), \tag{1.17}$$

and the last two equations in (1.16) become

$$p_x = U\frac{\partial u}{\partial x} + V\frac{\partial v}{\partial x}, \quad p_y = U\frac{\partial u}{\partial y} + V\frac{\partial v}{\partial y}, \tag{1.18}$$

which, in terms of the complex notation, can be written as

$$\mathbf{P} = \mathbf{\Pi}\frac{\overline{d\mathbf{z}}}{d\mathbf{x}}, \tag{1.19}$$

where the bar denotes complex conjugate. Note that, by means of equation (1.15), we can write

$$\mathbf{P} = \frac{\mathbf{\Pi}}{2\mathbf{z}}. \tag{1.20}$$

Equations (1.15) and (1.20) defines a completely canonical transformation (multiplier $\lambda = 1$). However, we will consider a canonical transformation of multiplier $\lambda = 1/4$ used in the literature [SS00, LR11] given by

$$\mathbf{P} = 2\frac{\mathbf{\Pi}}{\mathbf{z}}, \tag{1.21}$$

that in explicit form reads as

$$x = u^2 - v^2, \quad y = 2uv, \quad p_x = 2\frac{uU - vV}{u^2 + v^2}, \quad p_y = 2\frac{uV + vU}{u^2 + v^2}. \tag{1.22}$$

Substitution in Hamiltonian (1.13) gives

$$H = \frac{2(U^2 + V^2) - 1}{u^2 + v^2} - 2(uV - vU) - (u^2 - v^2)^2 + 2u^2v^2.$$

In a non rigorous way, we perform an overall multiplication by $(u^2 + v^2)/4$ in order eliminate the denominator. By doing so, we arrive to

$$\frac{u^2 + v^2}{4}H = \frac{U^2 + V^2}{2} - \frac{1}{4}\left(2(uV - vU) + u^4 - 4u^2v^2 + v^4\right)(u^2 + v^2) - \frac{1}{4}.$$

This is, in fact, the first step of Levi-Civita regularization, when a fictitious time is introduced by means of

$$d\tau = 4\frac{dt}{r},$$

where $r = \sqrt{x^2 + y^2} = u^2 + v^2$.

To complete the regularization process, we set the value of the Hamiltonian to be h and we arrive to the pseudo-Hamiltonian

$$K = \frac{U^2 + V^2}{2} - \left(\frac{1}{2}(uV - vU) + \frac{1}{4}(u^4 - 4u^2v^2 + v^4) + \frac{h}{4}\right)(u^2 + v^2), \tag{1.23}$$

where K has a constant value equal to $1/4$. Now the equations of the motion, in the regularized variables and time, are

$$\frac{du}{d\tau} = \frac{\partial K}{\partial U}, \quad \frac{dv}{d\tau} = \frac{\partial K}{\partial V}, \quad \frac{dU}{d\tau} = -\frac{\partial K}{\partial u}, \quad \frac{dV}{d\tau} = -\frac{\partial K}{\partial v}, \tag{1.24}$$

which are not singular when a collision takes place.

It is possible to arrive to a more simplified Hamiltonian and equations of the motion by means of a new canonical change of variables. Indeed, let $h = -2c$ and consider the scaling

$$u = 2c^{1/4}\hat{u}, \quad v = 2c^{1/4}\hat{v}, \quad U = 2c^{3/4}\hat{U}, \quad V = 2c^{3/4}\hat{V}.$$

The simplified Hamiltonian becomes

$$H = H_2 + H_4 + H_6, \tag{1.25}$$

where

$$H_2 = \tfrac{1}{2}(u^2 + v^2 + U^2 + V^2),$$

$$H_4 = 2(u^2 + v^2)(vU - uV),$$

$$H_6 = -4(u^6 + v^6 - 3u^4v^2 - 3u^2v^4).$$

We note that this expression for the regularized Hill Hamiltonian is free of parameters, as it was the departure one. Moreover, the new Hamiltonian is no longer constant and it is related with the original one through the multiplier of the canonical transformation $\lambda = \tfrac{1}{4}c^{-3/2}$. In this way, if h is the value of the Hamiltonian function in cartesian variables, then the value of the Hamiltonian function in the fully regularized form is

$$h_R = \frac{1}{2}\left(\frac{|h|}{2}\right)^{-3/2} = \frac{1}{2}|c_H|^{-3/2},$$

where $c_H = -2h$ is the value of Jacobi constant for the Hill problem. Although (1.25) is preferable to study periodic orbits and other invariant structures [SS00], we will consider (1.23) for the numerical computations. This is because it is the more convenient way to go from cartesian to regularized coordinates and back. Indeed, equations (1.22) give us the change from regularized to cartesian coordinates. This transformation is a mapping, provided that, for a given quadruplet (u, v, U, V), there is a unique quadruplet (x, y, p_x, p_y) through the action of the transformation. However the mapping is not injective, because of (1.15). As a consequence, for each pair (x, y) of cartesian coordinates there are two pairs (u, v) of regularized ones, so that the Levi-Civita regularization makes a double covering. This can be viewed in Figure 1.5. The argument of **x** is halved and each quadrant in the complex plane (x, y) is mapped onto two octants in the complex plane (u, v), symmetric respect to the origin. For instance, the first quadrant goes to the first and fifth octants and analogously for the other three quadrants. The direct transformation can be written as
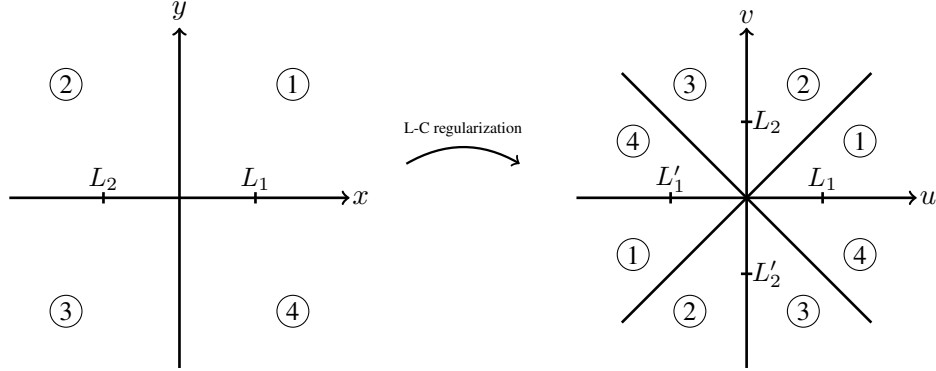
Figure 1.5: The double covering of the Levi-Civita regularization. Each point in cartesian variables transforms into two points in regularized coordinates.

$$
\begin{cases}
u = \pm \dfrac{y}{|y|} \sqrt{\dfrac{x + \sqrt{x^2 + y^2}}{2}}, \\[3ex]
v = \pm \dfrac{|y|}{\sqrt{2x + 2\sqrt{x^2 + y^2}}}, \\[3ex]
U = \pm \dfrac{\sqrt{x + \sqrt{x^2 + y^2}}\left(yp_x - p_y(x - \sqrt{x^2 + y^2})\right)}{2\sqrt{2}|y|}, \\[3ex]
V = \pm \dfrac{\sqrt{x + \sqrt{x^2 + y^2}}\left(yp_y + p_x(x - \sqrt{x^2 + y^2})\right)}{2\sqrt{2}|y|},
\end{cases}
\tag{1.26}
$$

where the $\pm$ sign is the consequence of the double covering, both in coordinates and momenta.

The apparent inconvenient of equations (1.26) is the choice of sign. Indeed, we use the switch from cartesian to regularized coordinates for numerical integration purpose, so that initial values of an orbit in cartesian variables are transformed into regularized coordinates and then integrated numerically. At the end, we go back to the cartesian variables through the mapping (1.22). However, is there any difference between the orbits if we choose different sign for the first transformation? The answer is not and, it does not matter the sign we choose in (1.26), the final orbit is the same. As an example, we consider an orbit with initial conditions

y

v

0.5

u
−1.0   −0.5   0.5   1.0

−0.5

Regularized coordinates

v

0.5

u
−1.0   −0.5   0.5

−0.5

0.6

0.4

0.2

−0.5   0.5   1.0   x
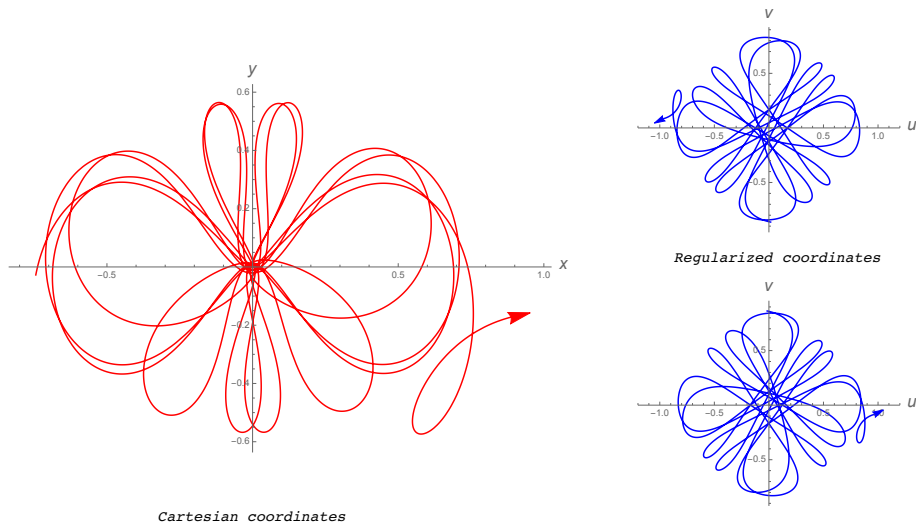
−0.2

−0.4

−0.6

Cartesian coordinates

Figure 1.6: Two copies of the same orbit in regularized coordinates.

in cartesian variables given by

$$x = -0.744249, \quad y = -0.027428, \quad p_x = 0.209091, \quad p_y = 0.206899.$$

In regularized coordinates, we obtain the two starting points

$$(u_1, v_1, U_1, V_1) \equiv (-0.015894, 0.862845, 0.087599, -0.091851),$$
$$(u_2, v_2, U_2, V_2) \equiv (0.015894, -0.862845, -0.087599, 0.091851),$$

given rise to two copies of the same orbit in cartesian variables, as it is depicted in Figure 1.6.

Chapter 2

The Restricted 2+2-Body Problem

The restricted three-body problem, in the Hill approximation, is a good model to describe the motion of a small object in the vicinity of a planet. However, this description is not enough to account for a permanent capture of an object. It is necessary that there also exists a mechanism that forces the object to change its energy in such a way it can be trapped in a stable island or even more, it loses enough energy (below the energy of the saddle point) to become permanent trapped in the Hill sphere. This can be achieved by means of the interaction with another body in a close encounter, as it is illustrated in Figure 3.8.
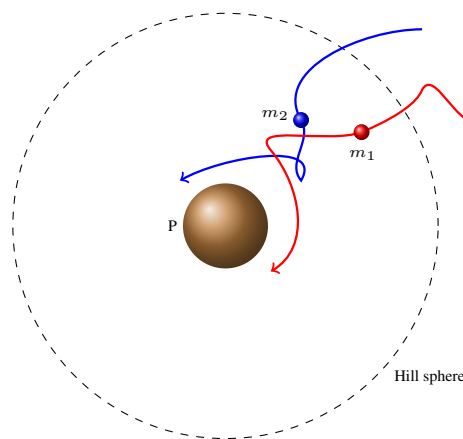

Figure 2.1: Close encounter of two minor bodies in the vicinity of a planet as a model of a capture mechanism.

In order to model this situation we consider a particular case of the restricted $n + \nu$ problem, described by Whipple and Szebehely [WS84], that Whipple used later on to study the stability of binary asteroids [Whi84, WW85]. In particular,
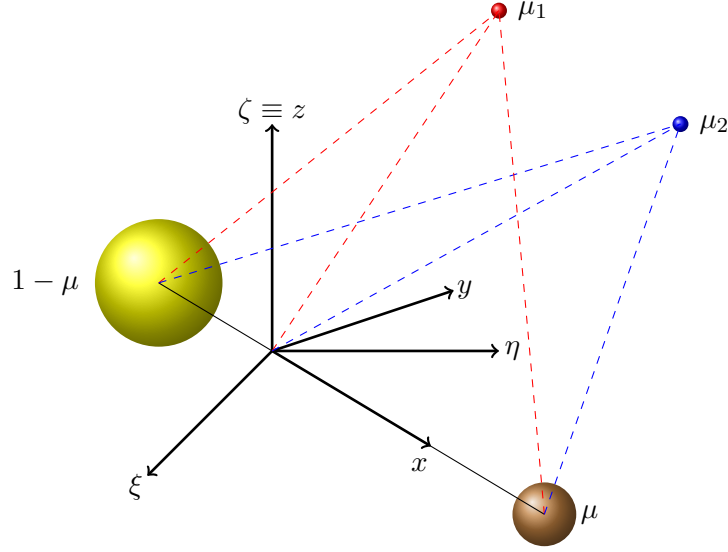
Figure 2.2: The restricted problem of $2 + 2$ bodies in a synodic reference frame.

we consider the restricted problem of $2+2$ bodies, where two primaries of masses $M_1 \gg M_2$ revolve in a circular orbit about their center of mass. Two small bodies, $m_{1,2} \ll M_2$, move under the attraction of the primaries, and their mutual attraction, in such a way that they do not exert any influence on the primaries.

Let us consider a synodic reference frame and appropriate units of length and time, as it was done in the restricted three body problem, and let us introduce the mass parameters

$$\mu = \frac{M_2}{M_1 + M_2}, \qquad \mu_i = \frac{m_i}{M_1 + M_2}, \ i = 1, 2, \tag{2.1}$$

In this reference system the two primaries are fixed located on the x axis (see Figure 2.2) and the equations of the motion of the two small bodies are given by [Whi84]

$$\ddot{x}_i - 2\dot{y}_i = \frac{1}{\mu_i} \frac{\partial U}{\partial x_i}, \quad \ddot{y}_i + 2\dot{x}_i = \frac{1}{\mu_i} \frac{\partial U}{\partial y_i}, \quad \ddot{z}_i = \frac{1}{\mu_i} \frac{\partial U}{\partial z_i}, \quad i = 1, 2, \tag{2.2}$$

where the effective potential function U is defined as

$$U = \sum_{i=1}^{2} \mu_i \left(\frac{x_i^2 + y_i^2}{2} + \frac{1 - \mu}{r_{1i}} + \frac{\mu}{r_{2i}} + \frac{\mu_{3-i}}{2r} \right), \tag{2.3}$$

being

$$r_{1i} = \sqrt{(x_i + \mu)^2 + y_i^2 + z_i^2}, \quad r_{2i} = \sqrt{(x_i - 1 + \mu)^2 + y_i^2 + z_i^2}, \, i = 1, 2,$$

$$r = \sqrt{(x_1 - x_2)^2 + (y_1 - y_2)^2 + (z_1 - z_2)^2}.$$

Proceeding in the same way as in the restricted three-body problem, we find a generalized Jacobi integral [SW84]

$$C = -\sum_{i=1}^{2} \mu_i \left[(\dot{x}_i^2 + \dot{y}_i^2 + \dot{z}_i^2) - (x_i^2 + y_i^2) - 2\frac{1 - \mu}{r_{1i}} - 2\frac{\mu}{r_{2i}} - \frac{\mu_{3-i}}{r} \right].$$

After introducing the conjugate momenta

$$\dot{x}_i = \frac{p_{x_i}}{\mu_i} + y_i, \qquad \dot{y}_i = \frac{p_{y_i}}{\mu_i} - x_i, \qquad \dot{z}_i = \frac{p_{z_i}}{\mu_i}, \quad i = 1, 2. \qquad (2.4)$$

we obtain the Hamiltonian function, $H = -C/2$, given by

$$H = \sum_{i=1}^{2} \left[\frac{1}{2\mu_i} (p_{x_i}^2 + p_{y_i}^2 + p_{z_i}^2) + y_i p_{x_i} - x_i p_{y_i} - \mu_i \left(\frac{1 - \mu}{r_{1i}} + \frac{\mu}{r_{2i}} \right) \right] - \frac{\mu_1 \mu_2}{r},$$

which can be viewed as the sum of two independent restricted three body problems coupled by the last term. This term is negligible if the two minor bodies are far away and only contributes, or even dominates, when they come close enough.

2.1 Hill's approximation

The structure of the Jacobi constant and the Hamiltonian function suggests a similar approach to Hill's original treatment of the planar problem. Indeed, the orbital plane of the two primaries is invariant. In fact, if the two minor bodies start in the orbital plane with $\dot{z}_1 = \dot{z}_2 = 0$ they will remain there for every time. In this sense, to simplify the problem, we will restrict ourselves to the planar case, when $z_1 = z_2 = \dot{z}_1 = \dot{z}_2 = 0$. Therefore, the Jacobi constant becomes

$$C = -\sum_{i=1}^{2} \mu_i \left[(\dot{x}_i^2 + \dot{y}_i^2) - (x_i^2 + y_i^2) - 2\frac{1 - \mu}{r_{1i}} - 2\frac{\mu}{r_{2i}} - \frac{\mu_{3-i}}{r} \right], \qquad (2.5)$$

where

$$r_{1i} = \sqrt{(x_i + \mu)^2 + y_i^2}, \quad r_{2i} = \sqrt{(x_i - 1 + \mu)^2 + y_i^2}, \, i = 1, 2,$$

$$r = \sqrt{(x_1 - x_2)^2 + (y_1 - y_2)^2}. \qquad (2.6)$$

Now we follow step by step the sequence of transformations and approximations that led us to the Hill's Hamiltonian (1.13). First of all we move to a reference frame with the origin at the center of mass of the small primary by means of the translation

$$x \to \bar{x} + 1 - \mu.$$

For the sake of simplicity, we maintain the name of the variables, so that after the change of coordinates $\bar{x}$ is replaced by x, while the derivatives remain the same for the old and new variables. In this way, the only affected terms in the Jacobi constant (2.5) are those coming from twice the effective potential (2.3) that, after the translation becomes

$$U = \sum_{i=1}^{2} \mu_i \left[\frac{1}{2}((x_i + 1 - \mu)^2 + y_i^2) + \frac{1 - \mu}{r_{1i}} + \frac{\mu}{r_{2i}} + \frac{\mu_{3-i}}{2r} \right],$$

where the distances (2.6) are given by

$$r_{1i} = \sqrt{(x_i + 1)^2 + y_i^2}, \quad r_{2i} = \sqrt{x_i^2 + y_i^2}, \, i = 1, 2,$$
$$r = \sqrt{(x_1 - x_2)^2 + (y_1 - y_2)^2}.$$

Now, we acknowledge that x_i and y_i are small when moving in the vicinity of the small primary, so that we can expand r_{1i}^{-1} in power series of x_i and y_i and neglect terms of third order and higher. In this a way, we have

$$r_{1i}^{-1} \approx 1 - x_i + x_i^2 - \frac{1}{2}y_i^2, \quad i = 1, 2.$$

Finally,

$$\frac{1}{2}((x_i + 1 - \mu)^2 + y_i^2) + \frac{1 - \mu}{r_{1i}} \approx \frac{3}{2} - 2\mu + \frac{\mu^2}{2} + \frac{3}{2}x_i^2, \quad i = 1, 2.$$

where he have neglected the products μx_i^2 and μy_i^2, by considering these terms of third order, due to the smallness of μ. If we drop the constant terms, the transformed effective potential takes the following form

$$U = \sum_{i=1}^{2} \mu_i \left[\frac{3}{2}x_i^2 + \frac{\mu}{r_{2i}} + \frac{\mu_{3-i}}{2r} \right], \tag{2.7}$$

and the Jacobi constant

$$C = -\sum_{i=1}^{2} \mu_i \left[(\dot{x}_i^2 + \dot{y}_i^2) - 3x_i^2 - 2\frac{\mu}{r_{2i}} - \frac{\mu_{3-i}}{r} \right].$$

Thus, the Hamiltonian function in Hill's approximation, after introducing the conjugate momenta by means of equations (2.4), becomes

$$H = \sum_{i=1}^{2} \left[\frac{1}{2\mu_i}(p_{x_i}^2 + p_{y_i}^2) + y_i p_{x_i} - x_i p_{y_i} + \mu_i \left(\frac{1}{2}(y_i^2 - 2x_i^2) - \frac{\mu}{r_{2i}} \right) \right] - \frac{\mu_1 \mu_2}{r}.$$

Let us now perform a series of canonical transformations in order to give a more convenient form of the Hamiltonian function. To begin with, we scale the momenta by a factor μ_1,

$$p_{x_i} = \mu_1 \bar{p}_{x_i}, \quad p_{y_i} = \mu_1 \bar{p}_{y_i}, \quad i = 1, 2,$$

which gives rise to a canonical transformation with multiplier $\lambda = \mu_1^{-1}$. According to the theory of canonical transformations [MHO09], and suppressing the hats after transformation, we arrive to the new Hamiltonian

$$H = \frac{1}{2}(p_{x_1}^2 + p_{y_1}^2) + y_1 p_{x_1} - x_1 p_{y_1} + \frac{1}{2}(y_1^2 - 2x_1^2) - \frac{\mu}{r_{21}}$$
$$+ \frac{\mu_1}{2\mu_2}(p_{x_2}^2 + p_{y_2}^2) + y_2 p_{x_2} - x_2 p_{y_2} + \frac{\mu_2}{2\mu_1}(y_2^2 - 2x_2^2) - \frac{\mu \mu_2}{\mu_1 r_{22}} - \frac{\mu_2}{r}.$$

A new scale of variables is introduced by

$$x_i = \mu^{1/3}\hat{x}_i, \quad y_i = \mu^{1/3}\hat{y}_i, \quad p_{x_i} = \mu^{1/3}\hat{p}_{x_i}, \quad p_{y_i} = \mu^{1/3}\hat{p}_{y_i}, \quad i = 1, 2.$$

This is a canonical transformation with multiplier $\lambda = \mu^{-2/3}$, so that the transformed Hamiltonian takes the form

$$H = \frac{1}{2}(p_{x_1}^2 + p_{y_1}^2) + y_1 p_{x_1} - x_1 p_{y_1} + \frac{1}{2}(y_1^2 - 2x_1^2) - \frac{1}{r_{21}}$$
$$+ \frac{\mu_1}{2\mu_2}(p_{x_2}^2 + p_{y_2}^2) + y_2 p_{x_2} - x_2 p_{y_2} + \frac{\mu_2}{2\mu_1}(y_2^2 - 2x_2^2) - \frac{\mu_2}{\mu_1 r_{22}} - \frac{\mu_2}{\mu r}.$$

Finally, we set $\mu_1 = \mu_2 = \mu_p$, and we get the Hamiltonian function we will use for our capture model

$$H = \sum_{i=1}^{2} \left[\frac{1}{2}(p_{x_i}^2 + p_{y_i}^2) + y_i p_{x_i} - x_i p_{y_i} + \frac{1}{2}(y_i^2 - 2x_i^2) - \frac{1}{r_{2i}} \right] - \frac{\mu}{r}, \qquad (2.8)$$

where μ is in fact the mass ratio μ_p / μ.

2.2   Regularization of the $2+2$ Hill problem

As in the case of the restricted three-body problem in the Hill approximation, we have to consider the occurrence of singularities. For the case of the Hamiltonian system defined by (2.8), three different singularities can take place and they correspond to the three possible collisions (we exclude the case of a triple collision).

The two first possible collisions are those involving a minor body and the planet. As it will be explained later, this case will not be considered in the framework of the $2+2$ Hill problem. So, we are left with the singularity due to the collision of the two minor bodies. To overcome this situation we will perform a regularization in the same style we did in section 1.2.2. To this end, we will adopt the procedure described by Waldvogel [Wal72]. This procedure follows the same ideas of the classical Levi-Civita regularization scheme. To begin with, we introduce a complex set of variables to account for the positions and the momenta

$$\mathbf{X}_1 = x_1 + iy_1, \qquad \mathbf{X}_2 = x_2 + iy_2,$$
$$\mathbf{P}_1 = p_{x_1} + ip_{y_1}, \qquad \mathbf{P}_2 = p_{x_2} + ip_{y_2}. \tag{2.9}$$

Note that, with this notation,

$$|\mathbf{X}_1| = \sqrt{x_1^2 + y_1^2}, \quad |\mathbf{X}_2| = \sqrt{x_2^2 + y_2^2}.$$

Let us introduce two complex variables

$$\mathbf{z}_1 = u_1 + iv_1, \quad \mathbf{z}_2 = u_2 + iv_2, \tag{2.10}$$

playing the role of new positions, related to the old positions by means of

$$\mathbf{X}_1 = \mathbf{X}_1(\mathbf{z}_1, \mathbf{z}_2), \quad \mathbf{X}_2 = \mathbf{X}_2(\mathbf{z}_1, \mathbf{z}_2).$$

We choose the change of variables in such a way that

$$\mathbf{X}_1 = a(\mathbf{z}_1, \mathbf{z}_2)^2, \quad \mathbf{X}_2 = c(\mathbf{z}_1, \mathbf{z}_2)^2, \quad \mathbf{X}_2 - \mathbf{X}_1 = b(\mathbf{z}_1, \mathbf{z}_2)^2, \tag{2.11}$$

where the functions a, b and c are chosen to satisfy the relation

$$a^2 + b^2 = c^2.$$

Although a, b and c are complex functions and not integer numbers, we can view them as they as forming a Pythagorean triplet. There are different ways to obtain a Pythagorean triplet and, among them, Waldvogel chooses the classical one given

in Proposition 28 of Book X of Euclid's Elements [Euc96] (see also [Sha78]). In this way we choose, for the functions a, b and c, the expressions

$$a = \frac{\mathbf{z}_1^2 - \mathbf{z}_2^2}{2}, \quad b = \mathbf{z}_1\mathbf{z}_2, \quad c = \frac{\mathbf{z}_1^2 + \mathbf{z}_2^2}{2}, \tag{2.12}$$

and consequently

$$\mathbf{X}_1 = \frac{1}{4}(\mathbf{z}_1^2 - \mathbf{z}_2^2)^2, \quad \mathbf{X}_2 = \frac{1}{4}(\mathbf{z}_1^2 + \mathbf{z}_2^2)^2, \quad \mathbf{X}_2 - \mathbf{X}_1 = \mathbf{z}_1^2\mathbf{z}_2^2. \tag{2.13}$$

Taking into account (2.9) and (2.10) we have

$$x_1 = \tfrac{1}{4}(u_1^2 - u_2^2 + 2u_1v_1 - v_1^2 - 2u_2v_2 + v_2^2)(u_1^2 - u_2^2 - 2u_1v_1 - v_1^2 + 2u_2v_2 + v_2^2),$$

$$y_1 = (u_1v_1 - u_2v_2)(u_1^2 - u_2^2 - v_1^2 + v_2^2),$$

$$x_2 = \tfrac{1}{4}(u_1^2 + u_2^2 - 2u_1v_1 - v_1^2 - 2u_2v_2 - v_2^2)(u_1^2 + u_2^2 + 2u_1v_1 - v_1^2 + 2u_2v_2 - v_2^2),$$

$$y_2 = (u_1v_1 + u_2v_2)(u_1^2 + u_2^2 - v_1^2 - v_2^2).$$

And for the distance between the masses we have

$$R_1 = |\mathbf{X}_1| = \sqrt{x_1^2 + y_1^2} = \tfrac{1}{4}((u_1 - u_2)^2 + (v_1 - v_2)^2)((u_1 + u_2)^2 + (v_1 + v_2)^2),$$

$$R_2 = |\mathbf{X}_2| = \sqrt{x_2^2 + y_2^2} = \tfrac{1}{4}((u_1 + v_2)^2 + (u_2 - v_1)^2)((u_1 - v_2)^2 + (u_2 + v_1)^2),$$

$$R_0 = |\mathbf{X}_2 - \mathbf{X}_1| = \sqrt{(x_1 - x_2)^2 + (y_1 - y_2)^2} = (u_1^2 + v_1^2)(u_2^2 + v_2^2).$$

To complete the transformation, we introduce the new momenta

$$\mathbf{\Pi}_1 = \pi_{u_1} + i\pi_{v_1}, \quad \mathbf{\Pi}_2 = \pi_{u_2} + i\pi_{v_2},$$

in such a way that the transformation is canonical. We do that by means of the generating function

$$G = \sum_{k=1}^{2} \left(\pi_{u_k} u_k(x_1, x_2, y_1, y_2) + \pi_{v_k} v_k(x_1, x_2, y_1, y_2) \right), \tag{2.14}$$

and then

$$u_k = \frac{\partial G}{\partial \pi_{u_k}}, \quad v_k = \frac{\partial G}{\partial \pi_{v_k}}, \quad p_{x_k} = \frac{\partial G}{\partial x_k}, \quad p_{y_k} = \frac{\partial G}{\partial y_k}, \quad k = 1, 2. \tag{2.15}$$

It follows, from (2.14) and (2.15), that

$$p_{x_k} = \sum_{j=1}^{2} \left(\pi_{u_j} \frac{\partial u_j}{\partial x_k} + \pi_{v_j} \frac{\partial v_j}{\partial x_k} \right), \quad p_{y_k} = \sum_{j=1}^{2} \left(\pi_{u_j} \frac{\partial u_j}{\partial y_k} + \pi_{v_j} \frac{\partial v_j}{\partial y_k} \right), \quad k = 1, 2.$$

Taking into account that the change of variables is analytic, and by virtue of the equations of Cauchy-Riemann, we arrive at

$$\mathbf{P}_1 = \mathbf{\Pi}_1 \overline{\frac{\partial \mathbf{z}_1}{\partial \mathbf{X}_1}} + \mathbf{\Pi}_2 \overline{\frac{\partial \mathbf{z}_2}{\partial \mathbf{X}_1}}, \quad \mathbf{P}_2 = \mathbf{\Pi}_1 \overline{\frac{\partial \mathbf{z}_1}{\partial \mathbf{X}_2}} + \mathbf{\Pi}_2 \overline{\frac{\partial \mathbf{z}_2}{\partial \mathbf{X}_2}}, \tag{2.16}$$

where the bar means complex conjugation. Differentiating (2.13) respect to $\mathbf{X}_1$ we obtain

$$(\mathbf{z}_1^2 - \mathbf{z}_2^2)\left(\mathbf{z}_1\frac{\partial \mathbf{z}_1}{\partial \mathbf{X}_1} - \mathbf{z}_2\frac{\partial \mathbf{z}_2}{\partial \mathbf{X}_1}\right) = 1, \quad (\mathbf{z}_1^2 + \mathbf{z}_2^2)\left(\mathbf{z}_1\frac{\partial \mathbf{z}_1}{\partial \mathbf{X}_1} + \mathbf{z}_2\frac{\partial \mathbf{z}_2}{\partial \mathbf{X}_1}\right) = 0,$$

and the solution of the above linear system yields

$$\overline{\frac{\partial \mathbf{z}_1}{\partial \mathbf{X}_1}} = \frac{1}{2\bar{\mathbf{z}}_1(\bar{\mathbf{z}}_1^2 - \bar{\mathbf{z}}_2^2)}, \quad \overline{\frac{\partial \mathbf{z}_2}{\partial \mathbf{X}_1}} = -\frac{1}{2\bar{\mathbf{z}}_2(\bar{\mathbf{z}}_1^2 - \bar{\mathbf{z}}_2^2)}.$$

Analogously, for the derivatives respect to $\mathbf{X}_2$, we obtain

$$\overline{\frac{\partial \mathbf{z}_1}{\partial \mathbf{X}_2}} = \frac{1}{2\bar{\mathbf{z}}_1(\bar{\mathbf{z}}_1^2 + \bar{\mathbf{z}}_2^2)}, \quad \overline{\frac{\partial \mathbf{z}_2}{\partial \mathbf{X}_2}} = \frac{1}{2\bar{\mathbf{z}}_2(\bar{\mathbf{z}}_1^2 + \bar{\mathbf{z}}_2^2)}.$$

Finally, substitution in (2.16) results in

$$\mathbf{P}_1 = \frac{\mathbf{\Pi}_1\bar{\mathbf{z}}_2 - \mathbf{\Pi}_2\bar{\mathbf{z}}_1}{2\bar{\mathbf{z}}_1\bar{\mathbf{z}}_2(\bar{\mathbf{z}}_1^2 - \bar{\mathbf{z}}_2^2)}, \quad \mathbf{P}_2 = \frac{\mathbf{\Pi}_1\bar{\mathbf{z}}_2 + \mathbf{\Pi}_2\bar{\mathbf{z}}_1}{2\bar{\mathbf{z}}_1\bar{\mathbf{z}}_2(\bar{\mathbf{z}}_1^2 + \bar{\mathbf{z}}_2^2)}, \tag{2.17}$$

that completes, together with (2.13), the transformation from the old variables to the new ones.

To get the expression of the Hamiltonian in the new variables, we introduce the shorthands

$$Q_1 = |\mathbf{\Pi}_1\bar{\mathbf{z}}_2 - \mathbf{\Pi}_2\bar{\mathbf{z}}_1|^2, \quad Q_2 = |\mathbf{\Pi}_1\bar{\mathbf{z}}_2 + \mathbf{\Pi}_2\bar{\mathbf{z}}_1|^2, \tag{2.18}$$

and we also take into account that the distances are given by

$$R_0 = |\mathbf{z}_1\mathbf{z}_2|^2, \quad R_1 = \frac{1}{4}|\mathbf{z}_1^2 - \mathbf{z}_2^2|^2, \quad R_2 = \frac{1}{4}|\mathbf{z}_1^2 + \mathbf{z}_2^2|^2.$$

Then, the Hamiltonian can be written, in terms of a new variables, as

$$H = \frac{1}{32}\frac{Q_1}{R_0 R_1} + \frac{1}{32}\frac{Q_2}{R_0 R_2} + \frac{1}{4}\Im\left[\mathbf{z}_1\overline{\mathbf{\Pi}}_1 + \mathbf{z}_2\overline{\mathbf{\Pi}}_2\right] + \frac{1}{2}(R_1^2 + R_2^2)$$

$$- \frac{3}{32}\left(\Re[(\mathbf{z}_1^2 - \mathbf{z}_2^2)^2]\right)^2 - \frac{3}{32}\left(\Re[(\mathbf{z}_1^2 + \mathbf{z}_2^2)^2]\right)^2 - \frac{1}{R_1} - \frac{1}{R_2} - \frac{\mu}{R_0}, \tag{2.19}$$

where $\Re[\mathbf{z}]$ and $\Im[\mathbf{z}]$ stand for the real part and imaginary part of the complex variable $\mathbf{z}$.

To complete the regularization procedure, we introduce a new independent variable τ as

$$dt = R_0 R_1 R_2 d\tau$$

If we fix the value of the Hamiltonian to be E and perform an overall multiplication by $R_0 R_1 R_2$ we get the pseudoHamiltonian

$$K = R_0 R_1 R_2 (H - E) \tag{2.20}$$

which is free of singularities and it reads as

$$K = \frac{Q_1 R_2 + Q_2 R_1}{32} + \frac{R_0 R_1 R_2}{4} \left(\Im \left[\mathbf{z}_1 \overline{\mathbf{\Pi}}_1 + \mathbf{z}_2 \overline{\mathbf{\Pi}}_2 \right] + 2(R_1^2 + R_2^2) \right)$$

$$- \frac{3 R_0 R_1 R_2}{32} \left(\left(\Re[(\mathbf{z}_1^2 - \mathbf{z}_2^2)^2] \right)^2 + \left(\Re[(\mathbf{z}_1^2 + \mathbf{z}_2^2)^2] \right)^2 \right) \tag{2.21}$$

$$- R_0 R_1 - R_0 R_2 - \mu R_1 R_2 - E R_0 R_1 R_2.$$

Now, the canonical equations of motion can be written as follows

$$\frac{d\mathbf{z}_{jl}}{d\tau} = \frac{\partial K}{\partial \mathbf{\Pi}_{jl}}, \quad \frac{d\mathbf{\Pi}_{jl}}{d\tau} = -\frac{\partial K}{\partial \mathbf{z}_{jl}}, \tag{2.22}$$

where $j = 1, 2$ and $l = 1$ stands for the real part and $l = 2$ for the imaginary part.

2.3 Summary

As a summary of this chapter we list the main features of the model proposed. We consider a hierarchical restricted four-body problem with two primaries revolving in a circular orbit about their center of mass and two small bodies moving under their gravitational influence. The model results in the sum of two independent circular restricted three-body problems coupled by the interaction between the two small bodies. Being this term μ/r, where r stands for the distance between the minor bodies and μ the mass parameter, with a typical value less than 10^{-6}, it only matters if the two small masses are too close. Assuming that the minor bodies are temporally trapped by the small primary, Hill's approximation is considered, simplifying the model, but retaining the main characteristic of the full problem, as it is the sum of two Hill approximations of the restricted three body problem for each of the small masses, coupled by their mutual interaction. This final model has different singularities due to double or triple collisions. In this way, we consider the avoidance of collision between the small bodies, for computational purposes, by means of Waldvogel regularization in the planar case, that is to say, when all the objects move in the orbital plane of the primaries.

Chapter 3

Numerical simulations and results

The two previous chapters constitute the theoretical framework for the numerical simulations of the capture model. As it was explained, at the beginning of chapter 2, it is the interaction of two small bodies in the vicinity of the planet that is responsible of a possible capture. The question now is how to simulate this situation. To this end, we take advantage of the model proposed, i.e., the restricted $2 + 2$ body problem in its Hill approximation. As it is deduced from equation (2.8), this model can be viewed as two independent Hill problems coupled by the term μ/r, which only matters if the two bodies are close enough. This suggests to divide the simulation into two parts. The first part, based on the Hill approximation of the restricted three-body problem, is used to select the initial conditions of the two parents bodies of a potential capture. The second one, based on the Hill approximation of the restricted $2 + 2$ body problem, is used to account for the interaction of the two bodies, while in the Hill sphere of the planet.

3.1   Selection of the initial conditions

The selection of the initial conditions is based on Monte Carlo methods, described in Appendix A. This method has been extensively used to simulate similar problems to the one in touch. Hénon was the pioneer in this kind of simulations [Hén71a, Hén71b], considering the dynamical evolution of spherical stellar systems, whose ideas are still in use in million-body star cluster simulations [RMW+16]. Later on, Petit and Hénon focused on numerical model of planetary rings in which particles interact through gravitational and inelastic collisions [PH87a, PH87b]. Recently, Monte Carlo methods have been used to theoretical predict the presence of a nine planet in the most outer part of the solar system [dlFMdlFM16]. In our case, the basic idea is to get a large number of potential objects going into the Hill sphere from outside and that leave it after a minimum
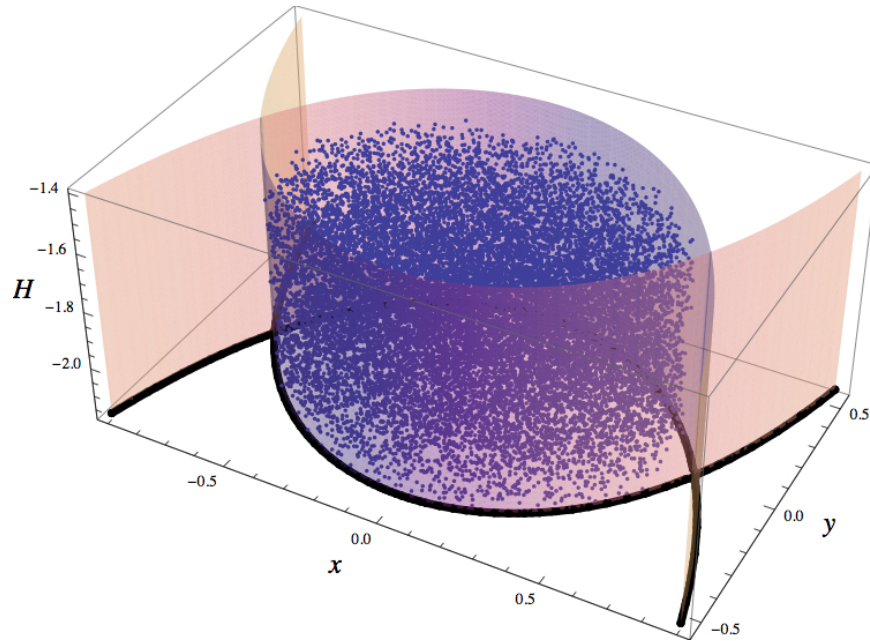
Figure 3.1: The starting set of initial conditions, selected at random inside the Hill sphere with a Hamiltonian value above the saddle point.

time around the planet. In this way, we choose randomly a value for the Hamiltonian (1.13) in the interval

$$\left(-\frac{3\sqrt[3]{3}}{2}, -1.3\right)$$

in order to guarantee that the object is a potential escape object. We note that the model we are using does not depend on the mass of the small body. Thus, it applies to every object, regardless its mass. Once the energy is selected, initial conditions are chosen at random inside the Hill sphere. In fact, we choose the coordinates and one of the momenta and the other one is fixed according to the value of the Hamiltonian. Doing this, we get a random collection of potential initial conditions, as it is depicted in Figure 3.1.

These initial conditions are transformed into regularized coordinates (1.22), and integrated numerically, by means of a linear multistep method of 12th order. The aim of this numerical integration is to find those initial conditions that give rise to orbits temporally trapped in the Hill sphere, but not permanently. We also impose that they are trapped a minimum time of 50 planet's periods in regularized time, which is longer than the real time. To this end, every initial condition is propagated forward in time. If it leaves the Hill sphere, in a time less than 5 000

planetary periods, it is integrated backward in time to see if it also leaves the Hill sphere. If this is the case, and the total time inside the Hill sphere is longer than 50 planetary periods and less than 10 000, the initial conditions, in cartesian variables, together with the energy and the distance to the planet, as well as the regularized lifetime, are recorded. We note that orbits passing through the planet are also considered, as the problem is treated in regularized coordinates, avoiding the singularity. At a first glance, these orbits should be discarded. However, these collision orbits are also possible candidates to exchange energy with other object, if the interaction is previous to the collision, and so they are not discarded. A typical record is as follows,

x	0.58720916388491650740
p_x	-0.24191109520516448916
y	-0.43197534153720662520
p_y	0.34756953833837311851
r	0.72898374319775405270
H	-1.63321956653858779700
lifetime	81.62839793791843590000

where the initial conditions are recorded at a distance $r = 0.729$, that is to say outside the Hill sphere, with a radius $r_H = 3^{-1/3} = 0.693361$. It can also be seen that the value of the Hamiltonian is greater than that corresponding to the saddle point $H_{r_H} = -2.16337$ and that the regularized lifetime is greater than 50, but less than 10 000.

It is worth noting that, from a departure set of 200 000 initial conditions, only 2054 are finally recorded, i.e., only 2054 objects satisfy the above requirements. In this way, the final set of initial conditions is that depicted in Figure 3.2, where the initial uniform distribution seems to be lost, as the points appear grouped around the saddles. This is because the initial positions are recorded at the moment the body enters the Hill sphere, and that is the reason why all of them are close to the saddle point, which is located in the middle of the escape gate of the Hill sphere, for a given value of the Hamiltonian. Also interesting is to look at the distribution of the value of the Hamiltonian function. From a more or less uniform distribution we arrive to another distribution with a clear peak just above the value of the Hamiltonian at the saddle point, as it can be seen in Figure 3.3. This is easily understood as a consequence of the escape dynamics. Indeed, the higher the value of the Hamiltonian function the more likely the object escapes the Hill sphere in a short time. As a consequence, the Hamiltonian H is not evenly distributed and there is an accumulation just above the value of the Hamiltonian at the saddle point. The mean value of this parameter is -1.825, which is 15% higher than the corresponding to the saddle point. However, the median is a little bit higher,
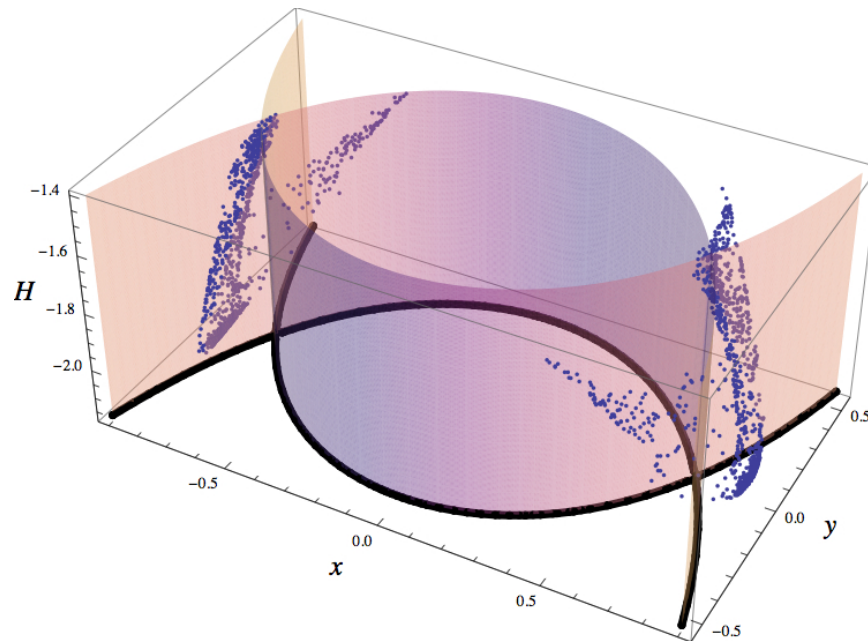
Figure 3.2: The final set of initial conditions, composed by temporally trapped orbits in the Hill sphere and selected from the departure set of initial conditions.

equal to -1.797 and it indicates that almost half of the initial conditions have a Hamiltonian value 20% greater than the corresponding value of the saddle point. However, the mean lifetimes for the selected objects, according to the energy, show a marked pick for those objects with a Hamiltonian value around -2 as it can be seen in Figure 3.3.

Regarding lifetime, although it is recorded as a regularized time, all of the orbits live a shorter period inside the Hill sphere. This is a consequence of the slow motion movie, that implies the time slows down when the two bodies are close. For instance, the regularized mean lifetime is 293.239, but there are some few orbits with very long lifetimes (as long as 9854 periods), and half of them lives less than 75 periods. If we take into account the real time counterpart, the numbers are always smaller. Now, the mean lifetime is 76.305 and the longest living orbit is inside the Hill sphere for 2641 periods, and half of the orbits lives less than 27 periods. This is summarized in Figure 3.4, where the orbits living more than 1000 periods are not considered, as they represent less than the 6% of the total. It is clearly seen that the majority of the orbits are inside the Hill sphere a moderate time. However, these times are, very likely, too long for a real situation in the solar system. It is known that Jupiter has temporally captured some comets in the recent past. For instance, comet 147P/Kushida-Muramatsu was captured in
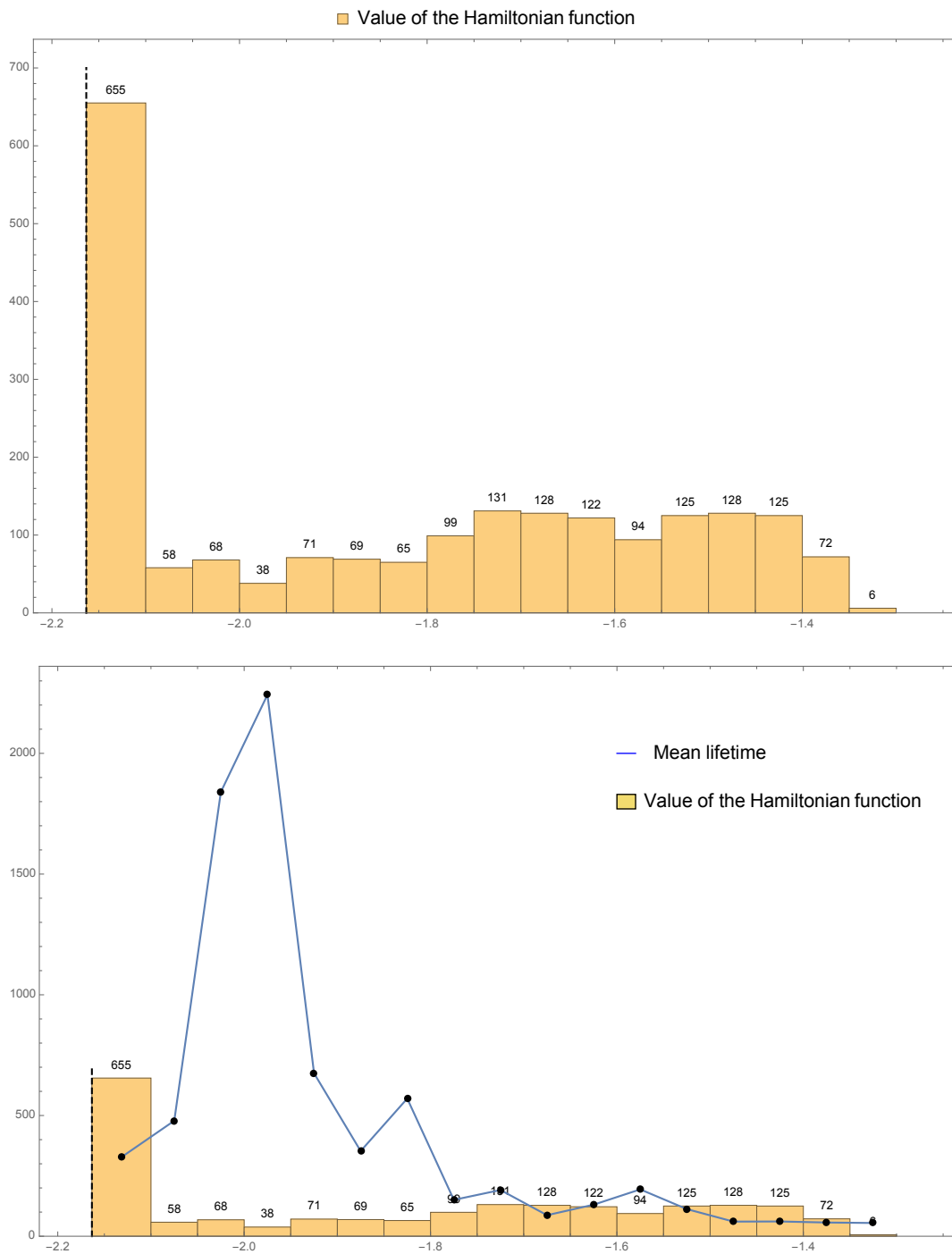
Figure 3.3: Distribution of the value of the Hamiltonian function for the set of selected initial conditions. The dashed line corresponds to the value of the Hamiltonian at the saddle point. In the bottom panel, superimposed, the mean lifetimes for the objects in each bar.

the mid of the last century for about 12 years, just one Jupiter's period [OIY$^+$08]. Nevertheless, the idea of our simulation is just to prove that the interaction of two bodies exchanging energy can lead to a permanent capture. For this reason, we consider a scenario where the probability of an interaction is high enough to be observed, and the lifetime is one of the parameters that increases this probability. In other case, may be millions of trials would be needed to observe a permanent capture, yielding a dramatic increase in the computation time.
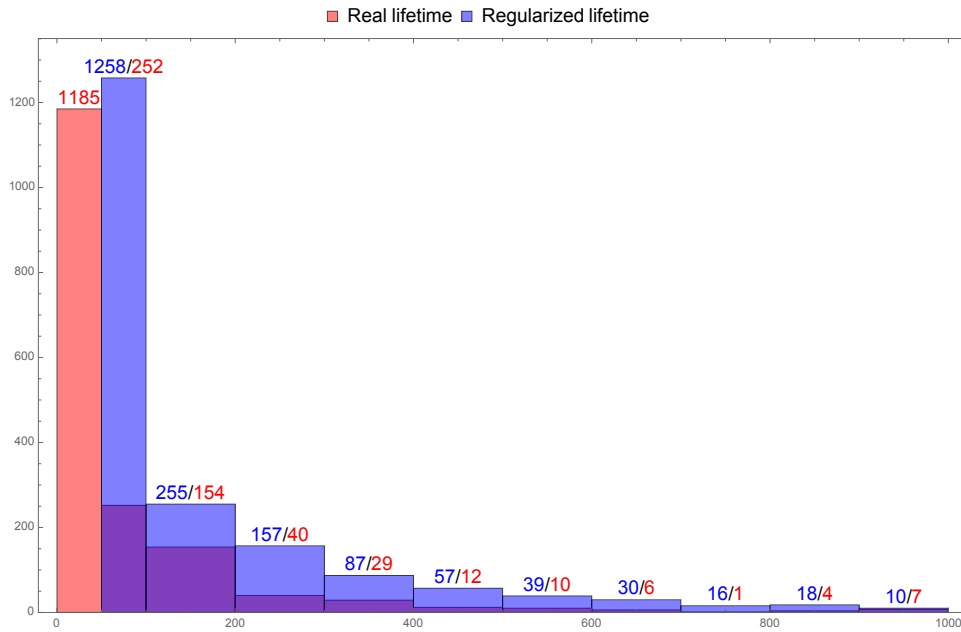

Figure 3.4: Lifetime of the initial set of potential captured objects in real and regularized time.

3.2   Capture simulation

Once the set of initial conditions has been selected, to search for a capture we use the following strategy: We choose two of the stored initial conditions as well as a mass ratio. Then, the cartesian coordinates of the two bodies are transformed into Waldvogel regularized coordinates (2.13) and (2.17) and the differential equations (2.22) are integrated numerically with the same method used in the previous section. The integration is carried out until one of the bodies has exited the Hill sphere and has departed sufficiently far, to be assumed it has escaped. At this point, we switch to cartesian coordinates and then to regularized Levi Civita co-

ordinates to continue the integration for the body that remains in the Hill sphere, using the differential equations (1.24). If this particle also exits the Hill sphere before 30 000 units of time, then no capture has occurred; otherwise, a capture is recorded. Besides, very close approaches to the primary are also considered and the integration is stopped if one of the small bodies is too close to the primary.

The strategy above described should be applied to every pair of the stored initial conditions. However, this amounts to more than two millions trials, yielding a very large computation time. Thus, instead of considering the whole set of pairs, we select a random sample of pairs of initial conditions, large enough to ensure we can catch the main features of the capture process, as capture rates, energy change or the type of captured orbits.

3.2.1 Capture rate

The interaction of two bodies inside the Hill sphere will not always gives rise a capture, but only in favorable cases. To measure the success rate, we consider the capture rate: the ratio between the number of effective capture trials and the total number of trials, as this number goes to infinity. It can be also viewed as the probability a given interaction ends in a capture. In this sense, every trial can be regarded as a Bernoulli one, with success probability p and failure probability $1 - p$, assuming a given trial is statistically independent of every other one. If the number of trials is n, we have the sum of n Bernouilli distributions, giving rise to a Binomial distribution $B(n, p)$. Moreover, if n is large, by means of the central limit theorem [Bil95], we can take as a reasonable approximation of $B(n, p)$ a normal distribution $N(np, \sqrt{np(1 - p)})$. Using this approximation, we can establish a confidence interval for the expected value of the capture rate. If the confidence is set to be 95%, the usual value, we obtain that the observed value of p, we denote by $\hat{p}$, will lie in the interval

$$\left[p - 1.96\sqrt{\frac{p(1 - p)}{n}}, p - 1.96\sqrt{\frac{p(1 - p)}{n}} \right], \tag{3.1}$$

with probability equal to 0.95. However, this interval is not always good enough, especially for small samples or if p is close to 0 or 1. A frequently cited rule of thumb [Bro01] is that the normal approximation is a reasonable one as long as $n \geq 30$, $np \geq 5$ and $n(1 - p) \geq 5$.

The confidence interval (3.1) shows that the larger the value of n the sharper the expected estimation is. But, on the other hand, the value of p is not known because we are using the sample to estimate it. Usually, in textbooks [Ros07], the value of p is replaced by $\hat{p}$ in (3.1), in such a way that the resulting interval is a confidence interval for the value of p at the 95% confidence level. However, if the

value of p is small, as we suppose to be in this case, this interval is not satisfactory, even if n is large [BCD01, Wal13]. This is a consequence of a frequent misunderstanding, that is assuming that the normal distribution of the errors in the true population is also normal in the observed one. An alternative confidence interval is preferable and we will consider the *Agresti-Coull* interval, as it is recommended in [BCD01]. In this sense, let be $X = n\hat{p}$ and

$$\tilde{X} = X + \frac{z_{\alpha/2}^2}{2}, \qquad \tilde{n} = n + z_{\alpha/2}^2,$$

being α the significance level[1] and $z_{\alpha/2}$ the value of a random variable in a $N(0,1)$ distribution such that $P(|z| > z_{\alpha/2}) = \alpha$. Let be now

$$\tilde{p} = \frac{\tilde{X}}{\tilde{n}},$$

then the Agresti-Coull confidence interval is given by

$$\left[\tilde{p} - z_{\alpha/2}\sqrt{\frac{\tilde{p}(1-\tilde{p})}{\tilde{n}}}, \tilde{p} + z_{\alpha/2}\sqrt{\frac{\tilde{p}(1-\tilde{p})}{\tilde{n}}} \right]. \qquad (3.2)$$

It is worth noting that the expression (3.2) is exactly the same than the expression for the classical interval, substituting $\hat{p}$ by $\tilde{p}$ and n by $\tilde{n}$.

As it was said previously, the accuracy in the estimation of the capture rate strongly depends on the number of trials performed, n. However, the numerical complexity of the interaction simulation yields a big amount of computation effort and we have to satisfy ourselves considering a large enough sample of trials, but not too much. In this sense, we have considered a sample of 50 000 pairs of objects, recording the estimation for the capture rate for different values of the mass parameter, following the Agresti-Coull confidence interval. For instance, for a mass ratio $\mu = 10^{-9}$, after 50 000 trials, we have observed 67 captures and the estimated probability is, with a 95% confidence level,

$$p = 0.00137831 \pm 0.000325183.$$

For other mass ratios, the results are summarized in Figure 3.5 and Table 3.1, where five different values of μ are considered. The main conclusion derived is that the probability of capture increases very fast as soon as the mass ratio is bigger than 10^{-7}, in the limit of the observed values for irregular satellites around the giant planets. The capture rate is specially high for a mass ratio $\mu = 10^{-5}$. However, this is not a real situation and the reason why this increment appears

---

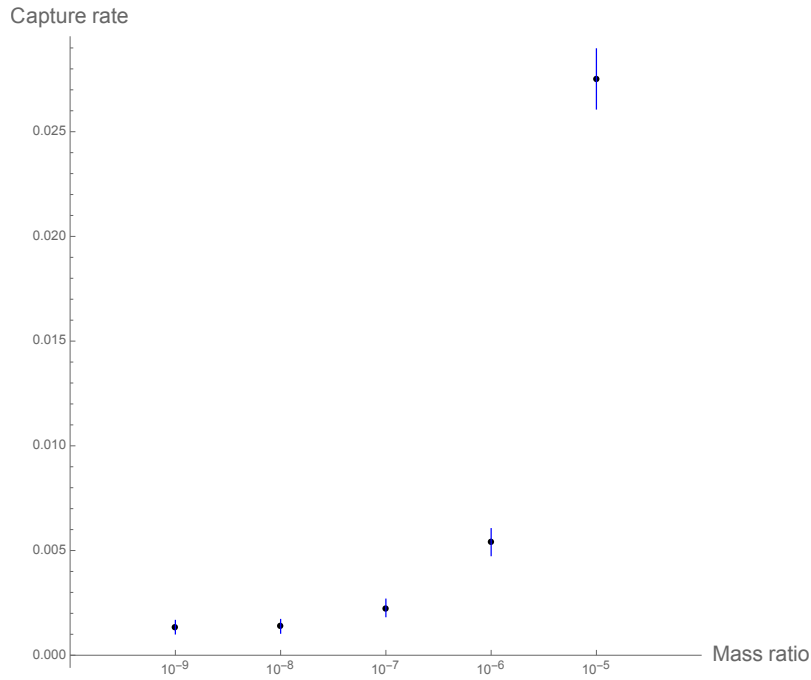[1]If the significance level is 5%, then $z_{\alpha/2} = 1.96$.

Figure 3.5: Capture rates for different mass ratios in the range $\mu = 10^{-9}$ and $\mu = 10^{-5}$.

is due to the contribution of the coupling term in the Hamiltonian function (2.8). In this sense, it is not necessary for a very close encounter to occur in order to modify the energy of the minor bodies. As a result, the number of capture objects increases.

3.2.2 Energy change

As it was said at the end of the previous section, one of the important questions in the capture mechanism is the variation of the energy of both the captured and escaping objects. At the beginning of the simulation, the value of the Hamiltonian of the $2 + 2$ problem is roughly equal to the sum of the values of the Hamiltonians of the restricted Hill three body problem for each of the interacting objects, provided the coupling term μ/r is negligible. On the other hand, at the end of the capture simulation, we also have the $2 + 2$ problem as a sum of two independent Hill problems and we can measure the energy change as the difference between the value of the Hamiltonian of the Hill problem[2] at the end and at the beginning of the simulation.

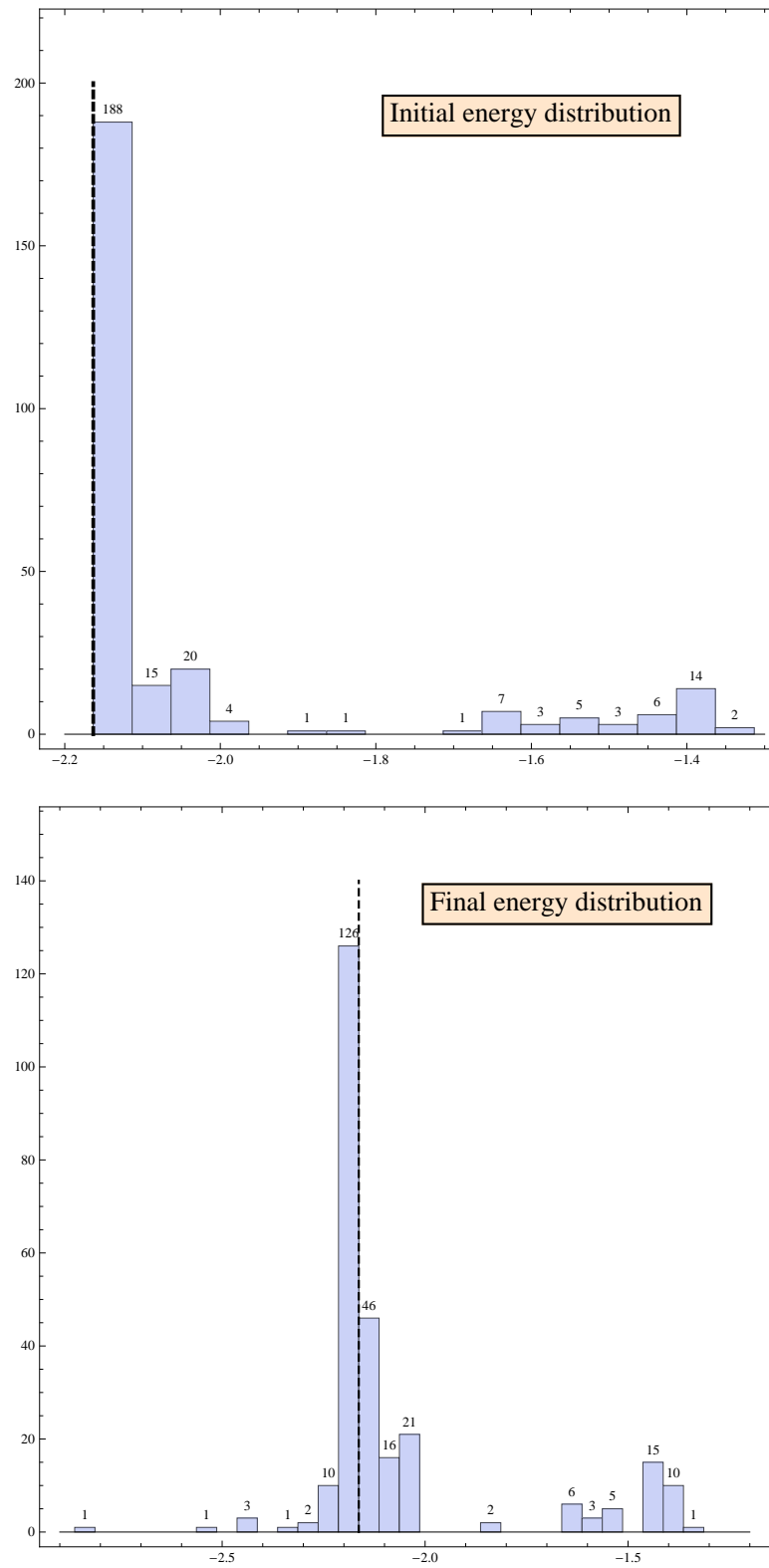
[2]From here on, we refers to this value as the energy.

Figure 3.6: Distribution of the energy at the initial and final states for the captured orbits when $\mu = 10^{-6}$. The dashed line corresponds to the energy at the saddle point in the Hill problem.

Mass ratio	Number of captures	Capture rate
10^{-9}	67	$0.00137831 \pm 0.000325183$
10^{-8}	69	$0.00141831 \pm 0.000329861$
10^{-7}	113	$0.00229824 \pm 0.000419713$
10^{-6}	270	$0.00543800 \pm 0.000644599$
10^{-5}	1376	$0.02755630 \pm 0.001434820$

Table 3.1: Capture rates for different mass ratios in the range $[10^{-9}, 10^{-5}]$ and the Agresti-Coull interval.

We have chosen to consider in detail the sample of captured objects corresponding to $\mu = 10^{-6}$, because it is large enough and, as a consequence, the statistics we are going to perform, more significant. In this case, we have observed 270 captured objects after $50\,000$ trials. The distribution of the energy at the initial state is depicted in the upper panel of Figure 3.6. The accumulation of objects with energy close to the saddle point is clearly apparent, as it was observed for the distribution of the whole set of initial conditions (see Figure 3.3). However, there is an important gap of energies in the interval $(-1.91, -1.66)$, where only three objects lie. This is an unexpected fact, because the gap was not present in the original distribution and it can suggest that the initial energy of the object conditions the probability of capture. Looking at the distribution of the energy at the end, once the object has been captured, we also make another interesting observation. This can be seen in lower panel of Figure 3.6, where the gap is still present. Even more, the most energetic objects at the final state, in the right side of the gap, come from the objects with the highest initial energies. Besides, a large number of objects have an energy below that of the saddle point, that is to say they are objects that cannot leave the Hill sphere. They are 144 objects, 53% of the total number of them. In other words, 53% of the objects have lost enough energy to be permanently captured. The rest are trapped in KAM islands and they can survive there for very long times or even forever.

The mean initial energy is found to be -2.0343, while the final one is equal to -2.06065. Thus, the mean energy is lower at the end, but still above the energy of the saddle point (-2.16337). However, this fact does not mean that the energy always diminishes. Indeed, we find some objects increase their energy in the capture process, as it is clearly seen from Figure 3.7, where the distribution of the increment of the energy is depicted. It is observed that most of the objects lose a small fraction of their energy and that around 40 objects increases their energy by a small amount. Nevertheless, there are objects that modify its energy significantly. The largest change corresponds to an object that loses around 30%
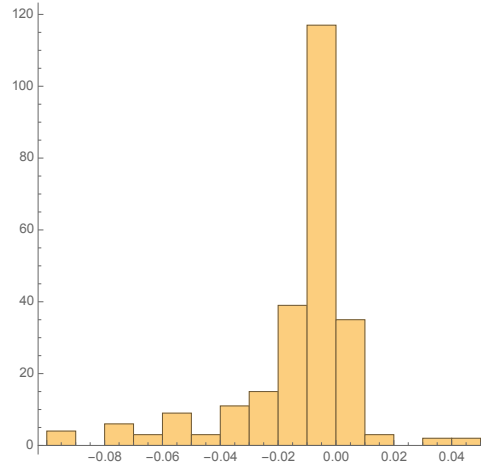
Figure 3.7: The increment of the energy after the capture process.

of its initial energy, going from $H = -2.16301$ to $H = -2.8211$. We can see how the change in energy takes place as a result of close encounters, as it is depicted in Figure 3.8, where in the upper panel the distance between the two objects is recorded, while in the lower panel it is the energy what it is represented. It is clear that when the distance between the two objects is small, there is a change in the energy and the objects modify their orbits. The variation of the energy can be the consequence of a unique close encounter or also of multiple encounters with small changes in the energy, in such a way that the orbits are slightly modify every time, before a definitive encounter produces the final orbits.

3.2.3   Type of captured orbits

The previous section served to highlight the mechanism of capture, that is to say the exchange of energy between the objects interacting. Even more, we observed how the common rule is that the final captured object loses energy, although there are exceptions. Besides, more than half of the captured objects lose enough energy to be permanently trapped inside the Hill sphere, as their final energy is lower than the energy of the saddle point. However, beyond these interesting observations, there remains an important issue as it is the type of orbit we find after the capture process. In this sense, we are interested in the fraction of prograde and retrograde orbits produced. Those orbits that do not belong to these categories will be regarded as *mixed* orbits, that is to say, orbits that revolve around the planet sometimes in direct motion and sometimes in retrograde one. Nevertheless, these orbits can be mainly prograde or retrograde, but we are not going to consider this
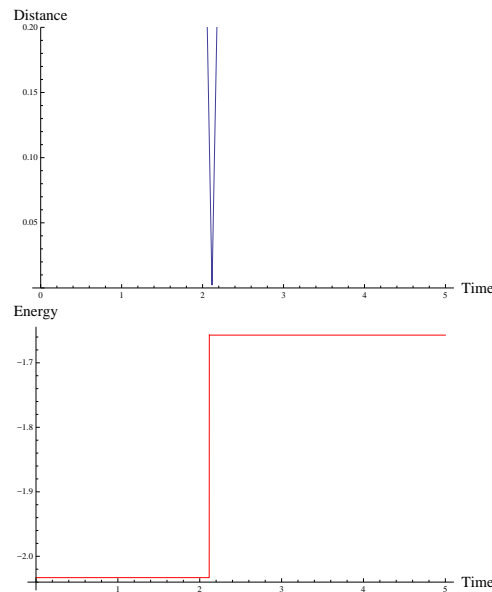
Figure 3.8: The modification of the energy as a consequence of a close encounter.

aspect in depth.

From the 270 of pairs, giving rise to a capture, we see that the number of different objects involved is not twice this number. In fact, some objects are present in several captured pairs, either contributing to the capture or as a trapped body. As a result, only 397 different objects interact and the type of orbit they follow is summarized in the left panel of Figure 3.9. The predominant type of orbit is the mixed one, representing almost 75% of the total. The prograde orbits represent almost 15% and the retrograde ones barely a 10%. After the interaction between the two objects, the type of captured orbits is given in the right panel of Figure 3.9. The mixed type is still the most frequent, 63%, but 12% less frequent than at the beginning. This decrement is, mainly, in favor of prograde orbits, that now represent 26% of the total. The retrograde orbits also increase in proportion, but as few as 1%. This distribution seems to be in opposition of the observed scenario, where most of the irregular satellites follow a retrograde orbit. However, this simplify model is a planar one and we can not expect a complete agreement with the real situation. Thus, we have to be cautious and satisfy ourselves with a statistics about the final type of obits and not to see the small proportion of retrograde orbits as a failure of the model.

For more details about this issue, in Table 3.2, we present the interaction between all the objects taking part in the capture process with the type of orbits before and after the capture. We can see that the most frequent interaction in-
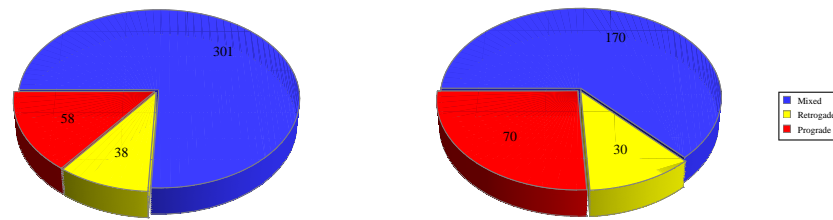
Figure 3.9: The type of orbit before the capture process (in the left) and after the capture process (in the right).

	Retrograde		Mixed		Prograde	
Retrograde	9	9 R 0 M 0 P	21	15 R 5 M 1 P	3	0 R 2 M 1 P
Mixed			160	3 R 120 M 37 P	65	0 R 39 M 26 P
Prograde					8	0 R 3 M 5 P

Table 3.2: Summary of the type of orbits involved in each interaction. In each square, the first number stands for the total number of interactions involving a concrete pair of orbits and the numbers in the right side represent the type of the captured orbit. The letters R, M and P refer to retrograde, mixed and prograde, respectively.

volves two mixed orbits, 59% of the total pairs. However, the result is not always a mixed one. Indeed, it can be appreciated that 23% of these interactions end in a prograde orbit and it is here where we find the increment in the number of prograde orbits. Nevertheless, it is also clear that, when a retrograde orbit is present in an interaction, the final orbit is most of the times retrograde, which roughly happens three of every four times. In the table, there are four missed pairs, corresponding to interactions with a collision object. In these cases, the final orbit results to be retrograde three of them and mixed the other one.

3.2.4   Some numerical examples

In this section we present some numerical examples to highlight some of the previous considerations. In this way, we provide a kind of atlas of different interactions where we account for fast and slow interactions, switching in the type of orbits or interaction with collision objects.

To begin with, we consider the interaction of two objects, one of them following a retrograde orbit and the other one a mixed orbit. If the final orbit is retrograde, the captured object is the one revolving initially in retrograde motion, with the exception of two cases, whose initial conditions are listed below

	O_1	O_2
x	0.64559937218167895430	0.70976617643856565465 0
p_x	$-$0.01395042340969841234	$-$0.19221969426321530720 0
y	0.19141594183214888369	0.02144197988805066068 5
p_y	$-$0.53831714118789530940	$-$0.38531490168169307831 0

	O_1	O_2
x	0.73077522712189801890	0.66849271046541214330 0
p_x	$-$0.10100432467929444660	$-$0.10752716423237032584 0
y	0.06977824037591601192	$-$0.00936097569070363719 2
p_y	$-$0.27563864681801214520	$-$0.58488129168788882680 0

In these two cases the object initially in a mixed orbit changes to a retrograde one. The situation is depicted in Figure 3.10, where the captured object is the one in mixed motion, although mostly retrograde. The upper panel corresponds to the first set of initial conditions and it is also an example of a fast interaction. The two objects interchange energy at the initial stages and one of them escapes very fast, while the other object modifies its orbit to a more or less regular orbit, but with energy above to that of the saddle point. It is also interesting to note that, in the example in the upper panel, the trapped object loses energy, while in the example of the lower one, corresponding to the second set of initial conditions, the trapped object increases its energy. Furthermore, at the beginning of the simulation process, in both cases the two objects are more or less at the same distance, but closer in the example in the lower panel, when the final exchange of energy takes place after different close encounters.

In the example above, we see how the time the two objects are interacting is variable. In this sense, the typical time the two objects are inside the Hill sphere before one of them escapes is about 90 planetary periods, although the median is about 60. These values are longer than the mean lifetime values of the initial sample. In this sense, we find that the longest interaction between two bodies

before the final capture is about 10 000 planetary periods. Moreover, this is an interesting case, because in the first stages one of the objects loses enough energy to be trapped into the Hill sphere. This situation holds for around 6000 periods, when a close encounter reverse the situation, and the trapped object with low energy is the other one. However, after 2000 more periods, the situation flips again and the body increasing its energy escapes definitively. This behavior is depicted in Figure 3.11 and the initial conditions for these two objects are the following

	O_1	O_2
x	-0.83513854992218916620	0.8305202363681372102
p_x	0.45838484246070954060	-0.4252326804018940476
y	-0.03826833437887983830	0.1141285712750616521
p_y	-0.72580368057833322130	0.6349106209507919818

Some times, the same object takes part in several capture processes with different results. In Figure 3.12 we present two interactions. In the first one (upper panel) the captured object is the same that escapes in the lower panel. Moreover, it is interesting to note how the interaction of the two objects, in the second case, takes place in several successive encounters, modifying the energy of the bodies in a slow fashion during a very long time. Also note that, in the first situation, the captured object loses enough energy to be permanently inside the Hill sphere, but in the second case there is an increment of the energy. Here we give the initial conditions for this example; the first set of initial conditions corresponds to the orbits in the upper panel of Figure 3.12, while the other set to the lower one.

	O_1	O_2
x	0.82903194445659067480	0.83652433974131934490
p_x	-0.41399644476762986760	-0.41375156662944506669
y	0.11813449868395373140	0.05960310396107033892
p_y	0.60043391449890848310	0.64800881180364999780

	O_1	O_2
x	0.82903194445659067480	$-0.83267740882229679400 0$
p_x	-0.41399644476762986760	$0.35584084823920703045 0$
y	0.11813449868395373140	$0.00464241237304412711 3$
p_y	0.60043391449890848310	$-0.53279114935031246510 0$

There exists also the possibility that two objects in a collision orbit with the primary interact before they collide, giving rise to a capture. This is an interesting situation as it can resemble the interaction of two comets, or the fragments of one

of them, in route to the planet. There are numerous observations of collisions of comets with Jupiter, the last one in March 2016. However, the most documented is the collision of comet Shoemaker-Levy 9 in July 1994. After its discovery in 1993, astronomers soon realized that it was orbiting Jupiter and it is thought it was captured from a solar orbit in the middle of the 1960s [Lan94]. Numerical tracking back of the orbit shows that it is likely it was a short-period comet with an aphelion close to Jupiter's orbit, and a perihelion interior to the asteroid belt [BM94]. Thus, collision orbits also matters in the capture process, as well as objects following a close path. This is exemplified in Figure 3.13 where, in the upper panel, two objects in collision orbits interact, resulting a captured object in retrograde motion, with a gain in energy. In the lower panel, only one of the objects follow a collision trajectory and the final trapped orbit is of mixed type, after a decrement of the initial energy. The initial conditions for these examples are the following

	O_1	O_2
x	0.69087448353671443430	0.70533058700642159430
p_x	-0.18794114211357135230	$-0.25568667158337976540 0$
y	-0.01470398149204942342	0.00188568014724673329 1
p_y	-0.47090312331193329150	$-0.39263483508555824253 0$

	O_1	O_2
x	0.81215421900379036750 00	0.73717351515301909881
p_x	$-0.45050999537801161840 00$	-0.25646704204387538170
y	$-0.00750965642364727001 27$	0.15318174208316748250
p_y	0.39171093823358682510 00	-0.15231959233862960024

Regarding objects that follow a close path, we can see in Figure 3.14 that a capture is also possible. The two objects follow a very close orbit during six periods, before they start to diverge in their trajectories. However, during this time they are interchanging energy in such a way that, at the end, one of the objects is trapped in a prograde orbit permanently, as its final energy is below that of the saddle point. It is worth noting that the final orbit of the trapped object differs too much from the initial one. The initial conditions for these objects are listed below

	O_1	O_2
x	0.83223318637832610630	0.83272290509813684520
p_x	-0.42770891634288343841	-0.41693471367544537864
y	0.07901525730959398086	0.07979190981918202197
p_y	0.60217241903475360320	0.59663137244206132520

It is interesting to see, for this example, how the capture process is modify with the mass ratio μ. Indeed, the final result is very sensitive to it, in such a way that sometimes the captured object is the other one, but also both of then can escape or collide. Moreover, if $\mu < 10^{-7}$ no capture takes place and the two objects escape. Similarly, if $\mu > 10^{-5}$ there is no capture, but now the two objects collide very fast. For $\mu \in [2 \times 10^{-7}, 5 \times 10^{-6}]$, we show in Figure 3.15 the results for 100 different simulations. A blue line indicates O_1 object is captured; a red one is for the capture of O_2 object; a yellow line stands for a mutual collision, while a green one for escape of the two bodies. As it can be seen, there is not a regular pattern and sometimes the final result is almost at random. A similar situation is observed for other objects that follow close trajectories.

Objects that do not follow a close path do not exhibit this complex behavior and, in general, they have a narrow window of mass ratio values ending into a capture. Outside this window, the two bodies escape. As an example, we consider the objects with initial conditions

	O_1	O_2
x	0.781767766254677698430	-0.811840060076070457700
p_x	-0.774242927752655907300	0.388451836263363048400
y	0.008885887238714064440	0.005992392475120278221
p_y	1.002887580661794508800	-0.328384074426652683400

If $8 \times 10^{-7} < \mu < 2 \times 10^{-6}$ the second object is captured, otherwise both of them exit the Hill sphere. This situation is depicted in Figure 3.16, where in the upper panel we have a capture for $\mu = 10^{-6}$, while for a greater mass ratio, $\mu = 1.5 \times 10^{-6}$, the lower panel shows the escape of the two bodies. It is worth noting how the coupling term affects the variation of the energy and, consequently, the final state of the two bodies, even if the mass ratio is slightly modified.

This scenario is similar for other objects, but with variations in the pattern, as it happens for the the bodies with initial conditions

	O_1	O_2
x	-0.813195828743553783550	-0.621064477761786476300
p_x	0.475275117179143891110	0.157541576010814698970
y	0.014857545874043982803	0.398567549936225784500
p_y	-0.443690027101813433400	-0.162112244511217223900

If $\mu \approx 10^{-6}$ the second object is captured. However, this body collide with the primary if the mass ratio is below this value. On the contrary, if $\mu \approx 1.16 \times 10^{-6}$ the two small masses collide and, above this value, if a capture takes place, it is

the first object that is captured. In Figure 3.17 the two captures and the collision with the primary are depicted. Note that the values of the mass ratio are very close between them and the final state is completely different. Even more, in the case $\mu = 1.64 \times 10^{-6}$ the final energy is below that of the saddle point, and the object can not leave the Hill sphere, being permanently trapped.

As we can see, this model yields a very rich casuistic in the capture process. However, the final orbits are, in general, very eccentric, although we cannot speak in a rigorous sense of a proper eccentricity, due to the irregular behavior of the orbits. Nevertheless, once the capture has occurred, we can define a pseudo-eccentricity by means of the equation

$$ e = \frac{D - d}{D + d}, $$

where D and d are the maximum and minimum distances to the primary, respectively, in a time interval corresponding to 10 periods of the planet. Due to the non regular motion of the trapped object, this eccentricity can vary, depending on the interval considered, but, for the sake of conciseness, we will take the same interval for all of the orbits, except for those with a very long interaction time. We observe that the mean value of the eccentricity is equal to 0.900277. However, the median, a more representative value in this case, is equal to 0.930694, while the first quartile is equal to 0.854279. This indicates that most of the orbits get too close to the primary. The upper panel of Figure 3.18 shows the distribution of the eccentricities for the captured orbits. The lowest eccentricity observed in our simulation is 0.415 and corresponds to a prograde orbit with very low energy, equal to -2.82111, well below that of the saddle point. The orbit is depicted in lower panel of Figure 3.18, and comes from two objects with initial conditions

	O_1	O_2
x	-0.68978070575289796020	0.83512378695144173780
p_x	0.09031935421541271991	-0.41439305812614879443
y	-0.02853686130135112825	0.07963046923057529036
p_y	0.48953706368281119100	0.63956041988580758510

3.3   Main results of the simulation

The main conclusion we extract from the numerical simulation is that the model proposed is able to account for the capture process. The mechanism is simple and it relies on the interchange of energy between the small objects when encounters take place. Also, a large variety of interactions can happen, making the scenario very interesting, because we cannot discard any initial situation. All of them are

suitable for a potential capture. This is, for instance, the case of two objects, may be coming from the disruption of a parent body, following a close path.

In general, the captured object loses energy, but we have shown examples where this is not the case, and objects increasing its energy are finally trapped.

In the capture process, the mass ratio plays an important role. On the one hand, the capture rate increases with the mass ratio, as it was expected. On the other hand, some pairs are very sensitive to the mass ratio and the final state of the interaction is very hard to predict.

Although the mechanism is satisfactory in some aspects, there are some other aspects that deserve more insight, as it is the lack of retrograde orbits and the high eccentricities of the final orbits. This suggests that other factors must be taken into account, as it can be the presence of drag or the influence of large regular moons around the planet.
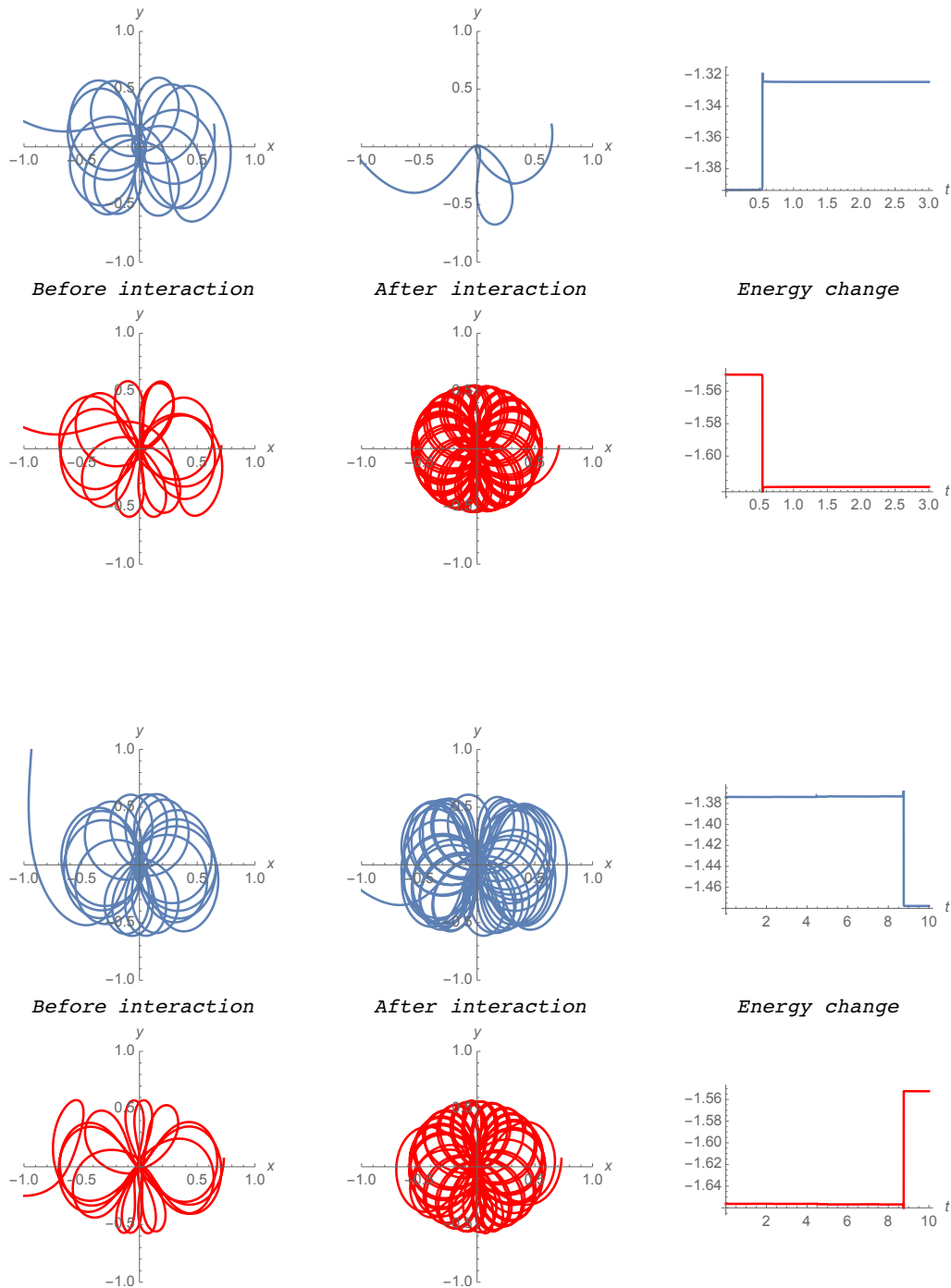
Figure 3.10: Example of interaction between an object in retrograde orbit and other one in a mixed one (almost retrograde) with a final retrograde orbit, coming from the mixed one. In the upper panel a fast interaction takes place and the trapped object looses energy. The lower panel shows a middle time interaction where the trapped object increases its energy.
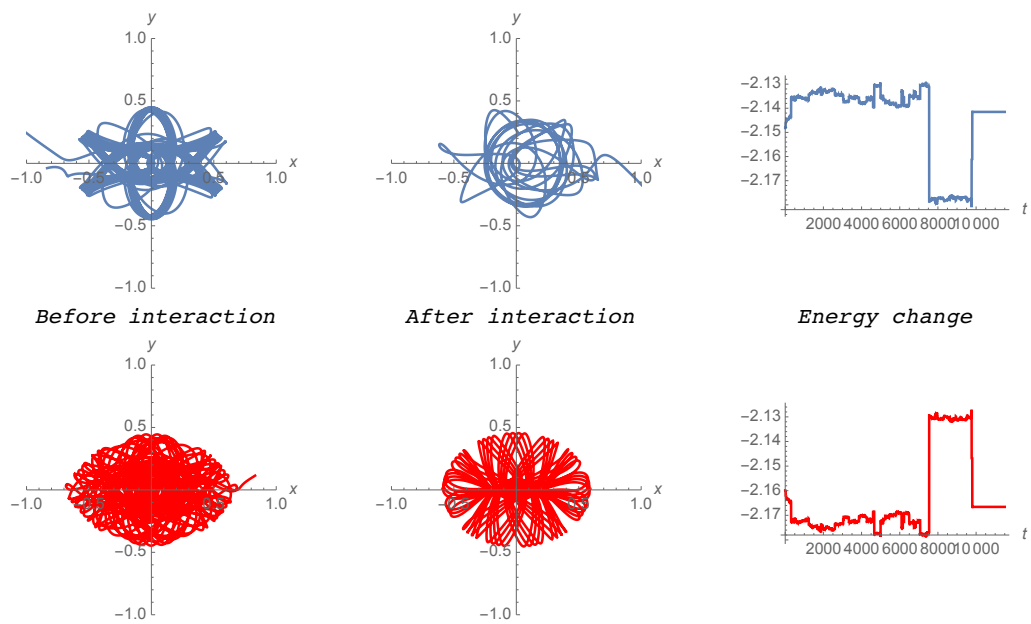
Figure 3.11: Example of a very long interaction between two objects with a lifetime in the Hill sphere of about 10 000 planetary periods. During the interaction two major energy changes occur.
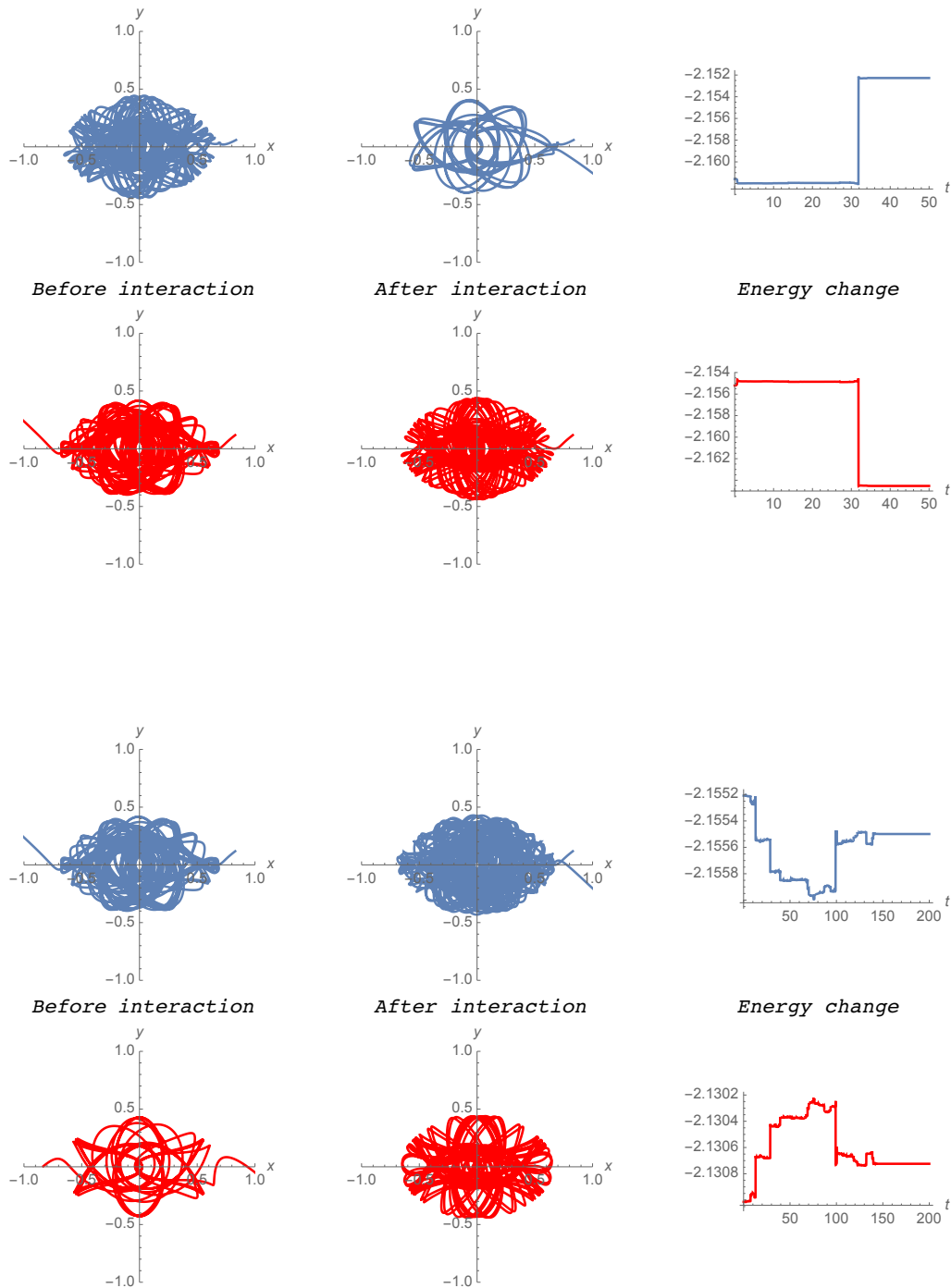
Figure 3.12: Interaction of an object in two different scenarios. In the upper panel the object following the mixed red orbit is captured, while in the lower one (in blue) it escapes, while the other object is trapped.
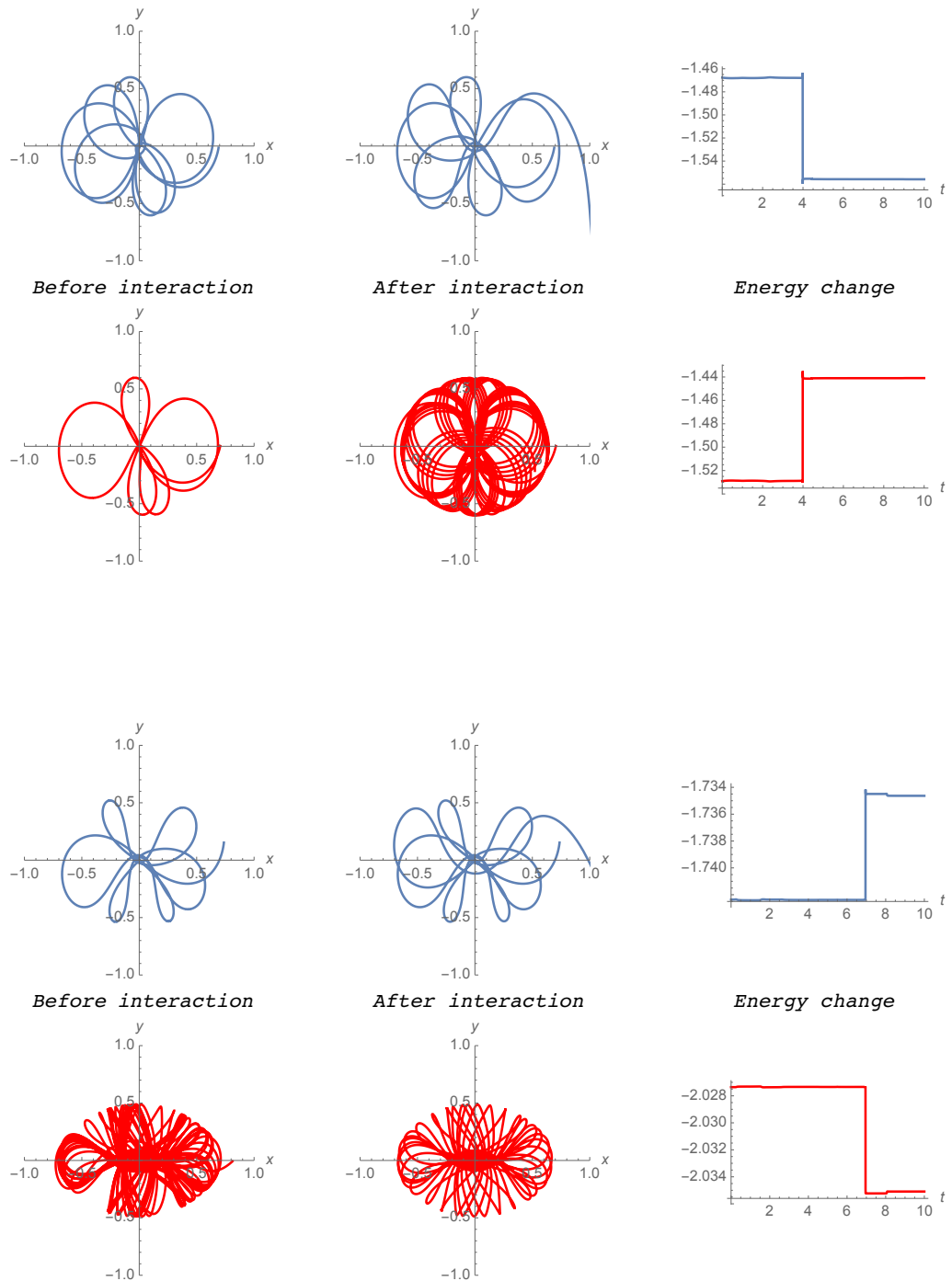
Figure 3.13: In the upper panel the interaction of two objects in collision orbits. In the lower panel the interaction of an object in a collision orbit (in blue) with a temporally trapped object in mixed orbit.
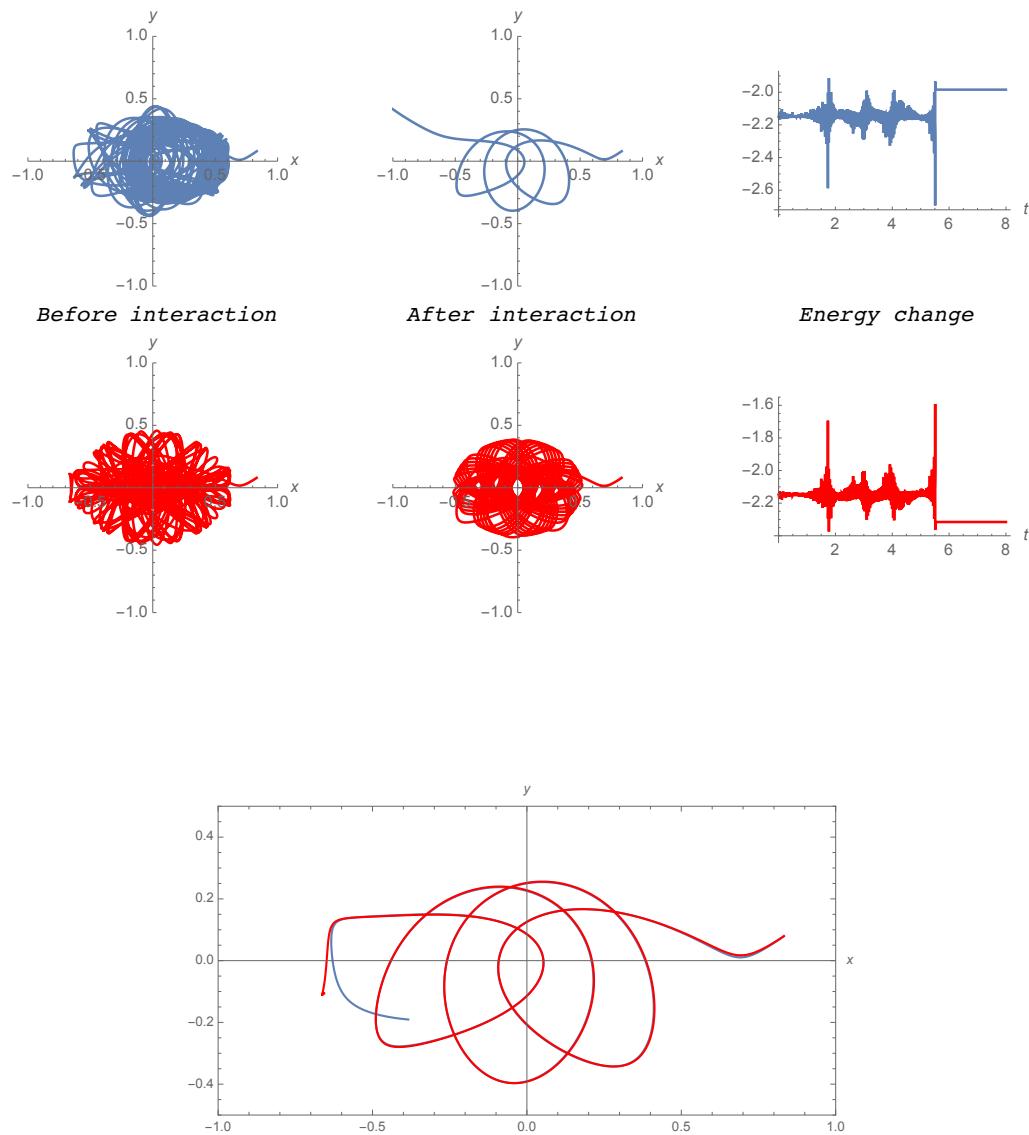
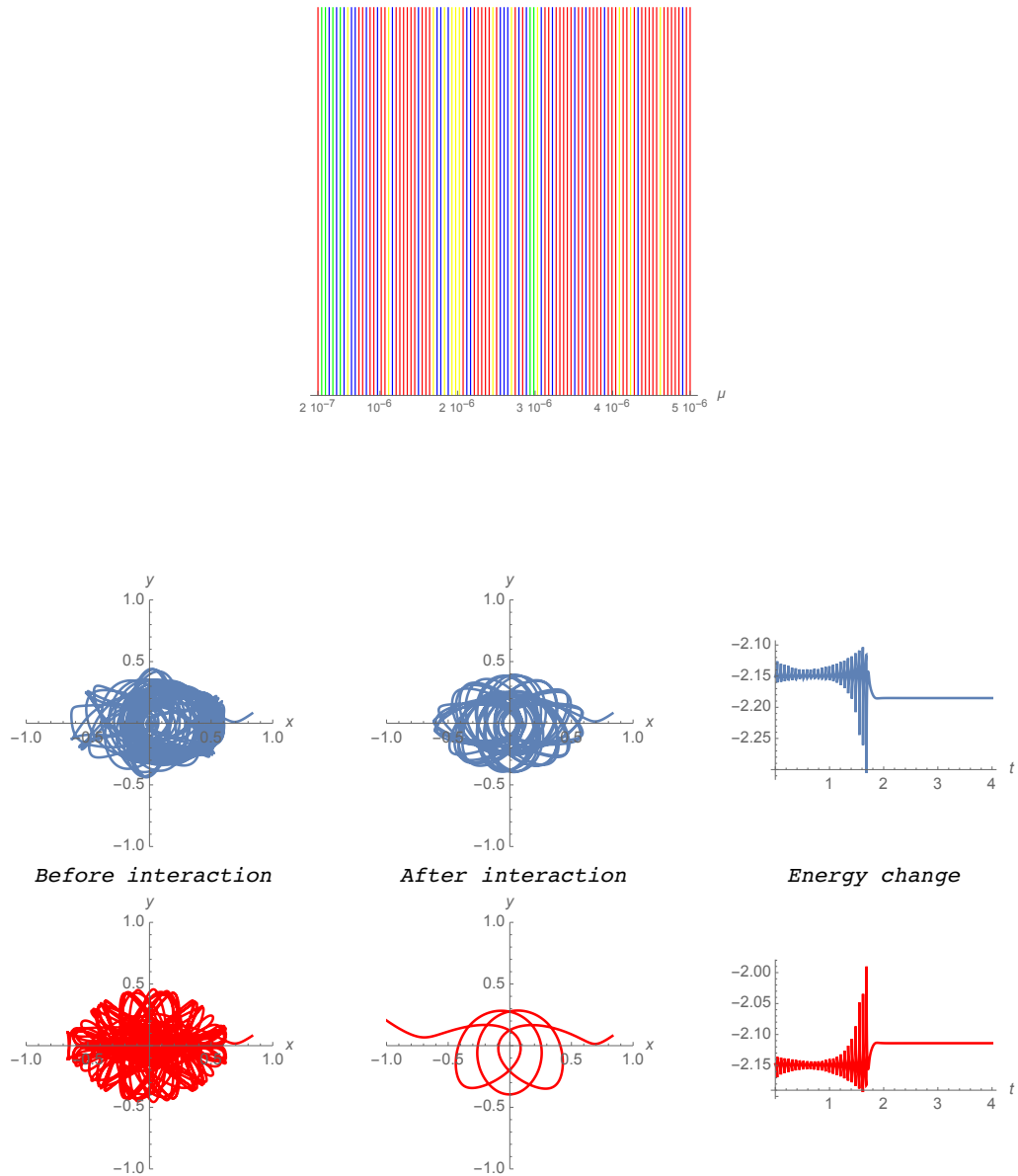Figure 3.14: The interaction of two objects following almost the same path.

Figure 3.15: The result of the interaction of two close objects as a function of the mass ratio μ. In the upper panel, blue color stands for the capture of the first object and red one for the capture of the second one. Green color indicates escape of the two objects and yellow one, mutual collision. In the lower panel the same objects as in Figure 3.14, but $\mu = 5 \times 10^{-7}$. The object captured is the other one.
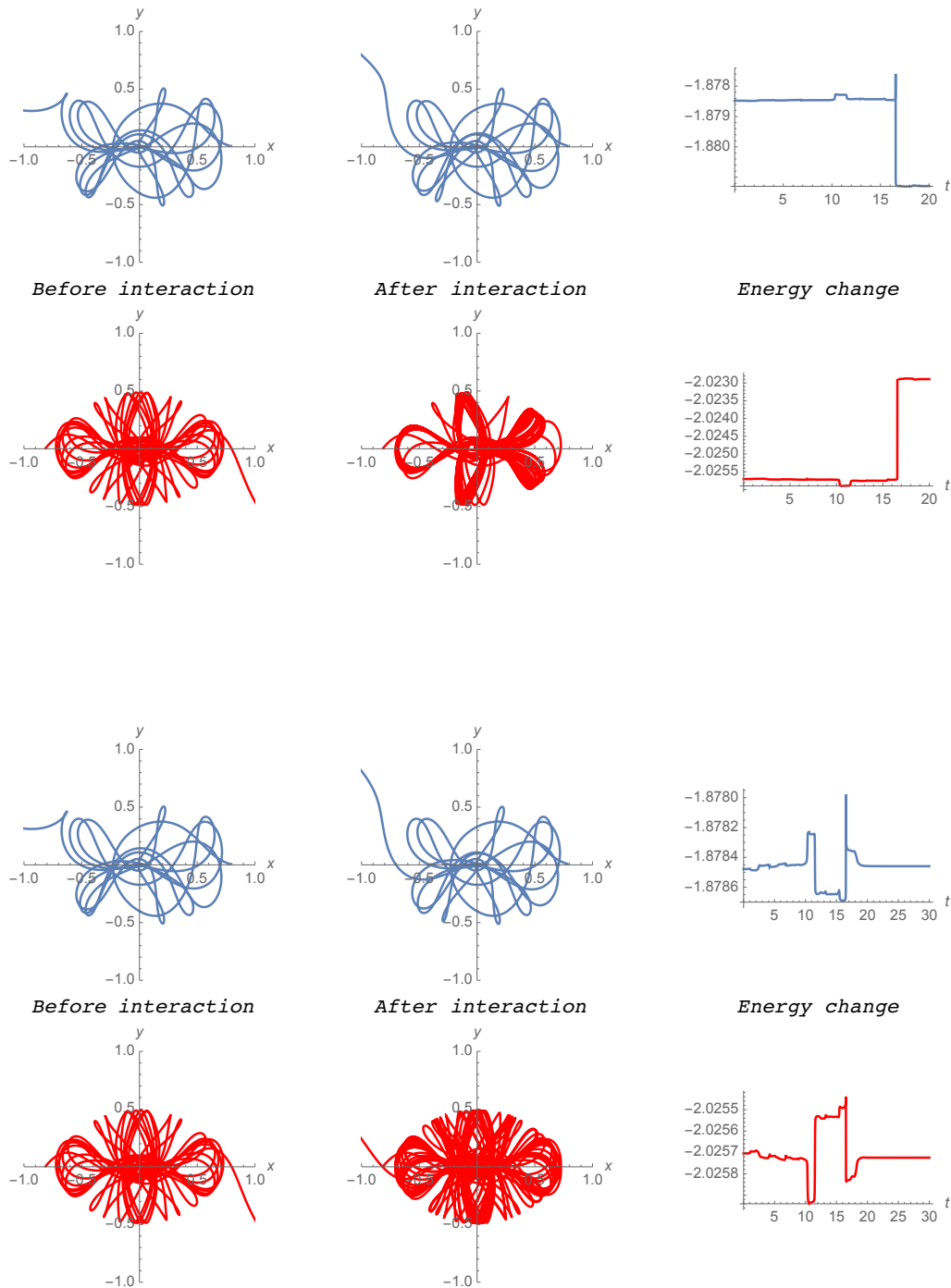
Figure 3.16: The interaction of two bodies for close values of the mass ratio. In the upper panel, for $\mu = 10^{-6}$, the first object is captured. In the lower panel, for $\mu = 1.5 \times 10^{-6}$, the two objects escape.
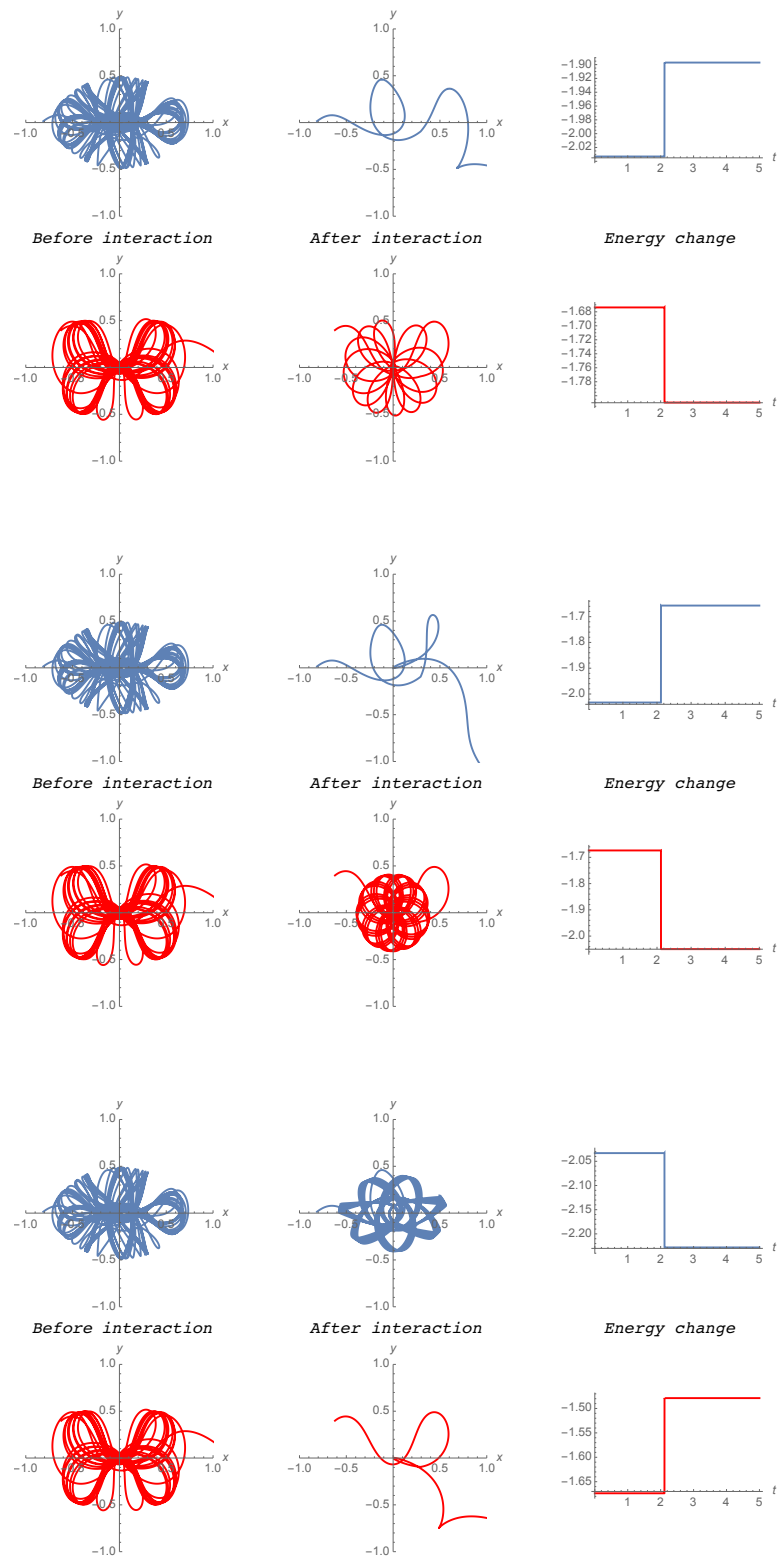
Figure 3.17: Three different final states for close values of μ. In the upper panel, for $\mu = 8 \times 10^{-7}$ one of the objects escape, while the other collides with the primary. In the middle, for $\mu = 10^{-6}$, the second object is trapped. In the lower panel it is the first object the captured one, for $\mu = 1.64 \times 10^{-6}$.
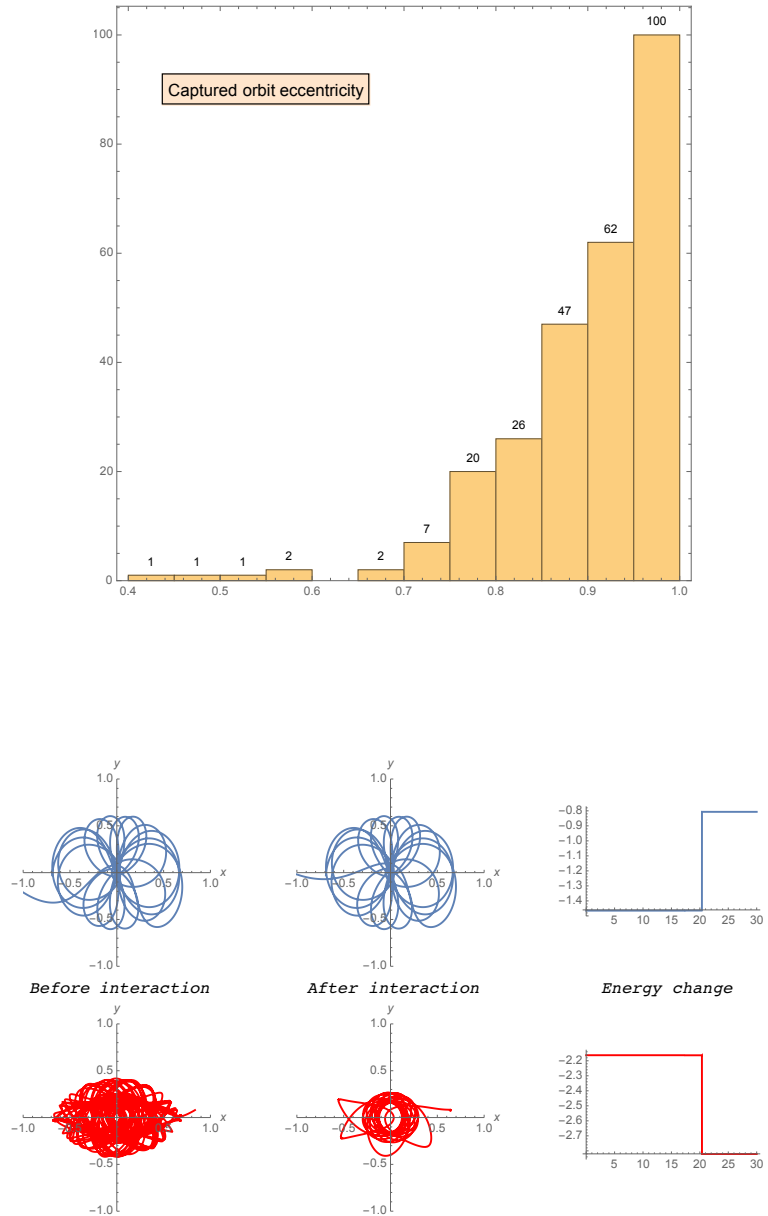
Figure 3.18: Distribution of the eccentricity of the captured orbits (upper panel). The lowest eccentric object captured. The mean eccentricity is equal to 0.415 and corresponds to an object in prograde motion (lower panel).

Chapter 4

Statistical study of the Kuiper belt objects

The study of the populations of astronomical objects is one of the topics in modern and classical astrophysics. The information derived from statistical aspects of the population helps to select the plausible dynamical models that give rise to the actual distribution of the observed population. In this sense, the construction of a dynamical model for a given population starts with a statistical analysis of the relevant data. What is the relevant data is also an interesting question, because there are multiple observed parameters that serve to characterize the population and one have to select those that give as much information as possible for the desired objective. Another relevant question is related to the biases of observational data. In fact, the data is not an unbiased sample of the total population as there are limitations imposed by the observational techniques and by some other constraints. These facts must be taken into account in order to perform a statistical analysis free of biases.

The population analyzed here is that corresponding to the objects in the Kuiper-Edgeworth belt, located beyond the orbit of Neptune. They are usually designed as KBO (Kuiper Belt Objects), and there are more than a thousand known KBOs. Our interest in this population is because it is thought that the irregular satellites could have been captured from some source regions in the Kuiper belt [JH07, NCS$^+$08]. Following the *Nice model* [TGML05], interactions with the migrating planets cleared objects from the young Kuiper belt, giving rise to the possibility of captures [MLTG05, TGML05]. Nevertheless, the source regions for the irregular satellites remain unknown and can be roughly divided into two possible regions: local and nonlocal. Local regions include those objects moving in a neighborhood of the growing giant planets, no ejected or absorbed by collisions. But, for capture processes, the nonlocal regions are the most interesting ones, as they sup-

ply the objects that enter into the Hill sphere where the capture mechanisms take place. In this way, it is suggested that the Trojan asteroids of Jupiter could be captured objects from the Kuiper belt in a late stage of the Solar system formation [MLTG05]. Even more, it is also thought that Triton could enter the Neptune's Hill sphere from a source region in the Kuiper belt and tidal dissipation further converted the temporarily captured retrograde orbit into a permanent stable one [ML95].

The physical parameters for KBOs are compiled in a database by the Minor Planet Center (responsible for the collection, computation, checking and dissemination of astrometric observations and orbits for minor planets, comets, and natural satellites) and can be obtained from its website [mpca]. For each object 15 different fields are provided. Among them, we find its designation and the facts of its discovery. The rest of the fields, a total of 11, refers to physical parameters, as they are the orbital elements and the absolute magnitude. For our statistical study we will consider those parameters that provide as much information as possible of the dynamical features of KBO population. These parameters are basically the semi major axis of the orbit (a), the eccentricity (e) and the inclination of the orbital plane (i), which proved to be the most relevant in the study of the main belt asteroid population. Nevertheless, we will also take into account the argument of the periapsis (ω), the absolute magnitude (H) and the number of observed oppositions (n).

4.1   Dynamic groups

It was speculated for a long time that the outermost part of the solar system was populated by small icy primordial particles – the residuals of the protoplanetary solar nebula. Based on theoretical considerations, Edgeworth and Kuiper, in the fifties of the last century, gave consistent arguments for this and conjectured the existence of a belt of objects between 40 and 50 AU that could be the origin of short period comets [Edg49, Kui51b]. This idea was strongly supported by other theoretical studies based on the frequency and on the total number of observed short period comets [Fer80]. Even more, an estimation of the number of objects, the total mass, the size of the objects and the characteristics of the orbits were inferred. Based on this, Fernandez [Fer80] established the magnitude of one of the largest hypothetical objects and concluded that, although detectable, it would be a very difficult task to observe it.

On the other hand, the study of the anomalous orbit of Pluto caused other authors to speculate about the existence of such region of bodies, beyond Neptune [Mal95]. An important role played the assumption of the migration of giant plan-

ets, especially Neptune, trapping Pluto's orbit in a 3:2 mean motion resonance[1]. The migration of planets is nowadays a central issue of the *Nice model*, one of the most plausible scenarios of the formation of the solar system [TGML05], which also predicts the existence of a belt of planetsimals beyond Neptune's orbit.

The theoretical considerations were the prelude to the first discovered object, aside from Pluto, in the *Kuiper belt*, by D. Jewitt and J. Luu [JL93]. This object, named 1992 QB1, fitted all the theoretical considerations of an expected KBO, that is, almost circular orbit with low inclination and at a mean distance of 43.734 AU. However, the next discovery showed a very different situation. It was the object 15789 (1993 SC) [WFOM95], that follows a similar orbit to that of Pluto, that is to say in 3:2 mean motion resonance with Neptune, with high inclination and eccentricity. Since then, much effort has been made to the search of trans Neptunian bodies through different specific surveys [EKC+05, PKG+11] and the dedication of the Hubble Space Telescope [CLSD95, BAB+03]. Nowadays more than a thousand trans Neptunian objects are known. At the beginning a trans Neptunian object (TNO) was the same as a Kuiper belt object (KBO), but the increasing number of them showed soon that their orbits exhibit different behaviors. This easily follows from a very basic statistical study.

Let us start with the distribution of the number of objects according to their semi major axis a, that is their mean distance to the Sun. The corresponding histogram is plotted in Figure 4.1. In this Figure, only objects with semi major axis in the interval [34,50] are considered, excluding a few of them with large semimajor axis, and they correspond to the objects listed in the database of the Minor Planet Center classified as trans Neptunian in January 2015. It can be seen, that the majority of the objects accumulates at distances between 39 and 48 AU. These limits are close to the mean motion resonances 3:2 and 2:1. There is a large population of objects trapped in the 3:2 mean motion resonance followed by a gap. Then, the objects are almost normally distributed up to the 2:1 mean motion resonance, where we observe again a lack of objects. Taking into account this distribution, a common belief is that the Kuiper belt is the part of the Solar System delimited by the two dashed lines in the Figure 4.1, in the band of the 3:2 and 2:1 mean motion resonance with Neptune [SCC01]. However, the structure of the outer Solar System is more intricate, and that can be proved if we take into account other relevant orbital elements, as they are the inclination and the eccentricity.

Before doing that, the information provided by Figure 4.1 gives a very interesting insight about the dynamical history of the trans Neptunian objects. The

---

[1] We say that two objects are in mean motion resonance when the ratio of their orbital periods is a rational number and, the most important ones, are those represented by the quotient of two small integers. For instance, Neptune and Pluto satisfy a 3:2 resonance, that means Neptune completes three orbits around the sun in the time it takes Pluto to complete just two.
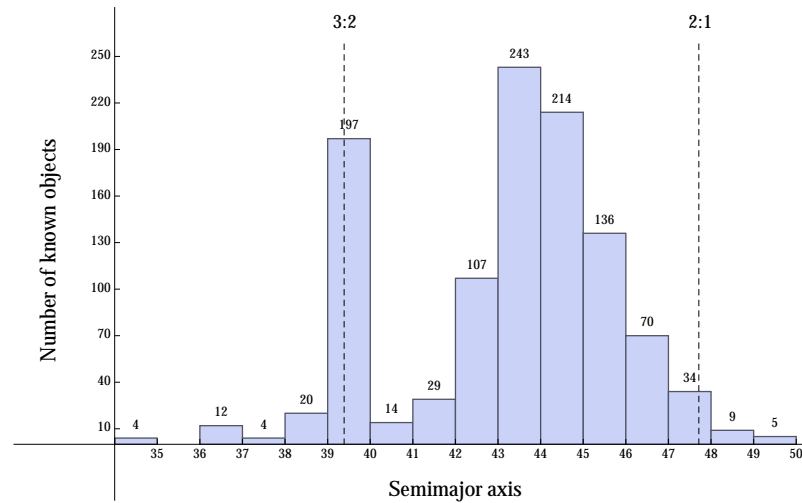
Figure 4.1: Distribution of the number of trans-Neptunian objects, according to the semi major axis. Dashed lines stand for a mean motion resonance 3:2 and 2:1 with Neptune.

first important thing is the gap $40 \leq a < 43$ AU, just after the 3:2 mean motion resonance. In [JWM05], it is explained that objects in this area would had had close encounters with Neptune and were scattered to the outer Solar System. However, objects trapped in the 3:2 mean motion resonance would had evolved into stable orbits avoiding close encounters with Neptune thanks to the resonance. On the other hand, if $a > 43$ AU, objects in the classical Kuiper belt, with low inclinations and moderate eccentricities, could not have had close encounters with Neptune and remained in stable orbits. This is a plausible explanation for the observed distribution and it is supported by different numerical simulations [JWM05, DLB95, MDL00].

Now, let us take a look at the dispersion diagram of semi major axis and eccentricity, depicted in Figure 4.2. Here, it is clear the population of objects in the 3:2 mean motion resonance with moderate and high eccentricities. Besides, it is also appreciated that objects in the populated region between $43 < a < 48$ exhibit a great range of eccentricities and part of them goes into the inner region of Neptune's orbit. These objects are potentially affected by close encounters and can be scattered, in such a way that their dynamical history is completely different to those objects with low eccentricities. Moreover, most Neptune crossers seems to be trapped in mean motion resonances with Neptune. Another interesting feature observed in Figure 4.2 is the gap after $a = 47.5$ AU. The population decreases in the number of objects towards the location of the 2:1 resonance, but it is not recovered for greater distances. This is an unexpected behavior that deserves further
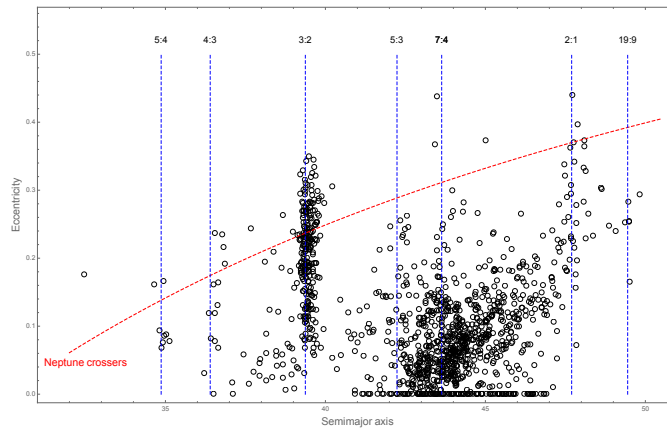
Figure 4.2: A plot of eccentricity against semi-major axis for observed Kuiper belt objects between 32 and 50 AU. Objects above the dashed red line are Neptune crossers. Also, the main mean motion resonances with Neptune are highlighted by blue dashed lines.

investigation.

The discussion above can be complemented by the dispersion diagram of the semimajor axis and the inclination, depicted in Figure 4.3. The presence of objects in high inclined orbits is a signal of different dynamical behavior among the objects in the Kuiper belt. In this case, we observe, not only the groups trapped in mean motion resonances, but a numerous population of objects, in the range from 42 to 48 AU, with low or moderate inclination. Based on this observations, the objects in the Kuiper belt, in a first attempt, can be roughly classified as resonant or non resonant and the last ones into different groups according to their eccentricity and inclination. However, even this simply classification is not an easy task. In fact, the first thing we have to solve is to decide when an object can be said that is trapped in a mean motion resonance with Neptune. In this way, the issue of stability plays an important role in the nature of the different populations, and this fact has to be taken into account, as it is done for the classification of small comets [Lev96]. In this way, following Gladman et *al*. [GMV08], the classification of a TNO must be based upon its current short-term dynamics rather than upon its long-term history and future evolution. Based on this idea and, by a balance of different points of view and taking into account that stability must be a criterion, a classification scheme has been proposed [GMV08]. It is a process of elimination based on the comparison of the current observed orbital elements of an object and its orbital elements after ten million years.
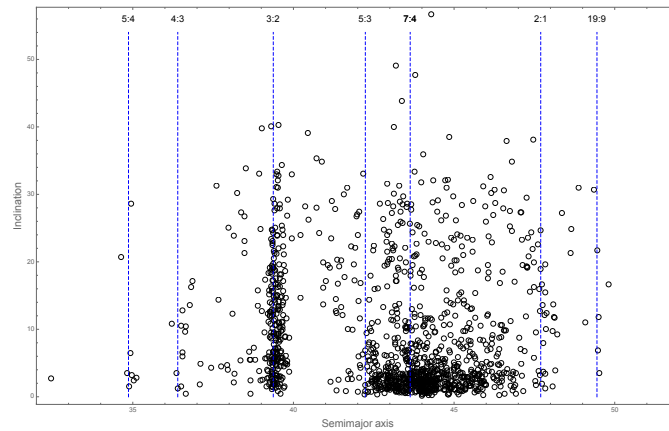
Figure 4.3: A plot of inclination against semi-major axis for observed Kuiper belt objects between 32 and 50 AU. The main mean motion resonances with Neptune are highlighted by blue dashed lines.

4.1.1   Resonant objects

The first objects to be classified are the resonant ones. They are important for the structure of the Kuiper belt, because they are allowed to exhibit large eccentric orbits that can survive for time lapses as long as the age of the Solar System, even if they approach Neptune or cross its orbit. Also, the chaotic nature of the resonance borders allows temporary trapping of scattered objects near the border of the resonance. Moreover, the relative population of the resonant objects can give clues about the rate of planet migration [HM05].

Resonant or near resonant objects can only be confirmed by a direct numerical calculation of the orbital evolution, because a period near a rational ratio of Neptune's is not at sufficient condition to be classified as resonant. To this end, the most likely orbit of the object is considered and also the two most extreme orbits than can match the actual path of the object. The three orbits are followed for ten million years and mean motion resonances with Neptune are examined. If the three orbits behaves in a resonant fashion, then the object is classified as resonant. If two of the three orbits present a resonant pattern then the object is classified as *insecure resonant* and further observations are needed to a definitive classification. If only one of the three orbits is resonant after ten million years, the object is termed as non resonant.

After classification, it is seen that a large number of objects is trapped in 3:2 mean motion resonance with Neptune at a distance of $a = 39.5 AU$, as it is observed in Figures 4.1-4.3. These objects have similar characteristics to Pluto and they are called *Plutinos*. Some other families of resonant objects, trapped at dif-

ferent resonances, have been also classified. In principle, there is no limitation on the order of the resonance, having observed objects in the resonances 4:3, 5:3, 7:4, 2:1, 5:2 that can be seen in Figures 4.2 and 4.3.

4.1.2 Nonresonant objects

If an object is not classified as resonant, it is said to be nonresonant. However, among these objects some different populations are considered, according to the orbital elements, in particular eccentricity and inclination. Basically, they are subdivided into two groups the scattered disc and the classical belt. A very simple criterion takes into account the perihelion distance $q = a(1 - e)$, in such a way that every Neptune crosser is classified as scattered and the rest as classical. However, this simple criterion does not take into account the dynamical evolution of the objects and a finer classification is desirable. The correct identification of the scattered objects is of great interest for the knowing of the source regions of comets, that are also potential objects to be captured as irregular moons [NCS$^+$08]. A study of the dynamical evolution of thousands of test bodies of the Kuiper belt shows an intricate boundary between scattered and non scattered objects [DLB95], so that the simple argument of the perihelion distance is not enough for a precise classification.

Scattered disc objects

The term *scattered disc* was originally intended for trans Neptunian objects scattered to high eccentric orbits with perihelion close to Neptune and semimajor axes greater than 50 AU [DL97]. The objects in this population are, in general, unstable and their orbital elements change with time, in particular the semimajor axis. This feature is then used to identify the population in the scattered disc. In this way, following Morbidelli et *al.* [MEL04], if the semi major axis of the more likely orbit, and those of the two extremal orbits, suffer a variation of 1.5 AU or more in a time lapse of ten million years, the object is classified as scattered. According this definition, these objects should be termed *scattering objects* rather than *scattered*, as their past evolution is not considered.

The scattered disc extends to objects not only with $a > 50$ AU, but also to objects with semimajor axes as small as 30 AU, in the limit with the Centaurs population. However, a cutoff must be set for the eccentricity, because high values of e yield coupling with Jupiter, and then the objects no longer belong to the Kuiper belt. On the other hand, objects with very large semimajor axes can be externally influenced and then there is also a cutoff to separate them from the objects in the inner Oort cloud [GMV08].

Detached trans-Neptunian objects

The discovery of objects like Sedna, with a perihelion distance of about 76 AU, initially classified as members of the scattered disc, led astronomers to introduce a new subpopulation in the Kuiper belt. Indeed, it is very unlikely these objects can be emplaced there by an encounter with Neptune, as its perihelion distance is clearly decoupled from the planet [GHG$^+$02]. This circumstance makes these objects to be only moderately affected by Neptune and the other known planets and makes them appear to be *detached* from the Solar System. For this reason they are termed *detached* [EAB03, DJ06, GMV08]

Numerical integration allows to separate the detached objects from the scattered objects. But it remains the problem about where the detached population should end at low eccentricity. In principle, it is possible to term all nonresonant, non scattered trans-Neptunian objects as *classical* objects of the Kuiper belt. However, it has not too much sense to consider in the same group objects like Sedna and objects in a circular orbit at the same perihelion distance. In this way, a lower bound for the eccentricity must be considered. It can be chosen arbitrarily, as Elliot et *al.* do [EKC$^+$05], taking $e = 0.2$. However, $e = 0.24$ seems to be preferable, because at moderate inclinations (10° - 20°) there are stable orbits interior to the 2:1 resonance that are better thought to be classical objects rather than detached. Moreover, this value introduce a symmetry respect to the eccentricity, in such a way that two stable objects with the same eccentricity on either side of the 2:1 resonance are classified as classical [GMV08].

Classical belt

By elimination, the objects not classified as resonant, scattered or detached are said to belong to the classical belt. We note that the classical belt is not confined to the interval between the 3:2 and the 2:1 resonance and includes objects outside these limits both in the inner and outer directions of the solar system. This yields to divide the classical belt into an *inner* classical belt, for those nonresonant objects with $a < 39.4$ UA, an *outer* classical belt, with $a > 48.4$ UA , $e < 0.24$ and nonresonant, and the *main* classical belt. The objects in the main belt are also known *cubewanos*, after the first discovered trans-Neptunian object 1992 QB1.

The objects in the classical belt were though to follow orbits with low inclination, but there are objects (e.g. 2004 DG77) with inclinations as high as $47.6°$. Thus, the inclination does not help to decide if an object belongs or not to the classical belt, but serves to divide the objects as *hot* or *cold* based on the orbital inclination. In this way, an inclination of $5°$ is sometimes taken to separate cold and hot objects. However, this cut reflects no dynamical separation.

4.2 Biases in the distribution of the observed object

The population of the observed Kuiper belt objects is not an unbiased sample of the total population, due to different factors that distort it. For instance, the main classical belt is mostly constituted by cold objects, as a consequence of the surveys, mainly confined to the ecliptic [Bro01]. Also, an additional population of cold objects is expected in the inner and outer discs [KJG⁺08], but a lack of them is clear in Figure 4.3. As surveys for the search of new Kuiper belt objects continue, researchers are aware about the great importance of having an assessment of all the observational bias in order to draw, as correct as possible, the true distribution of the material in the outer solar system beyond Neptune. We are not giving all the possible sources of bias, but we are going to mention the most obvious: the flux bias and the pointing bias, paying special attention to the second one, for which we will derive a theoretical approach.

4.2.1 Flux Bias

The most obvious bias is due to the limiting magnitude a survey is able to reach. In this way, brighter objects are easier to detect. For instance, two similar objects in size, but placed at different distances, do not have the same probability to be observed. In the same way, given two objects at a similar distance, the biggest one is more likely to be detected. Also the albedo, the fraction of radiation a body reflects, is a source of difference in the brightness. Thus, distance, size and albedo condition the probability of detection giving rise to the so called *flux bias* that makes up a disproportionate detected population.

Kuiper belt objects are discovered in the optical via reflected solar light. Assuming the same albedo for all of them, it is not difficult to see that the flux is proportional to the following expression [KJG⁺08]

$$\text{flux} \propto \frac{D^2}{\Delta^2 R^2},$$

where D is the object's diameter, Δ the distance to the Earth and R the distance to the Sun. This simple expression is enough to have an idea of the bias. For instance, if an object is 10 times larger than other one, it will be approximately 100 times brighter, which implies a difference of 5 magnitudes. On the other hand, for two objects of the same size, one of them situated at 30 AU and the other one at 60 UA, the first one is about 16 times brighter, that is a difference of 3 magnitudes. This can be readily seen from the expression for the apparent magnitude of a solar system body reflecting the solar light [KKO⁺07]

$$m = m_\odot - 5\log\frac{D}{2} + 2.5\log\frac{\Delta^2 R^2}{p(\chi)A}, \tag{4.1}$$

where $m_\odot$ is the apparent magnitude of the sun, A the object's albedo, $p(\chi)$ the phase integral, which can be taken the same for all objects, and D, R and Δ are given in astronomical units. From (4.1) it follows that if the albedo of an object is increased by a factor 2.5, it will be one magnitude brighter, and such differences in albedo are present in the Kuiper belt [LFL$^+$14]. For instance, a 100 Km across object at 40 AU with a typical albedo $A = 0.15$ [LFL$^+$14], will be observed with an apparent magnitude $m = 24.5$. The same object at a distance of 80 AU will have an apparent magnitude $m = 27.5$. In this sense, the knowledge of the true population of the Kuiper belt strongly depends on the flux limits of the survey, most of them with limiting magnitude around 24/25 [EKC$^+$05, KJG$^+$09, PKG$^+$11]. As a consequence, it is found that Plutinos represent a large fraction of the observed population, as they can be observed in the interior of Neptune's orbit and then easily to detect than objects in circular orbit at a distance of 40 UA. Besides, not too much is known about the population of small objects, say with a diameter of 10 Km or less, and also not too much about objects further than 50 AU.

4.2.2   Pointing Bias

This kind of bias is due to the design of the surveys conducted to the search of Kuiper Belt Objects. As a consequence, the inclination distribution of observed Kuiper Belt Objects is not representative of the real distribution. This is due to the fact that the majority of observations take place around the ecliptic and then the probability of detection of low-inclined objects is higher. Nevertheless, observation far from the ecliptic fails in detection of objects with inclinations less than the ecliptic latitude, and this is the reason why the surveys focus on a narrow band around the ecliptic [EKC$^+$05, KJG$^+$09, PKG$^+$11]. Taking these facts in mind, Brown [Bro01] developed a method to determining the unbiased distribution of Kuiper Belt Objects, that different authors have been used to study the dynamics of these objects [JWM05, VM11].

The method used by Brown has some limitations, as it is based upon the hypothesis of circular orbits. A discussion is made about the influence of the eccentricity in the inclination distribution and it is concluded that it does not affect significantly the total distribution. This conclusion follows from a Monte Carlo simulation, where it is assumed that orbital parameters, other than inclination and eccentricity, can be randomly chosen. However, the argument of perihelion also contributes to the observed distribution, because the time an object spends in the band around the ecliptic, where the survey is conducted, depends on both the eccentricity and the argument of perihelion. Thus, any bias in the inclination distribution yields a bias in the argument of perihelion distribution.

In this way, the distribution of the argument of perihelion should show some
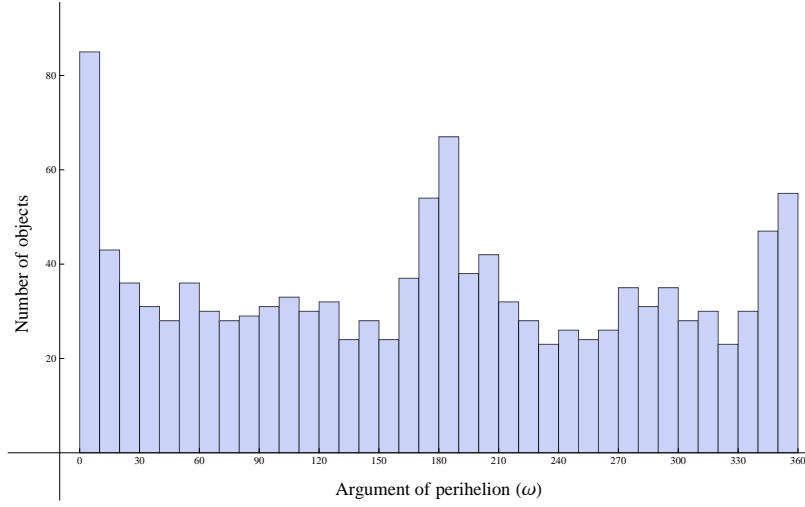
Figure 4.4: Histogram of the argument of perihelion for the known Kuiper Belt Objects, obtained from the data of Minor Planet Center in January of 2015.

deviations from the expected distribution, in this case a uniform one, as it is the case for the asteroids in the main belt (see [mpcb]). However, from the data available in Minor Planet Center [mpca], it can be readily seen that there is a cumulative number of objects around perihelion close to 0 and 180 degrees (see Figure 4.4). Even more, statistical tests show that the distribution is significantly far from a uniform one. Moreover, for the outermost objects, periapsis around $0°$ are the most frequent and there are no objects with $\omega \approx 180°$, as it should be expected. This fact is thought to be a signaling of the presence of trans-Plutonian planets [TS14, dlFMdlFM14].

Let us compute the probability to detect an object at an ecliptic latitude $-\delta \leq \beta \leq \delta$. It is proportional to the time the object spends in a band of width 2δ. In order to obtain this time, we recall that the ecliptic latitude of an object in elliptic orbit around the Sun is given by

$$\sin \beta = \sin i \sin(\omega + f), \tag{4.2}$$

where ω is the argument of perihelion and f the true anomaly of the object. If the orbit is circular, equation (4.2) reduces to

$$\sin \beta = \sin i \sin M,$$

where M is the mean anomaly. In this simple case, due to the symmetry, it is enough to consider $M \in [0, \pi/2]$. Thus, we have that the inequality $0 \leq \beta \leq \delta$ holds if

$$0 \leq \sin \beta = \sin i \sin M \leq \sin \delta.$$

Consequently, the object has an ecliptic latitude less than or equal to δ if

$$0 \leq M \leq \frac{\pi}{2}, \ i \leq \delta, \qquad 0 \leq M \leq \arcsin \frac{\sin \delta}{\sin i}, \ i > \delta.$$

Taking into account that the mean anomaly is proportional to time, we have

$$P(\delta, i) = \frac{2}{\pi} \arcsin \left[\min \left(\frac{\sin \delta}{\sin i}, 1 \right) \right], \qquad (4.3)$$

being $P(\delta, i)$ the probability to observe an object, in circular orbit inclined i degrees, in a 2δ wide band around the ecliptic. We can also obtain $P(\delta, i)$, by Monte Carlo simulations, taking a uniform time distribution of points along the orbit. Let be N the number of points in the distribution and m the number of points such that their corresponding ecliptic latitude belongs to the interval $[-\delta, \delta]$. Then, the probability $P(\delta, i)$ is given by

$$P(\delta, i) = \lim_{N \to \infty} \frac{m}{N}. \qquad (4.4)$$

This expression is general and can be used to estimate $P(\delta, i)$ for either circular and eccentric inclined orbits. In this sense, numerical simulations show that the probability of detection of an object in an inclined elliptic orbit is greater if the argument of the perigee is close to 0 or 180 degrees, as it is seen in Figure 4.5, where a density plot of the simulated probability is depicted for an orbit inclined $15°$ and $\delta = 6°$. Indeed, the probability is maximum at $\omega = 0°$ or $\omega = 180°$ and minimum if $\omega = 90°$. The differences between the maximum and minimum probabilities increase with the eccentricity. Moreover, in average, the probability is almost constant and equal to the circular case. To show this fact, we take a numerical simulation of the probability function fixing a value of $e = 0.3$ and taking a uniform sample of 50 values of ω in the interval $[0, \pi/2]$. We find that the difference between the average probability and the corresponding to the circular orbit is less than 10^{-5} (see Figure 4.6). This fact is in agreement with the simulations of Brown [Bro01].

We can conclude, from the numerical simulations, that the number of objects with argument of perihelion close to $0°$ and $180°$ must be greater than the number at any other angles. This is in agreement with Figure 4.4, but it seems that the big differences observed in the histogram cannot be explained by the observational bias.

To better understand the observational bias, we will give a theoretical derivation of the probability function using the asymptotic expansions of the elliptic motion.
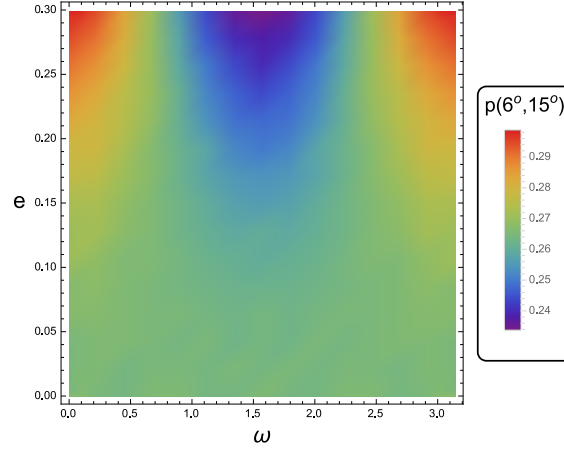
Figure 4.5: Density plot of the probability function to detect an object in a $15°$ inclined elliptic orbit in a $12°$ width band around the ecliptic, as a function of the eccentricity and the argument of perihelion.

Let us assume that the object follows an orbit with orbital elements i, e and ω, and let be

$$\alpha = \arcsin \frac{\sin \delta}{\sin i}.$$

Thus, from equation (4.2), the values of f delimiting the arcs of the orbit where the ecliptic latitude is less than or equal to δ are

$$f_1 = -\alpha - \omega, \quad f_2 = \alpha - \omega, \quad f_3 = \pi - \alpha - \omega, \quad f_4 = \pi + \alpha - \omega. \quad (4.5)$$

By means of the expansions of the elliptic motion [BC61, MD99], we have

$$M = f - 2e\sin f + \frac{3}{4}e^2\sin 2f - \frac{1}{3}e^3\sin 3f + \frac{1}{32}e^4(4\sin 2f + 5\sin 4f) + \dots \quad (4.6)$$

Substituting the values f_1, f_2, f_3 and f_4 in (4.6), we have that the total time the object spends in a band of width 2δ around the ecliptic is approximately given by

$$M_2 - M_1 + M_3 - M_4 \cong 4\alpha + \left(3e^2 + \frac{1}{2}e^4\right)\sin 2\alpha \cos 2\omega + \frac{5}{8}e^4\sin 4\alpha \cos 4\omega,$$

where the terms of the powers of the eccentricity greater than four have been neglected. Finally, the probability of detection, for the given orbital elements, results to be

$$P(\delta, i, \omega, e) \cong \frac{2}{\pi}\alpha + \left(\frac{3}{2\pi}e^2 + \frac{1}{4\pi}e^4\right)\sin 2\alpha \cos 2\omega + \frac{5}{16\pi}e^4\sin 4\alpha \cos 4\omega, \quad (4.7)$$
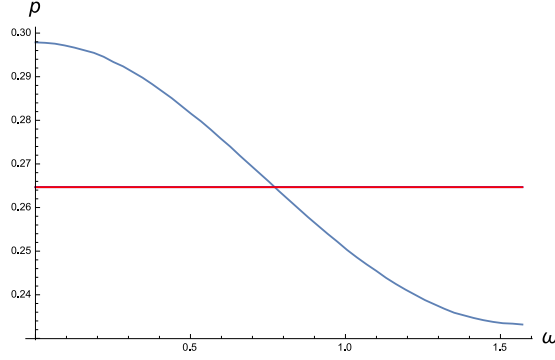
Figure 4.6: Numerical evaluation of the probability function when $e = 0.3$, $i = 15°$, $\delta = 6°$ and ω ranging from 0 to $\pi/2$. The horizontal straight line corresponds to the average value and also to the probability function for a circular orbit. To the scale of the picture the two lines appear superposed.

provided $i > \beta$. In other case, this probability is equal to one. From this expression we can obtain some interesting facts. On the one hand, taking the derivative respect to ω we find

$$\frac{dP(\delta, i, \omega, e)}{d\omega} = -\frac{6 + e^2(1 + 10\cos 2\alpha \cos 2\omega)}{2\pi} e^2 \sin 2\alpha \sin 2\omega.$$

As a consequence, the maximum and minimum probabilities of detection take place when $\sin 2\omega = 0$, that is at $\omega = 0$, $\pi/2$, π, and $3\pi/2$. By computing the second derivative, the probability is maximum at $\omega = 0$ and $\omega = \pi$ and minimum at the other two values. This confirms the results observed by numerical simulations. On the other hand, if we take the average of the probability function (4.7) over ω we obtain

$$\bar{P}(\delta, i, \omega, e) = \frac{1}{2\pi} \int_0^{2\pi} P(\delta, i, \omega, e)\, d\omega = \frac{2\alpha}{\pi}.$$

This means that, in average, we can take every orbit circular, a result we observed numerically.

It is also interesting to note that the function (4.7) is four fold symmetric respect to ω. Indeed, it is verified

$$P(\delta, i, \omega, e) = P(\delta, i, \omega - \pi, e) = P(\delta, i, \omega + \pi, e) = P(\delta, i, -\omega, e), \quad (4.8)$$

and we can restrict the study to periapsis in the interval $[0, \pi/2]$. In order to quantify the bias in the distribution, we focus on the ratio of the extreme values of the probability function given by

$$\frac{P_{max}}{P_{min}} = \frac{32\alpha + 4e^2(6 + e^2)\sin 2\alpha + 5e^4 \sin 4\alpha}{32\alpha - 4e^2(6 + e^2)\sin 2\alpha + 5e^4 \sin 4\alpha}.$$

Averaging over the eccentricity in the range $0 \leq e \leq 0.3$ we find that this ratio is close to 1.1, when $\delta = 6°$ and the inclination is grater than $10°$. So, this is the ratio we should have to find in the distribution of known objects. To check this aspect, we reduce the argument of perihelion of the known Kuiper Belt Objects in January 2015 to the interval $[0, \pi/2]$, making use of the four fold symmetry (4.8). We find this ratio to be very close to 2. As a consequence, there must be more reasons that affect the distribution of the argument of perihelion.

The effect of the distance

In order to find another factor that influence the distribution, we take into account the mean distance of the object to the Sun, while it is in the band around the ecliptic, where the survey is conducted. It is expected that the probability of detection of the object diminishes as the distance increases. We start from the equation

$$D = \frac{1 - e^2}{1 + e \cos f}, \tag{4.9}$$

that can be expanded in powers of the eccentricity

$$D = (1 - e^2)(1 - e \cos f + e^2 \cos^2 f - e^3 \cos^3 f + \cdots).$$

Taking into account the limits of the true anomaly that gives the intersection points of the orbit and the band around the ecliptic, given in equation (4.5), we obtain for the mean distance

$$\bar{D} = \frac{1}{(f_2 - f_1)} \int_{f_1}^{f_2} D \, df + \frac{1}{(f_4 - f_3)} \int_{f_3}^{f_4} D \, df,$$

and finally

$$\bar{D} = \frac{1 - e^2}{4\alpha}(4\alpha + e^2(2\alpha + \cos 2\omega \sin 2\alpha) + \cdots).$$

Contrary to what happened for the time spent in the band around the ecliptic, the mean distance is maximum at $\omega = 0°$ and $\omega = 180°$ and minimum at $\omega = 90°$ and $\omega = 270°$. Assuming that the probability is inversely proportional to the distance, the ratio of the maximum and minimum probability is around 1.02, when $\delta = 6°$ and $i > 10°$. Thus, the ratio between the number of objects with periapsis around $0°$ and periapsis around $90°$ must be corrected. In this way, taking into account the distance, this ratio should must be, approximately, $1.1/1.02 \approx 1.08$, which shows the predominance of the argument of the perihelion effect. As a result, there must be, approximately, a 8-10% more objects accumulated at perihelions of $0°$ and
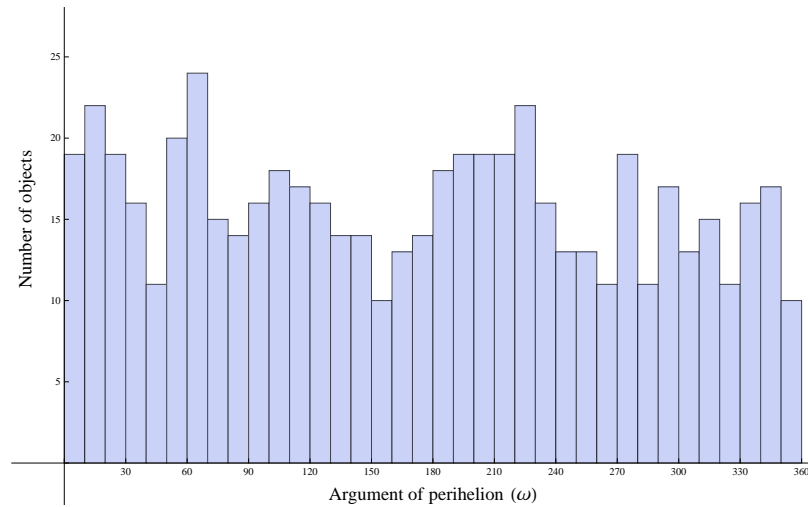
Figure 4.7: Histogram of the argument of perihelion of Kuiper Belt Objects recovered in two or more oppositions.

$180°$, but this is not observed in Figure 4.4, where this percentage appears to be clearly greater. In order to find an explanation to this deviation, we note that the argument of perihelion is one of the orbital elements of a Kuiper Belt Object determined with less accuracy [GMV08], even if the object has been recovered at several oppositions. If we restrict ourselves to those objects observed in two or more oppositions, we observe that the distribution of the argument of perihelion does not present so high concentrations around $0°$ and $180°$, as it it seen in Figure 4.7. Indeed, a Kolmogorov-Smirnov test leads to the conclusion that we cannot reject the hypothesis of a uniform distribution at a 10% confidence level, as the p-value obtained is $p = 0.141585$. Even more, the theoretical deviation is not observed clearly, although accumulations around $0°$ and $180°$ are more or less evident. Nevertheless, some peaks are attained at values of $\omega \approx 65°$ and $\omega \approx 215°$. While the second one is close to $180°$, the other value would deserve a more detailed examination, that is out of the scope of this dissertation.

If we now pay attention to the distribution of the objects with a poorly determined orbit, that is those observed only in one opposition, we can observe a clear accumulation of ω values around $0°$ and $180°$, as it can be seen in Figure 4.8. From this, we can conclude that preliminary orbits assigned to Kuiper Belt Objects are biased to give a value of ω near $0°$ and $180°$. Indeed, this fact is related to another of the important bias, as it is *ephemeris bias*. For instance, for an object observed for a few days, only its distance and the inclination of its orbit can be estimated with some accuracy [KJG+08]. The rest of the elements cannot be determined in a precise way an most of the times a circular orbit is assumed. As a result of
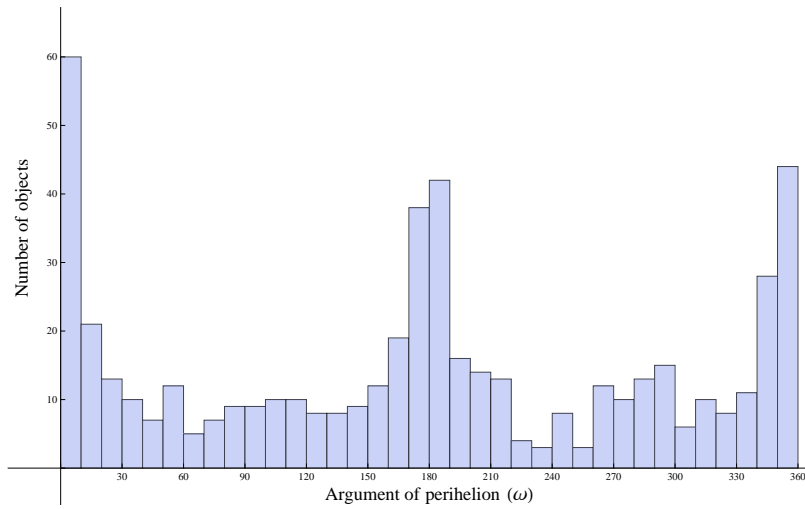
Figure 4.8: Histogram of the argument of perihelion of Kuiper Belt Objects observed one time.

a poorly determined orbit, it is difficult to predict the future positions and some objects are lost, causing a distortion in the distribution of the orbital elements.

There is still another important bias, related to the detection of the Kuiper belt objects from the images obtained in the survey. The method used is a blinking process, that compares two images in order to detect moving points. However, the arcs covered by objects at large distances are very short and thus these objects are hardly to pick up, especially those beyond a distance of 75 AU [KJG$^+$08]. In summary, if we consider all the biases mentioned, it is very unlikely that objects in very inclined orbits, with diameters less than 500 Km and at a distance greater than 50 AU can be detected. Therefore, the observed population is no more than a biased sample of the real population of the Kuiper belt and every conclusion derived from the known population must be properly corrected.

Conclusions and further work

The main conclusions reached in the development of this thesis can be summarized in the following items

- The planar circular restricted $2 + 2$ body problem is a suitable model to account for a capture mechanism in the vicinity of giant planets by an energy exchange process, when close encounters between the minor bodies take place. This model can be seen as a system of two independent circular restricted three-body problems, coupled by a term that only matters when the minor bodies are close.

- As we are only interested in the motion of the small bodies around the planet, Hill approximation has been introduced. In this way, we have arrived at a simplified model that retains the main characteristics of the full problem. In particular, it is the sum of two Hill approximations of the restricted three body problem for each of the small masses, coupled by their mutual interaction.

- Due to the presence of collisions, the model has different singularities that are a source of problems and instabilities when the equations of the motion are numerically integrated. In order to avoid these singularities, we have considered two different regularizations: the Levi-Civita regularization for close encounters between a minor body with small primary and the Waldvogel regularization for close encounters between the two minor bodies. A specific code for the numerical integration of the equations of the motion has been developed, switching from one set of regularized coordinates to the other one through cartesian coordinates.

- A synthetic population of initial conditions for those objects suitable for a capture has been produced on the basis of the Monte Carlo method. Starting from a uniform distribution of objects inside the Hill sphere with uniform distributed energy, only objects that enter and leave the Hill sphere and live inside it a minimum prefixed time are considered. About 1% of the quarter million initial population was selected at the end.

- Every pair of the synthetic initial population is a candidate to give a capture object, which is considered trapped if it lives more than 20 000 planetary periods inside the Hill sphere. However, provided that the number of potential pairs is more than two millions, and checking all of them we have considered samples of 50 000pairs to perform a basic statistic study of the capture rate and other important features. In this way, we have showed that the mass ratio plays an important role. In fact, the capture rate depends on it, in such a way that it increases when the mass ratio also increases. Besides, the final result of the interaction of two bodies is very sensitive to the mass ratio, being in some cases almost unpredictable.

- We have also showed that, in general, the trapped objects lose energy, and almost half of them lose enough energy to be permanently confined inside the Hill sphere, as their final energy is below that of the saddle point. We have also showed that about 63% of the captured objects follow a mixed type orbit, nor prograde, nor retrograde and that only about 11% move in a retrograde orbit.

- One of the most interesting facts we have showed is that the capture process works in a great variety of situations. Particularly relevant are the captures corresponding to objects in collision trajectory with the planet or to objects that follow a close path.

- Finally, we have performed a statistical study of Kuiper belt objects, as a source region for the irregular satellites. We have focused in the pointing bias and we have established a theoretical probability function for the detection of KBO depending on the inclination, eccentricity, argument of perihelion and ecliptic latitude, in accordance to the Monte Carlo simulations conducted by other authors. Also, a bias in the assignment of the argument of perihelion for preliminary orbits is detected.

Although the model proposed here is able to account for captured objects, it fails to give a predominant population of retrograde captured satellites and also the final eccentricity of the orbits are too high, in contrast with the observed one. These facts motivate us to further investigate this model by considering the lines of a future work we highlight in the following points:

- The model considered is just a planar one and it is strictly necessary to study the spatial case if we want to contrast the model with the real observations. In this way, it is possible that the spatial case can be able to account for a predominate number of retrograde objects.

- Another important issue that deserves further investigation is the selection of the initial population of objects. The cutoffs for the lifetime and energy fixed in this dissertation have to be reconsidered.

- Although the model predicts captured objects, these follow very eccentric orbits. To have moderate eccentricities we need to introduce drag forces or the interaction with the regular moons of the planets.

- It is necessary to conduct a statistical study to link the population of irregular moons with the objects in the Kuiper belt, specially those classified as scattered.

Appendix A

Monte Carlo Methods

Monte Carlo method is a numerical tool for solving mathematical problems by random sampling. In the form it is known nowadays, it is attributed to Enrico Fermi, John von Neumann, Nicholas Metropolis and Stanislaw Ulam [MU49]. It was Ulam who developed it to solve a problem related to neutron transport, during the secret research at Los Alamos for the construction of the atomic bomb in world war II. The name of the method was the code given by Metropolis, inspired by the gambling casinos at the city of Monte Carlo in Monaco.

After the publication of the seminal paper by Metropolis and Ulam in 1949 [MU49], the method became popular in the fields of physics, physical chemistry, and operations research and then it began to find a wide application in many different areas. The typical Monte Carlo approach tries to simplify problems as much as possible. However, the use of computers allows to generate modern Monte Carlo codes that require fewer approximations and provide more accurate solutions. This opens the possibility to cope with problems that could not be solved before entailing a large number of new applications. It can be said that Monte Carlo method is a very general mathematical tool, that includes a large and still growing collection of simulation methods, designed to obtain approximate solutions of different problems, by playing games of chance. Besides, those algorithms that make use of pseudorandom numbers are generally called Monte Carlo algorithms or methods. They are usually divided into two major groups. The first one consists on direct simulations of systems that are already statistical in their nature. In such cases, it is not even necessary to have well defined mathematical equations describing the behavior of the system. The second group, on the contrary, are devised for the solution of well defined mathematical equations. In such cases the methods are used to solve the equations that describe the problem of interest.

Originally, Monte Carlo method was not a simulation method, but a mathematical approach aimed to solve a multidimensional integro-differential equation

by means of a stochastic process. The equation itself did not necessarily refer to a stochastic process. However, when the method is applied to a physical stochastic process, such as neutron diffusion, the model could be identified with the process itself. Under those circumstances, the Monte Carlo method represents a simulation technique, since every step of the model is aimed to mimic an identical step in the physical process. This is precisely the approach we used in Chapter 3.

A.1   Sampling: the basic idea

The main idea of the method relies on the generation of random variables. This is usually exemplified by one of the main applications of Monte Carlo method, as it is the computation of integrals. In this way, let us suppose we want to obtain the area of a quarter of circle of unit radius. We can inscribe it into a square of side one and then proceed in the following way:

1. Select at random N points, $(x_j, y_j), j = 1, \ldots, N$, inside the square. This can be done by selecting random numbers in the interval $[0, 1]$.

2. Check for each point if the inequality $x_j^2 + y_j^2 \leq 1$ holds and let N_I the number of points satisfying the inequality.

3. The approximate value of the area is given by $A = \frac{N_I}{N}$.

The procedure is depicted in Figure A.1 and it seems clear that the quotient N_I/N is an approximation of the ratio between the area we want to find and the area of the unit square. Being this area equal to one, N_I/N is just what we are looking for. If we take $N = 1000$ we find, in one run, $A = 0.783$, while the true value is $A = \pi/4 \approx 0.7854$. Note, that this method could serve to estimate the value of the constant π.

The above example is no more than a particular case of the so called Monte Carlo integration. In the simple case, the aim is to get the value of the integral

$$I = \int_a^b f(x)\,dx.$$

To this end, let us choose N random numbers, x_j $(j = 1, \ldots, N)$, in the interval $[a, b]$. Then, a crude approximation of I is given by

$$I = (b - a)\frac{\sum_{j=1}^N f(x_j)}{N} = \sum_{j=1}^N f(x_j)\frac{b-a}{N}. \tag{A.1}$$
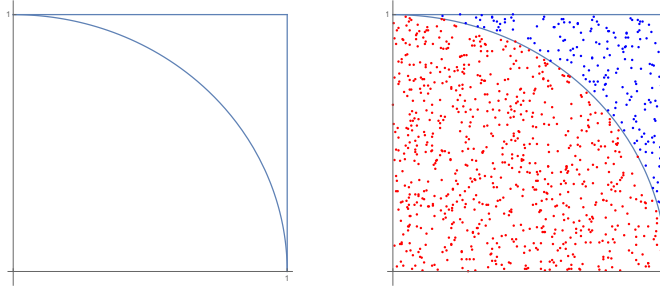
Figure A.1: The Monte Carlo method to approximate the area of a quarter or circle of unit radius. The area is approximately the ratio between the red dots and the total number of dots.

The above equation (A.1) can be viewed as an expectation value of a random variable uniformly distributed in the interval $[a, b]$. Indeed,

$$I = (b - a) \int_a^b f(x) \frac{1}{b - a} dx = (b - a) E[f(x)],$$

being $E[f(x)]$ the expected value of $f(x)$ under a uniform distribution. In this way, the Monte Carlo method serves to solve one or both of the following more general problems:

- To generate samples $\{\mathbf{x}_j\}_{j=1}^N$ from a given probability distribution $P(\mathbf{x})$.[1]

- To obtain the expected value of a function f under this distribution:

$$E[f(\mathbf{x})] = \int_\chi f(\mathbf{x}) P(\mathbf{x}) d^n \mathbf{x},$$

  where χ is the support of the random variable $\mathbf{x}$, or the set where it takes values. Moreover, $\mathbf{x}$ will be generally assumed to be an n-dimensional vector with real components, although the discrete case can also be considered.

If the first problem is solved, then, by using the random sampling $\{\mathbf{x}_j\}_{j=1}^N$, we have the estimate

$$\hat{f} = \frac{1}{N} \sum_{j=1}^N f(\mathbf{x}_j).$$

---

[1]Here the concept of sample is not the usual one, but a single realization of the random variable with density function $P(\mathbf{x})$.

It is clear that, if each $\mathbf{x}_j$ is generated from $P(\mathbf{x})$, then the expected value of $\hat{f}$ is $E[f(\mathbf{x})]$. Moreover, if σ^2 is the variance of f under the density function $P(\mathbf{x})$,

$$\sigma^2 = \int_\chi (f(\mathbf{x}) - E[f(\mathbf{x})])^2 P(\mathbf{x}) d^n\mathbf{x},$$

then the variance of $\hat{f}$ will be σ^2/N, which proves the convergence of $\hat{f}$ to the true value of the integral.

A.2   The Law of Large Numbers and the Central Limit Theorem

The convergence suggested above relies on the Law of Large Numbers, which is stated as follows [Bil95].

Theorem 1 (Law of Large Numbers) *Let $X_1, X_2, \ldots, X_N$ be an independent trials process, with finite expected value $\mu = E(X_j)$ and finite variance $\sigma^2 = V(X_j)$. Let $S_N = X_1 + X_2 + \cdots + X_N$. Then for any $\varepsilon > 0$,*

$$P\left(\left|\frac{S_N}{N} - \mu\right| \geq \varepsilon\right) \to 0$$

as $N \to \infty$. Equivalently,

$$P\left(\left|\frac{S_N}{N} - \mu\right| < \varepsilon\right) \to 1$$

as $N \to \infty$.

The proof is based on the well known Chebyshev inequality: If X is a random variable with expected value $\mu = E(X)$ and $\varepsilon > 0$ is any positive real number, then

$$P(|X - \mu| \geq \varepsilon) \leq \frac{V(X)}{\varepsilon^2}.$$

The other important result for the Monte Carlo method is the Central Limit Theorem that gives more insight about the distribution of a sum of independent random variables that describes the size and distribution of the stochastic fluctuations around the deterministic number μ during this convergence. Here, we state the Central Limit Theorem for N independent random variables identically distributed, which is know as the Lindeberg-Lévy theorem [Bil95].

Theorem 2 (Central Limit Theorem) *Let $X_1, X_2, \ldots, X_N$ be independent and identically distributed random variables with common mean μ and finite positive variance σ^2 and let $T_n = X_1 + \cdots X_N$. Then, for all $a \in \mathbb{R}$*

$$P\left(\frac{T_N - N\mu}{\sigma\sqrt{N}} \leq a\right) - \Phi(a) \to 0$$

as $N \to \infty$, where $\Phi(a) = P(z \leq a)$, being z a normal distributed random variable with mean 0 and variance 1.

The application of the Monte Carlo method can be understood as the calculation of some unknown quantity μ. To this end, we look for a random variable X such that its expected value, or mean, is equal to μ. Moreover, we will assume that the variance is equal to σ^2. Now, let us consider N independent random variables $X_1, X_2, \ldots, X_N$ identically distributed, with the same distribution as X. If N is large enough, the Central Limit Theorem ensures that that the distribution

$$X_N = X_1 + X_2 + \cdots + X_N$$

is approximately normal with mean $N\mu$ and variance $N\sigma^2$. Taking into account the *three sigmas rule* [Sob94] it follows that

$$P\left(N\mu - 3\sigma\sqrt{N} < X_N < N\mu + 3\sigma\sqrt{N}\right) \approx 0.997$$

or, equivalently,

$$P\left(\left|\frac{1}{N}\sum_{j=1}^{N} X_j - \mu\right| < \frac{3\sigma}{\sqrt{N}}\right) \approx 0.997. \tag{A.2}$$

This relation is of great importance for Monte Carlo method, giving us both the way to calculate μ and an error estimate. On the one hand, μ is obtained by choosing N independent variables which is equivalent to select N different values of X. This is the sampling mentioned in section A.1. From (A.2) it is clear that the arithmetic mean of X_j converges to μ as N goes to infinity and an error bound is given by $3\sigma/\sqrt{N}$. However, this error is not convenient in practical computations and it is more convenient to use the *probable error* [Sob94] given by

$$r_N = 0.6745\frac{\sigma}{\sqrt{N}}, \tag{A.3}$$

which is a characterization of the absolute error

$$\left|\frac{1}{N}\sum_{j=1}^{N} X_j - \mu\right|.$$

A.3   Peculiarities of Monte Carlo Method

We can summarize the most important features of Monte Carlo method in the two following items

- The algorithm has a very simple structure. As a rule, it consists on a program for performing a random test. After this test is repeated N times, so that each experiment is independent of the remaining, the mean of the results of all experiments is taken. For this the reason sometimes Monte Carlo method is called a statistical test.

- The error is, as a rule, proportional to the magnitude $\sqrt{D/N}$, where D is a constant and N is the number of tests. From this formula we can see that to reduce the error by a factor 10, the number of tests, N, must be increased by a factor 100. This shows that not always high accuracy is achieved and Monte Carlo proves to be especially effective in solving problems when not too much accuracy (5 to 10 percent) is required. However, different variants of the Monte Carlo method significantly increase the accuracy by choosing a method which corresponds to a much lower values of D

These two peculiarities can be observed in the example given in section A.1, where we aimed to calculate the area of a quarter of circle of unit radius. In fact, the algorithm is very simple and the error can be estimated taking into account that the random value N_I is given by the sum

$$N_I = X_1 + X_2 + \cdots X_N$$

where $X_j = 0$ if the jth point is inside the circle and 0 otherwise. Each X_j is independent of the rest of random variables and all them have a common distribution

$$X \sim \left(\begin{array}{cc} 1 & 0 \\ A & 1 - A \end{array} \right),$$

where A is the area of the quarter of circle, which is the also the probability that a random selected point lies inside it. Thus, we obtain

$$\mu = E(X) = A, \qquad \sigma^2 = V(x) = A(1 - A),$$

and the variance of the estimate N_I/N is equal to

$$V(N_I/N) = V(X)/N = A(1 - A)/N.$$

Finally, the probable error (A.3) is now

$$r_N = 0.6745\sqrt{A(1 - A)/N}.$$

Taking into account that in our simulation $A = \pi/4$ and $N = 1000$, we obtain for the probable error $r_N = 0.00875676$, which is close to the observed error

$$|0.783 - \pi/4| = 0.00239816.$$

It is worth noting that the theoretical error indicates that we can get the area with accuracy of one decimal figure. If we want to increase the accuracy to three decimal figures it will be necessary to perform a simulation with approximately ten millions of pints.

Bibliography

[ABWF03]   S. A. Astakhov, A. D. Burbanks, S. Wiggings, and D. Farrelly. Chaos-assisted capture of irregular moons. *Nature*, 423:264–267, 2003.

[AF04]   S. A. Astakhov and D. Farrelly. Capture and escape in the elliptic restricted three-body problem. *Monthly Notices of the Royal Astronomical Society*, 354:971–979, 2004.

[BAB$^+$03]   G. M. Bernstein, R. L. Allen, M. E. Brown, M. J. Holman, R. Malhotra, and D. E. Trilling. The size distribution of Kuiper Belt Objects from a Deep HST/ACS Survey. *Bulletin of the American Astronomical Society*, 35:1015, 2003.

[BC61]   D. Brouwer and G. M. Clemence. *Methods of Celestial Mechanics*. Academic Press, New York, 1961.

[BCD01]   L. D. Brown, T. T. Cai, and A. DasGupta. Interval Estimation for a Binomial Proportion. *Statistical Science*, 16(2):101–133, 2001.

[BG97]   June Barrow-Green. *Poincaré and the Three Body Problem*. American Mathematical Society, Providence, Rhode Island, 1997.

[Bil95]   P. Billingsley. *Probability and Measure*. John Wiley & sons, New Jersey, 1995.

[BM94]   L. A. M. Benner and W. B. McKinnon. Pre-Impact Orbital Evolution of P/Shoemaker-Levy 9. In *Abstracts of the 25th Lunar and Planetary Science Conference, held in Houston, TX, 14-18 March 1994.*, page 93, 1994.

[Bro01]   M. E. Brown. The inclination distribution of the Kuiper belt. *The Astronomical Journal*, 121:2804–2814, 2001.

91

[CLSD95]   A. L. Cochran, H. F. Levison, S. A. Stern, and M. J. Duncan. The discovery of Halley-sized Kuiper belt objects using the Hubble Space Telescope. *The Astrophysical Journal*, 455:342–346, 1995.

[Con02]   G. Contopoulos. *Order and Chaos in Dynamical Astronomy*. Springer, New York, 2002.

[CW02]   R. M. Canup and W. R. Ward. Formation of the Galilean Satellites: Conditions of Accretion. *The Astronomical Journal*, 124:3404–3423, 2002.

[CW06]   R. M. Canup and W. R. Ward. A common mass scaling for satellite systems of gaseous planets. *Nature*, 44:834–839, 2006.

[DJ06]   A. Delsanti and D. Jewitt. *Solar System Update*, chapter The solar system beyond the planets, pages 267–294. Springer-Praxis, 2006.

[DL97]   M. J. Duncan and H. F. Levison. A scattered comet disk and the origin of Jupiter family comets. *Science*, 276:1670–1672, 1997.

[DLB95]   M. J. Duncan, H. F. Levison, and S. M. Budd. The dynamical structure of the Kuiper belt. *The Astronomical Journal*, 110:3073–3081, 1995.

[dlFMdlFM14] C. de la Fuente Marcos and R. de la Fuente Marcos. Extreme trans-Neptunian objects and the Kozai mechanism: signalling the presence of trans-Plutonian planets. *Monthly Notices of the Royal Astronomical Society*, 443:L59–L63, 2014.

[dlFMdlFM16] C. de la Fuente Marcos and R. de la Fuente Marcos. Finding Planet Nine: a Monte Carlo approach. *Monthly Notices of the Royal Astronomical Society*, 459:L66–L70, 2016.

[EAB03]   V. V. Emel'yanenko, D. J. Asher, and M. E. Bailey. A new class of trans-Neptunian objects in high-eccentricity orbits. *Monthly Notices of the Royal Astronomical Society*, 338:443–452, 2003.

[Edg49]   K. E. Edgeworth. The origin and evolution of the Solar System. *Monthly Notices of the Royal Astronomical Society*, 109:600–609, 1949.

[EKC+05]   J. L. Elliot, S. D. Kern, K. B. Clancy, A. A. S. Gulbis, R. L. Millis, M. W. Buie, L. H. Wasserman, E. I. Chiang, A. B. Jordan, D. E.

Trilling, and K. J. Meech. The deep ecliptic survey: a search for Kuiper belt objects and Centaurs. II. Dynamical classification, the Kuiper belt plane, and the core population. *The Astronomical Journal*, 129:1117–1162, 2005.

[Euc96]   Euclides. *Elementos*. Gredos, 1996.

[Fer80]   J. A. Fernández. On the existence of a comet belt beyond Neptune. *Monthly Notices of the Royal Astronomical Society*, 192:481–491, 1980.

[GHG⁺02]   B. Gladman, M. Holman, T. Grav, J. Kavelaars, P. Nicholson, K. Aksnes, and J. M. Petit. Evidence for an Extended Scattered Disk. *Icarus*, 157:269–279, 2002.

[GMV08]   B. Gladman, B. G. Marsden, and C. Vanlaerhoven. *The Solar System Beyond Neptune*, chapter Nomenclature in the Outer Solar System, pages 43–57. University of Arizona Press, Tucson, 2008.

[GWN11]   H. S. Gaspar, O. C. Winter, and E. Vieira Neto. Irregular satellites of Jupiter: capture configurations of binary-asteroids. *Monthly Notices of the Royal Astronomical Society*, 415:1999–2008, 2011.

[GWN13]   H. S. Gaspar, O. C. Winter, and E. Vieira Neto. Irregular satellites of Jupiter: three-dimensional study of binary-asteroid captures. *Monthly Notices of the Royal Astronomical Society*, 433:36–46, 2013.

[Hén71a]   M. Hénon. The Monte Carlo Method. *Astrophysics and Space Science*, 14:151–167, 1971.

[Hén71b]   M. Hénon. Monte Carlo Models of Star Clusters. *Astrophysics and Space Science*, 13:284–299, 1971.

[Hil78]   G. W. Hill. Researches in the Lunar Theory. *American Journal of Mathematics*, 1:5–26, 129–147, 245–260, 1878.

[Hil86]   G. W. Hill. On the part of the motion of the lunar perigee which is a function of the mean motions of the Sun and the Moon. Reprinted in *Acta Mathematica*, 8:1–36, 1886.

[HM05]   J. M. Hahn and R. Malhotra. Neptune's migration into a stirred-up Kuiper belt: A detailed comparison of simulations to observations. *The Astronomical Journal*, 130:2392–2414, 2005.

[HP86]   M. Hénon and J. M. Petit. Series expansions for encounters-type solutions of Hill's problem. *Celestial Mechanics*, 38:67–100, 1986.

[JH07]   D. Jewitt and N. Haghighipour. Irregular Satellites of the Planets: Products of Capture in the Early Solar System. *Annual Review of Astronomy and Astrophysics*, 45:261–295, 2007.

[JL93]   D. Jewitt and J. Luu. Discovery of the candidate Kuiper belt object 1992 QB_1. *Nature*, 362:730–732, 1993.

[JS04]   D. Jewitt and S. Sheppard. Irregular satellites in the context of planet formation. *Space Science Reviews*, 114:407–421, 2004.

[JWM05]   D. C. Jones, I. P. Williams, and M. D. Melita. The dynamics of objects in the inner Edgeworth-Kuiper belt. *Earth, Moon and Planets*, 97:435–458, 2005.

[KJG$^+$08]   J. J. Kavelaars, L. Jones, B. Gladman, J. Wm. Parker, and J. M. Petit. *The Solar System Beyond Neptune*, chapter The Orbital and Spatial Distribution of the Kuiper Belt, pages 59–69. University of Arizona Press, Tucson, 2008.

[KJG$^+$09]   J. J. Kavelaars, R. L. Jones, B. J. Gladman, J. M. Petit, J. Wm. Parker, C. Van Laerhoven, P. Nicholson, P. Rousselot, H. Scholl, O. Mousis, B. Marsden, P. Benavidez, A. Bieryla, A. Campo Bagatin, A. Doressoundiram, J. L. Margot, I. Murray, and C. Veillet. The Canada-France Ecliptic Plane Survey-L3 Data Release: The Orbital Structure of the Kuiper Belt. *The Astronomical Journal*, 127:4917–4935, 2009.

[KKO$^+$07]   H. Karttunen, P. Kröger, H. Oja, M. Poutanen, and K. J. Donner. *Fundamental Astronomy*. Springer, New York, 5th edition edition, 2007.

[Kor05]   S. J. Kortenkamp. An efficient, low-velocity, resonant mechanism for capture satellites by a protoplanet. *Icarus*, 175:409–418, 2005.

[KS65]   P. Kustaanheimo and E.L. Stiefel. Perturbation theory of Kepler motion based on spinor regularization. *Journal für die Reine und Angewandte Mathematik*, 218:204–219, 1965.

[Kui51a]   G. P. Kuiper. On the origin of the irregular satellites. *Proceedings of the National Academy of Sciences*, 37:717–721, 1951.

[Kui51b]   G. P. Kuiper. On the origin of the Solar System. *Proceedings of the National Academy of Sciences*, 37(1):1–14, 1951.

[Kui56]   G. P. Kuiper. On the Origin of the Satellites and the Trojans. *Vistas in Astronomy*, 2:1631–1666, 1956.

[Lan94]   R. R. Landis. Comet P/Shoemaker-Levy's Collision with Jupiter: Covering HST's Planned Observations from Your Planetarium. http://www.seds.org/sl9/landis.html. In *Proceedings of the International Planetarium Society Conference held at the Astronaut Memorial Planetarium & Observatory, Cocoa, Florida, July 10-16 1994*, 1994.

[LC20]   T. Levi-Civita. Sur la régularisation du problème des trois corps. *Acta Mathematica*, 42:99–144, 1920.

[Lev96]   H. F. Levison. Comet taxonomy. In T. W. Rettig and J. M. Hahn, editors, *Completing the Inventory of the Solar System*, volume 107 of *ASP Conference Series*, pages 173–191, San Francisco, 1996.

[LFL$^+$14]   P. Lacerda, S. Fornasier, E. Lellouch, C. Kiss, E. Vilenius, P. Santos-Díaz, M. Rengel, T. Müller, J. Stansberry, R. Duffard, A. Delsanti, and A. Guilbert-Lepourte. The Albedo-Color Diversity of Tansneptunian Objects. *The Astrophysical Journal Letters*, 793:L2 (6pp), 2014.

[LR11]   J. Llibre and L. A. Roberto. On the periodic orbits and the integrability of the regularized Hill lunar problem. *Journal of Mathematical Physics*, 52:082701/8, 2011.

[Mal95]   R. Malhotra. The origin of Pluto's orbit: implication for the Solar System beyond Neptune. *The Astronomical Journal*, 110:420–429, 1995.

[MD99]   C. D. Murray and S. F. Dermott. *Solar system dynamics*. Cambridge University Press, 1999.

[MDL00]   R. Malhotra, M. J. Duncan, and H. F. Levison. Dynamics of the Kuiper belt. In V. Mannings, A. P. Boss, and S. S. Russell, editors, *Protostars and Planets IV*, pages 1231–1245, Tucson, 2000. University of Arizona Press.

[ME03a]   I. Mosqueira and P. R. Estrada. Formation of the regular satellites
                of giant planets in an extended gaseous nebula I: subnebula model
                and accretion of satellites. *Icarus*, 163:198–231, 2003.

[ME03b]   I. Mosqueira and P. R. Estrada. Formation of the regular satel-
                lites of giant planets in an extended gaseous nebula II: satellite
                migration and survival. *Icarus*, 163:232–255, 2003.

[MEL04]   A. Morbidelli, V. V. Emel'yanenko, and H. F. Levison. Origin and
                orbital distribution of the trans-Neptunian scattered disc. *Monthly
                Notices of the Royal Astronomical Society*, 335:935–940, 2004.

[MHO09]   K. Meyer, G. Hall, and D. Offin. *Introduction to Hamiltonian
                Dynamical Systems and the N-Body Problem*. Springer-Verlag
                New York, 2009.

[ML95]   W. B. McKinnon and A. C. Leith. Gas drag anf the orbital evolu-
                tion of a captured Triton. *Icarus*, 118(2):392–413, 1995.

[MLTG05]   A. Morbidelli, H. F. Levison, K. Tsiganis, and R. S. Gomes.
                Chaotic capture of Jupiter's Trojan asteroids in the early Solar
                System. *Nature*, 435:462–465, 2005.

[mpca]   http://www.minorplanetcenter.net.

[mpcb]   http://www.minorplanetcenter.net/iau/plot/orbels05.gif.

[MU49]   N. Metropolis and S. Ulam. The Monte Carlo Method. *Journal
                of the American Statistical Association*, 44(247):335–341, 1949.

[NCS$^+$08]   P. D. Nicholson, M. Ćuk, S. S. Sheppard, D. Nesvorný, and T. V.
                Johnson. *The Solar System Beyond Neptune*, chapter Irregular
                Satellites of the Giant Planets, pages 411–424. University of Ari-
                zona Press, Tucson, 2008.

[NVD14]   D. Nesvorný, D. Vokrouhlický, and R. Deienno. Capture of Ir-
                regular Satellites at Jupiter. *The Astrophysical Journal*, 784:22
                (6pp), 2014.

[NVM07]   D. Nesvorný, D. Vokrouhlický, and A. Morbidelli. Capture of
                irregular satellites during planetary encounters. *The Astronomical
                Journal*, 133:1962–1976, 2007.

[OIY+08]   K. Ohtsuka, T. Ito, M. Yoshikawa, D. J. Asher, and H. Arakida. Quasi-Hilda comet 147P/Kushida-Muramatsu. Another long temporary satellite capture by Jupiter. *Astronomy and Astrophysics*, 289(3):1355–1362, 2008.

[PBT79]   J. B. Pollack, J. A. Burns, and M. E. Tauber. Gas Drag in Primordial Circumplanetary Envelopes: A Mechanism for Satellite Capture. *Icarus*, 37:587–611, 1979.

[PH86]   J. M. Petit and M. Hénon. Stellite Encounters. *Icarus*, 66:536–555, 1986.

[PH87a]   J. M. Petit and M. Hénon. A numerical simulation of planetary rings i. Binary encounters. *Astronomy and Astrophysics*, 173:389–404, 1987.

[PH87b]   J. M. Petit and M. Hénon. A numerical simulation of planetary rings ii. Monte Carlo model. *Astronomy and Astrophysics*, 188:198–205, 1987.

[PHA10]   C. M. Philpott, D. P. Hamilton, and C. B. Agnor. Three-body capture of irregular satellites: Application to Jupiter. *Icarus*, 208:824–836, 2010.

[PKG+11]   J. M. Petit, J. J. Kavelaars, B. J. Gladman, R. L. Jones, J. Wm. Parker, C. Van Laerhoven, P. Nicholson, G. Mars, P. Rousselot, O. Mousis, B. Marsden, A. Bieryla, M. Taylor, M. L. N. Ashby, P. Benavidez, A. Campo Bagatin, and G. Bernabeu. The Canada-France ecliptic plane survey-full data release: The orbital structure of the Kuiper belt. *The Astronomical Journal*, 142:131–153, 2011.

[RMW+16]   C. L. Rodriguez, M. Morscher, L. Wand, S. Chatterjee, F. A. Rasio, and R. Spurzem. Million-body star cluster simulations: comparisons betweenn Monte Carlo and direct n-body. *Monthly Notices of the Royal Astronomical Society*, 463:2109–2118, 2016.

[Ros07]   S. M. Ross. *Introducción a la Estadística*. Reverté, S.A., Barcelona, 2007.

[RW06]   D. C. Richardson and K. J. Walsh. Binary Minor Planets. *Annual Review of Earth and Planetary Science*, 34:47–81, 2006.

[SCC01]   M. C. De Sanctis, M. T. Capria, and A. Coradini. Thermal evo-
             lution and differentiation of Edgeworth-Kuiper bel objects. *The
             Astronomical Journal*, 121:2792–2799, 2001.

[Sha78]   D. Shanks. *Solved and Unsolved Problems in Number Theory*.
             Chelsea Publishing Company, second edition, 1978.

[Sob94]   I. M. Sobol. *A Primer for the Monte Carlo Method*. CRC Press,
             London, 1994.

[SS00]   C. Simó and T. J. Stuchi. Central stable/unstable manifolds and
             the destruction of KAM tori in the planar Hill problem. *Physica
             D*, 140:1–32, 2000.

[SW84]   V. Szebehely and A.L. Whipple. Generalizations of the Jacobi
             integral. *Celestial Mechanics*, 34:125–133, 1984.

[TGML05]   K. Tsiganis, R. Gomes, A. Morbidelli, and H. F. Levison. Origin
             of the orbital architecture of the giant planets of the Solar System.
             Nature, 435:459–461, 2005.

[TS14]   C. Trujillo and S. Sheppard. A Sedna-like body with a perihelion
             of 80 astronomical units. *Nature*, 507:471–474, 2014.

[VM11]   K. Volk and R. Malhotra. Inclination mixing in the classical
             Kuiper Belt. *The Astronomical Journal*, 142:131–154, 2011.

[Wal72]   J. Waldvogel. A new regularization technique of the planar prob-
             lem of three bodies. *Celestial Mechanics*, 6:221–231, 1972.

[Wal13]   S. Wallis. Binomial Coonfidence Intervals and Contingency
             Tests: Mathematical Fundamentals and the Evaluation of Alter-
             native Methods. *Journal of Quantitative Linguistics*, 20(3):178–
             208, 2013.

[WFOM95]   I. P. Williams, A. Fitzsimmons, D. O'Ceallaigh, and B. G. Mars-
             den. The slow-moving objects 1993 SB and 1993 SC. *Icarus*,
             116:180–185, 1995.

[Whi84]   A. L. Whipple. Equilibrium solutions of the restricted problem
             of $2 + 2$ bodies. *Celestial Mechanics*, 33:271–294, 1984.

[WS84]   A. L. Whipple and V. Szebehely. The restricted problem of $n + \nu$
             bodies. *Celestial Mechanics*, 32:137–144, 1984.

[WW85]   A. L. Whipple and L. K. White. Stability of binary asteroids. *Celestial Mechanics*, 35:95–104, 1985.